Pulsed Field Gradient Magnetic Resonance
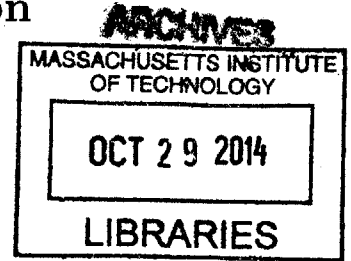# Measurements of Lithium-Ion Diffusion

by

Kevin D. Krsulich

B.S., Physics (2007)

Massachusetts Institute of Technology

Submitted to the Department of Nuclear Science and Engineering
in partial fulfillment of the requirements for the degree of

Doctor of Philosophy in Nuclear Science and Engineering

at the

MASSACHUSETTS INSTITUTE OF TECHNOLOGY

September 2014

Author .... **Signature redacted**

Kevin D. Krsulich

Department of Nuclear Science and Engineering

August 18, 2014

Certified by .... **Signature redacted**

David G. Cory

Professor of Chemistry, University of Waterloo

Thesis Supervisor

Certified by .... Signature redacted

Paola Cappellaro

Associate Professor of Nuclear Science and Engineering

Thesis Reader

Accepted by .... **Signature redacted**

Mujid S. Kazimi

TEPCO Professor of Nuclear Engineering

Chair, Department Committee on Graduate Students

Pulsed Field Gradient Magnetic Resonance Measurements of Lithium-Ion Diffusion

by

Kevin D. Krsulich

Abstract

The transport of lithium ions between the electrolyte-electrode interface and the electrode bulk is an essential and presently rate limiting process in the high-current operation of lithium-ion batteries. Despite their importance, few methods exist to experimentally investigate these macroscopic diffusion processes and, as a result, much remains unknown regarding their underlying mechanisms and the resulting macroscopic transport. Gradient nuclear magnetic resonance measurements are a mature and effective means of investigating macroscopic transport phenomena and posses several advantages over competing measures of transport in ionic solids. However, short coherence times, slow diffusion rates and a small gyromagnetic ratio have, to date, limited their usefulness for measurements of room-temperature transport in solid lithium-ion conductors.

Recent developments in quantum control have demonstrated methods for extending the coherence times of dipolar-coupled nuclear spins by several orders of magnitude, into a regime enabling gradient measurements of slow lithium-ion diffusion. This thesis proposes and demonstrates, through the utilization of a dipolar refocusing sequence and a strong pulsed magnetic field gradient, a nuclear magnetic resonance method for the direct measurement of the lithium ion self-diffusion coefficient within room-temperature lithium-ion conductors.

Magnetic resonance field gradient measurements derive ensemble transport statistics through observation of the residual phase mismatch following two position dependent phase rotations, implemented as DC pulses of a spatially varying gradient field, separated in time by a transport period. Generating sufficiently fine spatial encodings to be sensitive to slow diffusion has proven challenging in solids where strong relaxation due to the homonuclear dipole-dipole interaction drastically shortens coherence times and thus limits the duration of applied gradient pulses. This study utilizes a magic echo based refocusing sequence to nullify the dominant decoherence mechanism allowing effective gradient pulses on the order of one millisecond. Combined with a custom-built pulsed field gradient, spatial encodings on the order of 1 μm are obtained.

For a demonstrative sample, the lithium-ion conductor lithium sulfide is chosen both for its favorable NMR properties and for its role in the recent renewal of interest in nanostructured integration cathode materials. Initial sample characterization reveals two ^7Li NMR lines distinguished by their static line widths and refocusing behavior. A modified version of the 1D EXSY selective inversion experiment is performed to characterize an exchange process between these two lines and extract their intrinsic spin-lattice relaxation rates.

Two stimulated echo diffusion measurements are performed to identify the apparent diffusion coefficients of each line in the presence of exchange. The observed diffusion coefficient of the narrow line is determined to be $2.39 \pm 0.34 \cdot 10^{-8} cm^2/s$. Diffusive attenuation is not observed for the broad line. These results are analyzed through a two bath exchange model parameterized by the results of the earlier exchange experiments. The influence of exchange on the observed diffusion coefficients is determined to be negligible as diffusion times are limited by the inverse of the exchange rates.

Thesis Supervisor: David G. Cory
Title: Professor

Acknowledgments

The course of my graduate studies has been rewarding and fulfilling beyond words. This is, without question, due to the wonderful array of people who have accompanied me along this long and winding journey. First, I wish to thank my advisor, Prof. David Cory, for the opportunity to work in the Cory group. He has been an endless source of guidance, insight, and encouragement and his enthusiasm and clarity as a teacher have led me along many fruitful and enjoyable research paths. I am grateful for his mentorship and friendship.

I would also like to thank all the members of the Cory group with whom I have had the pleasure and privilege of working over the past several years. In particular, Clarice Aiello, Mohamed Abutaleb, and Sekhar Ramanathan for helping to ease the steep learning curve in beginning research in the group; Sarah Sheldon and Troy Borneman for sharing in the adventurous move to Waterloo; Patryk Gumann for his guidance and friendship; Mohamad Niknam, Ivar Taminiau, Olaf Benningshof, Christopher Granade, Om Patange, and Fatin Haque from whom I have learned so much and for making my time in Waterloo extremely memorable.

I would also like to thank the many friends we've made along the way, especially Deborah Daly and Barbara Sacher, the Snider, Park, and Walther families for making sure our family always felt at home, no matter where our travels led us. And to my parents, for starting me off down this fascinating path.

I wish to express my boundless gratitude for my loving wife, Kate, whose endless patience, encouragement, and tolerance of far too many late nights turned early mornings sustained me in challenging times and motivated me in moments of doubt. And lastly, to my darling children, Charlie, Luka, Emily and Ryan, thank you for being a never-ending source of joy, laughter, and inspiration and for the ever-present reminders of what a wondrous place the world can be when you explore it with an open mind, open eyes, and open arms.

Contents

List of Figures

8

List of Tables

Chapter 1

Introduction

Lithium-ion batteries have had a marked influence on the recent upsurge in the sophistication and popularity of low-current, portable electronic devices. Their exceptional energy density, both by mass and by volume, and their long cycle and shelf lifetimes have made lithium-ion cells the dominant choice over competing battery chemistries for low-current applications [1]. However, recent attempts at the application of lithium-ion battery technology to high-current devices, such as plug-in electric and hybrid automobiles, and grid-scale energy storage, have not yet yielded the same success falling short of expectations in both cell lifetime and safety [2,3]. Addressing these shortcomings, in light of the recent popular demand for high energy density, inexpensive storage architectures to support a more diversified energy infrastructure, has become a problem of considerable societal importance.

Inadequate high-current performance of lithium-ion batteries has been attributed to the sluggishness of the intrinsic solid-state diffusion processes responsible for the migration of lithium ions between the electrode bulk and surface [4]. Lithium-ion batteries employ electrodes with open or disordered host lattice structures into which lithium ions intercalate upon charge or discharge. Cell operation requires continuous transport of lithium into and out of the bulk of these electrode structures so as to prevent the accumulation or depletion of surface lithium resulting in dangerous outgrowths of lithium metal or decreased cell output, respectively [5].

Establishing informative and applicable methods for studying the ionic diffusion

14

mechanisms which drive this transport has been a long standing challenge in the material sciences [6]. Limited experimental insight into macroscopic lithium-ion transport has hindered the engineering and optimization of next-generation electrode materials and prevented investigations into the dependence of lithium transport on cell characteristics such as cycle count and level of discharge [7].

While magnetic resonance methods have been used to great effect in the structural and chemical analysis of lithium-ion conductors [8] and in the transport analysis of lithium liquids and high-temperature solids [9–11], NMR transport studies of room-temperature lithium-ion conductors have, to date, been limited by slow diffusion rates and short coherence times. This thesis aims to explore the extent to which coherent control sequences and novel gradient design make possible field gradient nuclear magnetic resonance measurements of lithium-ion transport in room-temperature lithium-ion conductors.

This thesis proposes and demonstrates a magnetic resonance method for direct measurement of the diffusion coefficient of lithium ions within room-temperature lithium-ion conductors. To overcome the limits of an intrinsically short coherence time, a dipolar averaging sequence is utilized to refocus the dominant relaxation interactions allowing effective gradient pulses on the order of a millisecond. Extended gradient pulse lengths, in conjunction with the development of an experimental setup for the application of strong gradient pulses, allow for the application of a standard NMR experiment for the measurement of diffusion in a previously inaccessible regime.

The lithium-ion conductor lithium sulfide is chosen as an initial sample both for its favorable NMR properties and for its role in the recent renewal of interest in nanostructured lithium integration electrodes. Sulfur has been proposed as a next-generation lithium battery cathode offering higher theoretical energy densities and improved high-current performance as compared to current lithium intercalation compounds [3]. Further, the lithium polysulfides do not exhibit paramagnetism or electronic conduction throughout the entire range of lithium concentrations and as such, are expected to respond favorably to known NMR coherent control schemes.

The following chapter reviews the current state of the field in the application of

NMR methods to measurements of transport in various lithium-ion conductors as well as reviewing the advances and limitations of a selection of non-NMR methods. Chapter 3 describes a series of experiments performed to characterize the solid-state NMR properties of lithium sulfide. These experiments reveal two distinct ^7Li lines distinguished by their static line widths and relative amplitudes. Subsequent relaxation measurements suggest the existence of an exchange process between these lines.

To characterize this exchange process and obtain the intrinsic relaxation rates associated with each line, a modified 1D exchange spectroscopy experiment was performed as reported in Chapter 4. By comparing the dependence of the rate and form of each bath's magnetization recovery on the system initial magnetization state to a two bath dissipative exchange model, the exchange rates and intrinsic spin-lattice relaxation rates are obtained.

Chapter 5 describes two stimulated echo diffusion measurements subsequently performed to investigate potential diffusion processes. These experiments employ a custom-built gradient coil to create magnetization gratings with pitches down to 1 μm during effective gradient pulses on the order of one millisecond in length. Observation of the attenuation of the stimulated gradient echo amplitude as a function of both diffusion time and grating pitch allows measurement of the rates of ensemble diffusion processes. For the broader of the two lines, a magic echo based refocusing sequence is utilized to extend the naturally short coherence time and allow for longer effective gradient pulses, resulting in finer spatial resolution and sensitivity to slower diffusion. These results are analyzed in light of the exchange model described earlier to extract, from the observed echo attenuations, the intrinsic diffusion coefficient of each bath.

To motivate the following discussion of lithium diffusion and to understand the importance of transport in influencing lithium battery performance, we begin with a description of the chemistry and kinetics underlying the operation of lithium batteries.

Lithium Battery Chemistry

Lithium electrochemical cells utilize the difference in chemical potential between a lithium enriched anode and a lithium deficient cathode to drive an electrical load. An

electrolyte separates the two electrodes and acts as an effective Li^+ ion permeable, Li atom impermeable filter thereby limiting cell self-discharge and supporting the necessary charge compensating ionic current.

To match the rapid rate at which lithium ions may traverse the electrolyte, a solid-state transport process is required within each electrode to either replenish surface lithium ions or to vacate surface sites for subsequent ion arrivals. Migration rates which fail to keep pace with the rate at which ions pass through the electrolyte will result in transport-induced structural damage such as the accumulation of lithium metal structures on the electrode surface leading to decreased cell stability, lifetime and safety [6, 12, 13]. The transport of lithium ions between electrode surface and bulk sites is driven only by a concentration gradient resulting in a rate of ion flow considerably slower than the rate at which ions may cross the electrolyte [7]. The rate of these solid-state diffusion processes presently sets the limit on safe operating current and thus maximum power output of lithium-ion batteries.

To address these issues, considerable effort has been invested in the identification and characterization of next-generation cathode materials which aim to be low cost, environmentally benign, and boast improved energy storage densities and high-current performance over current implementations [1, 14]. To be effective, this search requires both thorough theoretical understanding and experimental insight into the materials properties which directly influence the performance of lithium electrode materials.

Transport Dynamics in Lithium Battery Cathode Materials

While cell properties such as operating voltage and energy density are determined solely by cell chemistry, others are dependent on kinetic processes which often display a complicated and concentration-dependent dependence on cathode host structure. Furthermore, many cathode materials display dramatic structural and crystallographic responses to changes in lithium concentration which in turn result in lithium-ion mobilities which may vary by several orders of magnitude within a single discharge cycle [15].

Despite the need to investigate the factors influencing lithium-ion mobility, experimental probes of lithium transport dynamics have been, to date, limited in their usefulness. Indirect indications of transport are accessible through the range of electrochemical methods widely employed for measurements of the thermodynamic properties of lithium-ion batteries such as the chemical potential, Gibbs free energy and entropy. However, these methods are not well suited for measurements of transport. Kinetic measures obtained through electrochemical methods are, in general, poorly isolated from the thermodynamic interactions under study and extraneous environmental factors such as cell geometry. As a result, obtaining reliable measures of lithium transport through electrochemical methods has proven challenging [16,17].

Nuclear magnetic resonance spectroscopy and relaxometry have proven useful in providing direct insight into the atomic scale structure and transport dynamics of lithium-ion conductors such as exchange rates, jump mechanisms and activation energies [18]. However, the extension of these microscopic measures into the macroscopic transport properties of interest requires accurate models of both the material structure and the nature of the active relaxation and transport mechanisms and does not encapsulate macroscopic transport phenomena such as ordering and vacancy clustering [8].

Magnetic field gradient NMR experiments, by contrast, are sensitive to collective transport phenomena through the systematic observation of an ensemble average residual phase mismatch following two position-dependent phase rotations separated in time by a transport period. The dependence of this phase mismatch as a function of both transport time and gradient pulse length provides direct experimental access to the macroscopic diffusion profile and in the case of Gaussian diffusion, a measure of the free diffusion coefficient [19]. Field gradient NMR methods have been successfully employed in transport studies of liquids and high temperature hydrogen, fluorine and lithium ion conductors [20–22]. However, generating sufficiently rapid spatially dependent evolution necessary to be sensitive to the short diffusive path lengths in room-temperature solids requires gradient pulses of exceptional length and intensity. The small gyromagnetic ratio of lithium and short coherence times common in the

NMR of solids further extend gradient pulse requirements and have considerably limited application of field gradient measurements of lithium transport in solids [23].

1.1 Ionic Transport Processes in Lithium-Ion Batteries

Contrary to the common pedagogical view of solids as rigid, tightly packed, thermally vibrating lattices, many solids are dynamic systems with open or loosely packed lattice structures, constant thermal motion and varying degrees of disorder. The open structure and disorder present in such systems permit the long range motion of interstitial and host atoms from which emerges thermal transport and diffusion processes. Lattice disorder and loose binding allow individual ions to migrate about their host lattice, albeit at a relatively slow rate, and are critical phenomena in the abilities of materials such as solid electrolytes, ionic membranes, and insertion electrodes where fast ionic diffusion rates support the flow of an electrical current and in materials such as ionic glasses where slow rates of ionic diffusion allow the preservation of a technologically useful non-equilibrium state [24, 25].

In lithium-ion batteries, ionic diffusion determines the upper limits of cell charge and discharge rates. Unlike other cell chemistries whose operation involves continuous surface plating of either electrode, lithium-ion battery electrodes continuously integrate lithium ions into their active mass. A Li^+ ion deposited on the electrode surface migrates into the electrode bulk so as to release a surface site for subsequent ion arrivals and thus prevent accumulation of lithium metal deposits on the electrode surface. In the absence of sufficiently rapid ionic diffusion processes, mossy or dendritic lithium microstructures develop a solid-electrolyte interface on the electrode surface resulting in an impedance barrier to further current flow and, in cases where dendrites reach fully across the electrolyte, an internal short circuit and safety hazard [7, 12, 13].

To address these shortcomings, a broader variety of materials has been considered

for development as the next generation of lithium battery cathode. These include additional intercalation compounds both of newly developed chemistries as well as existing compounds doped with additives to improve ionic and electric conductivity [14]. Recently, integration chemistries such as $Li - S$ and $Li-$Air cells, wherein lithium ions do not occupy interstitial sites but rather form covalent chemical bonds with the host lattice, have drawn increased interest due to their greater theoretical energy storage densities, up to an order of magnitude greater than those of intercalation electrodes [3, 26, 27]. Integration materials too are current-limited by the solid-state ionic diffusion processes required for full, uniform reduction or oxidation of the electrode bulk. In lithium-sulfur cells, for example, half of the available energy density is released through insoluble sulfides inaccessible without the presence of a solid-state transport process [28].

1.2   Fick's Laws and Gaussian Diffusion

Transport processes in lithium batteries involve lithium ions hopping between local energetic minima within a host electrode structure driven by a modest concentration gradient. The measure of interest then, in quantifying the rate of lithium-ion transport, is the diffusion coefficient as defined by Fick's first law. Fick's first law defines a diffusion coefficient D relating the particle flux $\vec{J}$ induced by a concentration gradient to the gradient of the concentration profile, as

$$\vec{J}(\vec{r}, t) = -D\nabla c(\vec{r}, t). \tag{1.1}$$

Combining Equation 1.1 with a continuity of mass requirement,

$$\frac{\partial c(\vec{r}, t)}{\partial t} + \nabla \vec{J}(\vec{r}, t) = 0, \tag{1.2}$$

yields Fick's second law, Equation 1.3, which can be solved under assumption of a constant diffusion coefficient to find the resulting time and space evolution of the diffusing species' concentration profile or, conversely, to determine the diffusion coef-

ficient from measurements of the concentration profile [29].

$$\frac{\partial c(\vec{r}, t)}{\partial t} = D\nabla^2 c(\vec{r}, t) \tag{1.3}$$

A corresponding microscopic picture of diffusion is obtained by substituting a conditional jump probability $\wp(\vec{r}|\vec{r_0}, t)$ for the concentration profile $c(\vec{r}, t)$ and asserting that it too will satisfy Equation 1.3. An analogous microscopic definition of the diffusion coefficient is obtained through the Einstein-Smoluchowski relation

$$D = \lim_{t \to \infty} \frac{\langle r^2(t) \rangle}{2dt} \tag{1.4}$$

where $\langle r^2(t) \rangle$ is the mean square particle displacement after a time t and d is the dimensionality of the diffusion process [30, 31].

For the case of unbounded diffusion in one dimension, Equation 1.3 may be solved to derive a displacement probability density function by imposing the initial condition $\wp(r|r_0, 0) = \delta(r_0 - r)$. The solution is a Gaussian diffusion process

$$\wp(r|r_0, t) = \frac{1}{(4\pi Dt)^{1/2}} e^{-(r-r_0)^2/4Dt} \tag{1.5}$$

from which the average square displacement can be found to match the condition of Equation 1.4,

$$\langle (r(t) - r_0)^2 \rangle = 2Dt. \tag{1.6}$$

1.3 Measures of Ionic Transport

The description of diffusion as presented in the previous section makes several assumptions, not necessarily held in real solids, which ensure agreement between the microscopic and macroscopic descriptions of a diffusion process. The previous section's description of Fickian diffusion assumes the absence of correlations between sequential jumps in the diffusion process and the absence of interactions between members of the diffusing species. These assumptions need not be true and, when

violated, result in a divergence of the dynamics predicted by the microscopic and macroscopic descriptions of diffusion. To characterize diffusion in materials then, experimental probes of both microscopic and macroscopic diffusion are needed.

Macroscopic probes of transport report on the long range diffusion processes responsible for determining diffusion-dependent materials properties and device characteristics. They are sensitive to emergent phenomena such as correlated diffusion, ordering and vacancy clustering. Microscopic probes, on the other hand, are sensitive to the local, atomic scale influences of diffusion and inform measurements of the activation energy, average jump length, and residency time of a given diffusion process.

The diffusion coefficient, as defined in Fick's first law, is more specifically referred to as the chemical diffusion coefficient, D_C, and describes a diffusing system's macroscopic response in the presence of a concentration gradient. In order to relate the dynamics predicted by microscopic and macroscopic models of diffusion, it is possible to extrapolate, from microscopic quantities, an equivalent diffusion coefficient, called the jump diffusion coefficient, under the assumption of uncorrelated jumps through the Kubo-Green expression

$$D_J = \lim_{t \to \infty} \frac{1}{2dt} \left\langle \frac{1}{N} \left(\sum_{i=1}^{N} \Delta \vec{R}_i(t) \right)^2 \right\rangle = \frac{\ell^2}{2d\tau} \tag{1.7}$$

where $\Delta \vec{R}_i(t)$ is the vector connecting the trajectory of particle i after a time t, ℓ is the average jump length, τ is the mean residency time and angled brackets denote an ensemble average [32]. It is also useful to define a tracer, or self, diffusion coefficient, D_T, to describe the dynamics of a diffusing species in the absence of a concentration gradient [33],

$$D_T = \lim_{t \to \infty} \frac{1}{2dt} \left(\frac{1}{N} \sum_{i=1}^{N} \left\langle \left(\Delta \vec{R}_i(t) \right)^2 \right\rangle \right). \tag{1.8}$$

The tracer diffusion coefficient measures the mean square displacement of individual members of the diffusing species rather than the mean square displacement of the center of mass of all diffusing particles as measured by the jump diffusion coefficient.

In the ideal case, a single diffusion coefficient is sufficient to encapsulate the dynamics of a diffusion process across these three descriptions. The disagreement between the measured diffusion coefficients identifies the role of specific non-idealities in the resulting macroscopic behavior.

The ratio between the microscopic derived jump diffusion coefficient and the macroscopic tracer diffusion coefficient defines a correlation factor f,

$$D_T = fD_J, \tag{1.9}$$

which is unity for random, uncorrelated hopping of the diffusing species and $0 < f < 1$ for correlated motion defined by an increased likelihood of backward hopping following any given jump. A similar relation is defined between the jump and chemical diffusion coefficients,

$$D_C = \Theta D_J, \tag{1.10}$$

where Θ is the thermodynamic factor related to the gradient of the chemical potential μ as $\Theta = \frac{\partial(\mu/kT)}{\partial \ln x}$ and deviates from unity to compensate for the fact that the driving force underlying diffusion processes is a gradient in chemical potential, rather than a gradient in concentration as assumed in Fick's first law [34]. This thermodynamic factor varies substantially from unity at non-dilute concentrations for lithium intercalation compounds and diverges at lithium concentrations where lithium-vacancy ordering is stable [15,35].

Determination of the correlation and thermodynamic factors through observation of microscopic and macroscopic transport allows one to establish the active diffusion mechanism by comparing the measured values to those calculated for modes of diffusion available for the given lattice structure [36]. For instance, a direct interstitial mechanism predicts $f = 1$ whereas a vacancy mechanism in a bcc lattice is characterized by $f = 0.727$ [37,38].

1.4 Nuclear Magnetic Resonance

Spatial NMR methods measure transport through the use of the nuclear spin degree of freedom as a flag of the relative motion of individual spins in the presence of a spatially non-uniform Hamiltonian. Spatial selectivity is achieved through a position dependent phase rotation, resulting in a magnetization helix with a pitch determined by the product of the rotation rate and duration. A more tightly wound helix allows for greater spatial resolution in imaging applications and sensitivity to smaller displacements for transport measurements.

This position dependent rotation is often achieved through the use of a spatially non-homogeneous magnetic field aligned with the static Zeeman field. Ease of implementation and the ability to modulate the gradient strength have made DC gradient coils a common choice. The use of gradient fields produced in the stray fields of superconducting magnets [39] or through specifically designed superconducting gradient coils [40] have also been explored. Other approaches, such as utilizing the field gradient in the immediate vicinity of a magnetic particle [41,42] or near the surface of a type-II superconductor [43,44], have demonstrated exceptional gradient strengths but suffer drawbacks in that accessible volumes are small and the gradient profile is highly non-uniform making the inclusion of sufficiently many spins to generate an observable NMR signal challenging. Other schemes, such as the use of inhomogeneous RF pulses have also been explored but suffer from weak gradient strengths and have failed to find widespread adoption [45].

Static field gradients are an effective and frequently utilized means of generating large field gradients for NMR studies. NMR measurements of diffusion utilizing the static field gradient produced in the fringe field of a superconducting solenoid or through the construction of a special geometry of superconducting coils, have demonstrated gradient strengths up to 60 T/m and 200 T/m, respectively [40]. While superconducting static field gradients have advantages of high strength, stability and ease of access and implementation, the inability to completely remove or modulate the gradient interaction limits the ability to obtain high resolution spectra and utilize

coherent averaging sequences to extend coherence times [46].

Alternately, pulsed field gradient experiments utilize a set of resistive coils to impose a field gradient which may be removed, modulated, or inverted. Switching times on the order of several microseconds are common [47] and so high resolution spectra are obtainable and a variety of coherence extending sequences are applicable [48]. Pulse field gradients are, however, generally considerably weaker than their static counterparts. To obtain the large gradient fields required for solid-state studies of diffusion, exceptional currents of hundreds of amperes are required which, in turn, raise experimental challenges in the form of gradient matching, Joule heating and Lorentz forces [49].

The fine resolution essential for spatial NMR studies in solids such as imaging and slow diffusion measurements require the creation of a tightly wound magnetization helix to encode and detect small displacements and accurate relative positions. The short coherence times common in solids generally limit the duration of applied gradient pulses but multiple short, rapidly switched pulses may be composed if compatible with multipulse coherent control sequences to create the required encoding before the initial polarization is lost to relaxation.

Chapter 2

Transport Measurements of Lithium-Ion Conductors

Materials selection and engineering are central to many of the recent advances in lithium-battery technology. Electrode materials, specifically, determine cell energy density, voltage, and operating current and influence properties such as cell cycleability, lifetime, and safety. Consequently, substantial effort has been invested in the discovery and characterization of candidate electrode materials. This chapter aims to review the experimental methods employed to quantify the properties of lithium-battery materials and to summarize results for a selection of relevant materials.

Lithium-battery material characterization is usefully divided into measures of thermodynamic and kinetic properties. Thermodynamic properties, including the chemical potential, Gibbs free energy and entropy, determine battery characteristics such as the electrochemically active voltage range and the energy storage density. Kinetic processes, such as diffusion, cathode structural phase transitions, and interface reactions, determine the shape of the voltage curve and the limits of operating current. While mature methods exist to study thermodynamic properties of lithium electrode materials, measures of kinetic processes have proven more difficult to isolate experimentally and applicable experimental methods are currently lacking.

2.1 Experimental Probes of Lithium-Ion Transport

The canonical method for measurement of the self-diffusion coefficient is the tracer radioisotope experiment. Through observation of the time and spatial dependence of the radiative emission from a geometry of initially partitioned isotopes of a given material, a direct measure of the rate of self diffusion is obtained [29]. The tracer diffusion experiment is preferred when possible as the obtained data is easily interpreted and provides unambiguous insight into the self-diffusion coefficient of the mobile species neglecting the influence of any isotope effect on the rate of diffusion. However, the method requires a radioisotope with a sufficiently long half-life to allow for macroscopic diffusive path lengths and so is not applicable for measurements of slow lithium transport as lithium lacks a suitably long-lived radioisotope.

A number of alternate methods have been employed for the experimental investigation of lithium transport in these materials. A selection of these methods are reviewed below and the results obtained are summarized for several important lithium-ion conductors.

2.1.1 Electrochemical Methods

Electrochemical methods are frequently utilized to study the thermodynamic properties of lithium electrochemical cells. By recording the steady state voltage or charge response of a system to incremental changes in applied charge or voltage, accurate measures of the thermodynamics underlying an electrochemical reaction are obtained.

The transient system response following these incremental changes in applied voltage or charge, informed by a model of transport with the electrode, yields insight into the macroscopic transport properties of the mobile species within the cell. Electrochemical methods for studies of transport are commonly applied due to their ease of implementation. However, obtaining reliable measures of macroscopic transport from these methods has proven challenging. Indications of transport are poorly isolated from extraneous factors such as cell geometry, mass transfer, surface films and side reactions.

The potentiostatic intermittent titatration technique (PITT) applies small, incremental voltage steps interspersed with open circuit periods during which the system is allowed to relax to a potential equilibrium [50]. Integration of the current-time curve yields the charge increment, the accumulated charge in response to a given applied voltage, from which cell thermodynamic properties may be calculated and the curve shape following changes in the applied voltage is determined by the rates of transport. PITT allows for identification of electrode phase transitions and models have been established to determine the chemical diffusion coefficient from PITT data in both single and two phase regions, and can be used to distinguish between diffusion and nucleation mediated transport [51].

A complimentary method is the galvanostatic intermittent titration technique (GITT) which applies a set current to an electrochemical cell for a fixed period of time resulting in successively increasing levels of charge. Between each current application, a relaxation time allows the cell to reach equilibrium, demonstrated by stability in the measured open circuit voltage. The observed voltage response allows determination of the cell voltage profile and kinetic properties such as the chemical diffusion coefficient and ionic conductivity [52]. Similarly, the location of plateaus in the observed voltage response inform measurements of thermodynamic properties and the curve shape surrounding current switches inform measures of kinetic properties.

While the system responses observed in these methods are influenced by transport such that the properties of the transport process may be inferred from the observed voltage profile through the use of an appropriate model, these methods of probing lithium transport phenomena have proven unreliable in generating consistent measures of the chemical diffusion coefficient [7, 16]. Measures of kinetic properties are poorly isolated from competing kinetic phenomena, such as the rate of parasitic background currents, which are themselves heavily influence by experimental parameters such as electrode geometry and current duration. The influence of such extraneous kinetic processes are not easily compensated for or isolated and greatly complicate data analysis. Furthermore, the ability to extract the chemical diffusion coefficient from the observed current or voltage profile relies on several assumptions

often not valid in lithium-ion conductors such as a lack of ion/electron interactions and anisotropic diffusion, resulting in measures of the diffusion coefficient which may vary by as many as ten orders of magnitude for a single material at a given lithium concentration [6, 17, 53].

Electrochemical impedance spectroscopy (EIS) provides direct electrochemical access to the macroscopic diffusion properties of a sample [54]. Systematic measurements of the frequency dependent AC impedance of a material are extrapolated to obtain the low frequency conductivity limit. The Nernst-Einstein equation relates the measured DC conductivity σ_{DC} and the diffusion coefficient,

$$D^\sigma = \frac{\sigma_{DC} k_B T}{N q^2} \qquad (2.1)$$

where N is particle density of charge carriers and q is their charge.

EIS is of its greatest utility when only a single charge carrier contributes to the observed conductivity. The Haven ratio,

$$D^T = H_R D^\sigma, \qquad (2.2)$$

quantifies whether the observed conductivity is due to a single charge carrier or several [55]. For single ions diffusing via random jumps, $H_R = f = 1$ and $D^T = D^J = D^\sigma$. A Haven ratio less than unity is observed in the presence of correlations in the movement of charge carriers or electronic conduction. A Haven ratio greater than unity is observed when vacancy pairs or impurity-vacancy pairs jointly participate in diffusion but do not contribute to the observed macroscopic conductivity. EIS measurements alone are not sufficient to determine the Haven ratio and so are not independently able to unambiguously measure the diffusion coefficient of a mobile species.

2.1.2 Neutron Scattering

Neutrons are frequently used in structural and crystallographic studies of lithium-ion conductors and have also found application in the investigation of kinetic and transport processes. High temperature powder neutron diffraction has recently been applied to identify diffusion pathways in lithium-ion conductors by studying the observed lithium distribution within the unit cell [56]. Quasielastic neutron scattering (QENS), through observation of the energy and angular dependence of the scattering function and comparison against theoretical models, provides a more direct measure of transport and obtains a microscopic measure of the jump diffusion coefficient [57]. However, a lack of sensitivity to the length scales of slow diffusion has so far restricted the application of QENS to measurements of transport in high-temperature lithium-ion conductors [58].

Lithium's large neutron cross section and, in particular, the four order of magnitude difference between that of lithium's two stable isotopes, ^6Li and ^7Li, have allowed application of cold neutron radiography experiments to the study of room-temperature lithium transport. In-situ studies of the spatial evolution of lithium concentration during cell charge and discharge report indirectly on the influence of transport processes on cell aging and safety [59,60]. A cold neutron radiography experiment has been proposed and realized for the study of macroscopic lithium mass transport similar to the tracer diffusion experiment. By coating a natural abundance lithium-ion conductor with its ^7Li enriched counterpart and observing the time evolution of spatially resolved neutron transmission rates, a macroscopic measure of the self diffusion coefficient is obtained [61]. However, limits on the resolution of spatially sensitive neutron detectors require extended periods of high-temperature diffusive annealing to achieve sufficiently long diffusive path lengths to be able to resolve the influence of diffusion.

2.1.3 Ab-Initio Statistical Mechanics

First principles statistical mechanics calculations provide insight into both the thermodynamics and kinetics of transport in lithium-ion conductors. By incorporating calculations of the activation barriers and pathways of various jump mechanisms and ab-initio calculations of electronic structure into kinetic Monte Carlo simulations, a number of thermodynamic and kinetic properties can be measured at thermodynamic equilibrium for a range of lithium-ion conductors [62]. Moreover, these methods allow for the prediction of the shapes of finite temperature phase and voltage curves, and their dependence on host parameters such as temperature and lithium concentration [63]. Ab-initio methods benefit from their ability to calculate a large number of material properties for a broad class of materials under a large variety of material parameters and conditions at a rate far greater than is achievable through experimental methods.

2.1.4 Muon Spin Rotation Spectroscopy

Muon spin rotation (μSR) spectroscopy is a relatively recent addition to the set of tools used to investigate the kinetics of lithium transport. μSR makes use of the fact that, upon the decay of a muon, the direction of the emitted positron is preferentially aligned with the parent muon's magnetic moment. Thus, the rate of precession of the angular moment of a spin polarized muon due to the magnetic environment of a given material and the resulting asymmetry in the angular distribution of positron emission are indicators of both the local field strength and field fluctuations as observed from the muon site within the material.

The expected response for positron arrival counts as a function of time at any given solid angle following the insertion of a low energy, spin polarized muon is a sinusoidal oscillation overlaid on a decaying exponential. The rate of oscillation is determined by the local field strength. The decay of the angular asymmetry, in cases where relaxation is driven by spin interactions with nearby lithium nuclei, is determined by and may be used to measure the rate of ionic hopping on a timescale set by the lifetime

31

of the muon in a way analogous to motional narrowing and coherence preservation in NMR relaxometry [64–66].

In lithium cobalt oxide, for example, injected positive muons are likely to bind near the O^{2-} and so will experience a local field fluctuation due to the presence or absence of diffusing lithium ions in the neighboring interstitial sites of the CoO_2 host lattice. The fluctuations of this field determine the rate of asymmetry decay such that slow lithium motion yields a Gaussian profile and fast ionic motion yields an exponential decay. This measure of the muon local field fluctuations can be combined with knowledge of the lithium-ion conductor structure, jump pathways and distances to obtain a measure of the jump diffusion coefficient [67,68]. This method has been broadly applied recently to a number of lithium-ion conductors and has yielded good agreement with ab-initio calculations of the microscopic diffusion coefficient.

2.1.5 Nuclear Magnetic Resonance

Nuclear magnetic resonance is a powerful probe of the local magnetic interactions experienced by a collection of nuclear spins within a macroscopic sample. NMR methods manipulate and observe the macroscopic magnetic moment due to the polarization of a nuclear spin ensemble in the presence of a strong external magnetic field. The Larmor precession of the magnetic moment and resulting observed signal can be tailored, via judicious engineering and design of radio frequency control fields, to shed light on the kinetics of lithium transport.

Lithium has two stable active NMR nuclei. Spin 1 lithium-6 is 7.42% natural abundance and has a gyromagnetic ratio of $3.94 \cdot 10^7$ rad/Ts. Spin 3/2 lithium-7 is 92.58% natural abundance and has a gyromagnetic ratio of $10.39 \cdot 10^7$ rad/Ts. High resolution NMR studies favor lithium-6 for its high sensitivity and low quadrupole moment, while spatial NMR studies preferentially utilize lithium-7 for its larger gyromagnetic ratio.

In general, the static spectra of solids will be broadened due to the strength of unrefocused nuclear couplings. For applications requiring extended coherence times, such as high resolution spectroscopy or phase encoded transport measurements, a

means of extending coherence is required. Magic angle spinning is one such NMR technique frequently employed to remove the influence of the dominant dipolar decoherence mechanism allowing extended coherence times and high resolution spectra to be obtained. These spectra inform structural models, determine bond lengths and electronic structure, and identify likely pathways for diffusion [8,69].

NMR relaxometery methods are employed to study the nature of the fluctuating fields observed by the nuclear spin and, when combined with models of the influence of active transport processes on relaxation, are able to provide measures of microscopic kinetic quantities such as the hopping frequency and jump activation energy [70–73].

Magnetic resonance imaging and skin-depth sensitive spectroscopy have demonstrated the effects of transport induced structural damage and aging, the existence of mossy and dendritic lithium outgrowths from electrodes and have proven useful in non-destructively examining failed battery cells [12,13].

Relaxometry

When NMR relaxation rates are dominated by fluctuating fields modulated by ionic motion, measurement of these rates as a function of temperature and Larmor frequency provides a measure of the microscopic kinetics underlying the ionic transport mechanism. For example, a nucleus undergoing a jump process with a jump rate following an Arrhenius relation, $\tau^{-1} = \tau_0^{-1} e^{-\frac{E_A}{k_B T}}$ with activation energy E_A, one observes a characteristic narrowing of the observed line width when the jump rate is greater than the width of the rigid lattice line,

$$\tau^{-1} \gtrsim 2\pi \Delta \nu_R. \tag{2.3}$$

This preservation of coherence occurs when the interactions between neighboring nuclei which lead to decoherence in the static case are quenched by motion. Measuring the onset of motional narrowing as a function of temperature allows one, through Equation 2.3, to measure the activation energy of the jump process and the jump rate.

Nuclear motion may similarly modulate interactions generating spin-lattice relaxation and this dependence is also utilized to quantify rates of hopping in lithium ionic conductors. The spin-lattice relaxation rate, T_1, is derived from a linear combination of spectral density functions of the fluctuations in the dipolar fields and electric field gradients around the nuclei. For the case of isotropic, uncorrelated hopping, an exponentially decaying correlation function results in a Lorentzian spectral density [74]. Measuring the temperature dependence of the spin-lattice relaxation rate at a given Larmor frequency produces a maximum when the jump frequency approximately equals the Larmor frequency, $\omega_L \tau(T) \approx 1$, the location of which allows for the determination of the mean residency time and activation energy. Spectral densities have been calculated for common modes of lattice diffusion [75–78].

Field Gradient NMR

The previously described NMR methods observe the collective evolution of a nuclear spin ensemble across a macroscopic sample taking care to reduce external variability in the nuclear spin Hamiltonian across the ensemble so as to maximize sensitivity to shared, local interactions. Through the introduction of engineered spatially varying control fields, sensitivity to macroscopic transport may be introduced to NMR methods while, in certain cases, maintaining sensitivity to local fields so as to obtain chemically resolved measures of transport.

Generally, field gradient experiments probe macroscopic transport by analyzing changes in spin evolution as nuclei migrate through the gradient field. Long coherence times and a strong spatial dependence in the system Hamiltonian are thus required to allow for the generation of measurably different evolutions across short diffusive path lengths. Likewise, slow longitudinal relaxation rates permit long diffusion times which, in turn, allow for the accumulation of a significant diffusive displacement and thus sensitivity to slower diffusion rates.

Material Suitability for NMR Studies of Transport

The sensitivity of NMR to small variations in local magnetic fields implies that the applicability of NMR methods will in general be contingent upon the presence or absence of particular magnetic and electronic materials properties. In particular, for lithium-ion conductors where paramagnetism and electronic conduction are common due to the usage of these materials in an electrochemical process, electronic materials properties will strongly influence NMR spectra and so affect the applicability and sensitivity of NMR studies of lithium transport kinetics.

Paramagnetism is commonly found in lithium intercalation compounds as a means of maintaining charge neutrality as lithium concentration varies. In paramagnetic materials, depending on the configuration of electrons surrounding the paramagnetic ion, a through space magnetic coupling between the paramagnetic center and nuclear spins will exist and will often dominate the magnetic evolution of the nuclear spin. The additional decoherence pathway of the nuclear spin introduced by its coupling to the rapidly relaxing paramagnetic moment can be exceptionally fast, limiting the use of experiments requiring extended coherence times [79].

Similarly, electrical conductivity is a desirable property of lithium electrodes as a means of providing contact between the chemical energy store and electrical load. However, the modulation of both control and response fields introduced through the skin depth effect of conductive materials complicates NMR studies. While this effect makes possible applications such as skin depth sensitive imaging, the inability to uniformly excite and detect ensemble spins and absorption of RF power limit applicability of coherent control sequences.

2.2 Review of Transport in Selected Lithium-Ion Conductors

Lithium cobalt oxide and lithiated graphite have comprised the preferred chemistry of the lithium-ion battery as cathode and anode, respectively, since its commercial

introduction [80]. However, the high cost and toxicity of cobalt and poor high-current performance of graphite have spurred a search for cheaper, more environmentally benign electrode materials with faster charge and discharge rates and improved cell lifetimes to meet the increased demand for energy storage support for high power, high energy density applications.

To this end, a wide variety of materials has been investigated in search of candidate lithium battery electrodes and considerable literature exists investigating the kinetic properties of this breadth of lithium-ion conductors. This section summarizes results for a selection of relevant materials. Transport properties and material parameters are collected in Table 2.1 and the preceding sections briefly describe the nature and kinetics of several classes of lithium-ion conductor.

2.2.1 Graphitic Carbon

Graphitic carbon has emerged as the dominant anode material of commercial lithium-ion batteries. The layered structure of these carbonaceous materials provides ample space for lithium intercalation and transport with minimal distortion and strain in the host lattice. Importantly, encapsulating lithium within the electrodes at both sides of the cell avoids the dangers associated with utilizing lithium metal anodes directly. As an anode, graphite is low cost, has a low operating potential, high capacity, high reversibility and exceptional interface stability [81]. However, relatively poor charge and discharge rate performance contribute to transport induced surface structural damage upon prolonged cycling which, in turn, limits cell lifetime and restricts the usage of lithiated graphite anodes for high-current applications.

In graphite, lithium occupies interstitial sites between graphene planes and thus transport is expected to be highly anisotropic. Consequently, reports of electrochemical measures of the diffusion coefficient, generally insensitive to anisotropic transport, vary by as many as ten orders of magnitude, from 10^{-6} to 10^{-16} cm^2/s [82–86]. Through a combination of ab-initio statistical calculations, and a geometrically arranged electrochemical study of highly oriented pyrolytic graphite, diffusion coefficients of $8.7\pm0.4\cdot10^{-12}cm^2/s$ perpendicular to graphite planes and $4.4\pm0.1\cdot10^{-6}cm^2/s$

along graphite planes have been measured [6, 87].

A variety of alternate anode materials have been considered to address the known shortcomings of graphite. Elemental anodes like silicon, tin and germanium boast high theoretical capacities but suffer severe volume expansion and contraction by as much as a factor of three upon lithiation and de-lithiation [88, 89]. After prolonged cycling, repeated strain due to volumetric expansion and diffusion induced stress leads to electrode cracking and fracture leading to loss of electrical conductivity and capacity fade [90]. Nanostructured electrodes integrating novel active anode materials such as $Sn/C/Co$ alloys and $Si - C$ composites within a carbonaceous framework have been investigated but, in addition to exceptionally increased fabrication costs, these structures suffer from an increased rate of solid electrolyte interface formation. The solid electrolyte interface forms an impedance barrier restricting ionic transport between the electrolyte and electrode and, in cells without a lithium metal anode, results in an irreversible loss of lithium atoms from the active electrochemical reaction and thus a reduction in accessible energy density.

2.2.2 Transition Metal Oxides

Lithium cobalt oxide (Li_xCoO_2) has been the predominant cathode paired with graphite for its high energy density and cycleability. O^{2-} ions form a nearly closed packed cubic lattice $(R\bar{3}m)$ with Li^+ and Co^{3+} occupying alternate octahedral sites between adjacent oxygen layers. Lattice parameters follow two distinct structural phases as lithium concentration varies, HEX-I ($x \leq 0.75$) and HEX-II ($x \geq 0.93$) [91, 92]. Theoretical studies predict highly anisotropic lithium diffusion occurring via a divacancy mechanism with prominent reductions in lithium mobility at $x = 0.5$ and $x = 0.66$ due to lithium-ion ordering [93, 94].

Favorable cycleability, however, is obtained only when x is restricted between 0.5 and 1 due to the instability of the residual cobalt oxide lattice. The consequent reduction in power density renders Li_xCoO_2 cathodes insufficient for automotive applications and has reenergized the search for alternate cathode configurations. Subsequent investigations have focused on the doping of $LiCoO_2$ with other transition

metals including Ni, Mn, Ti and Cr [95]. Alternate transition metal oxide synthesis methods which produce an alternate spinel ($Fd3m$) form such as $LT - Li_xCoO_2$ and $Li_xMn_2O_4$ supporting three dimensional transport have been recently proposed but the resulting cathode materials remain under study [96,97].

2.2.3 Olivine Phosphates and Sulfates

Lithium iron phosphate, Li_xFePO_4, and the associated lithium metal phosphates $Li_x[Mn, Co, Ni]PO_4$ and sulfates were recently proposed as potential successors to lithium cobalt oxide as cathodes with improved power density and exceptional rate characteristics [98, 99]. They posses an olivine structure described as a distorted hexagonal close-packed oxygen sub-array with Li, Fe and P atoms occupying interstitial sites to form FeO_6 and LiO_6 octahedra and tetrahedral PO_4 groups. The result is a series of curved one dimensional diffusion pathways along the [010] crystalline axis which give rise to rapid Li transport but are particularly susceptible to the influence of defects and blockages [56,100].

Lithium iron phosphate cells have seen considerable commercial adoption though remaining far below that of lithium cobalt oxide. Their decreased energy density is offset by improvements in lifetime, cycleability, power density, cost, toxicity, stability and safety. Though initially hindered by poor electrical conductivity, reductions in particle sizes and the introduction of conductive coatings were subsequently introduced to resolve the issue [101].

2.2.4 Integration Compounds

For the vast majority of intercalation compounds discussed above, lithium bonding is largely ionic occurring within an open host lattice structure. These relatively loose bonds allow for rapid lithium-ion transport and low activation energies for intercalation and de-intercalation with minimal strain on the host. There is an associated cost, however, in the reduced energy storage density as compared to close-packed lithium compounds in which lithium is covalently bonded as an integrated part of the host

38

lattice structure. The recent drive for expanded battery energy storage densities has renewed interest in such integration compound cathodes, namely the lithium-sulfur and lithium-air cells.

The lithium-sulfur cell has, as its base product under complete reduction, lithium sulfide, the material considered in this study and discussed in greater depth in the following chapter. Lithium-air cells have gained considerable recent interest for their exceptional energy density, up to 3000 Wh/kg, especially in automotive applications where the active cathode material can be accessed from the environment in the form of atmospheric oxygen [102, 103].

The lithium oxygen half reaction occurs in two parts producing lithium oxide and lithium peroxide, $Li^+ + e^- + 0.25\ O_2 \rightarrow 0.5\ Li_2O$ and $Li^+ + 0.5\ O_2 + e^- \rightarrow 0.5\ Li_2O_2$, respectively, at 2.96 V relative to Li metal. The production of lithium oxide is not reversible but may be suppressed through introduction of a suitable catalyst [104].

The lithium-air cell remains under rapid development though much progress has been made through the utilization of carbonaceous cathode frameworks which provide electrical conductivity and nucleation sites. However, several implementation challenges remain to be met before lithium-air cells can mature to commercialization [27]. At the cathode, the chief difficulty is the formation of precipitate and subsequent blockage of the orifices of the carbon framework which limits access to active reduction sites. The study and optimization of the transport of lithium ions and lithium peroxide precipitate within the carbon framework is an active area of research to maximize lithium uptake and in turn, achievable energy density. At the anode, difficulties arise due to reintroduction of a protected lithium metal electrode for increased energy storage density. Engineering of electrode structures and electrolytes to prevent access of atmospheric oxygen and water to the anode and the formation of dendrites remain to be addressed.

Material	Potential to Li/Li^+	Electrical conductivity	Paramagnet	$D\ (cm^2/s)$
Li_xC_6 (layered)	0.20 V	yes	no	$10^{-6} - 10^{-7}$ along graphene plane (ab-initio) [6,87] 10^{-11} along grain boundaries (ab-initio) [6,87] $2.0 - 3.4 \cdot 10^{-10}$ (SSCV) [16] $2.2 - 4.7 \cdot 10^{-10}$ (PITT) [85,86] $0.65 - 1.2 \cdot 10^{-10}$ (EIS) [83]
Li_xCoO_2 (layered)	3.9 V	for $x \lesssim 0.9$	for low x	$3 - 5.5 \cdot 10^{-12}$ (PITT) [35] $2.5 \cdot 10^{-13}$ (180K SLR NMR, $HEX - I$) [105,106] $1.4 \cdot 10^{-12}$ (400K SLR NMR, $HEX - II$) [105,106] $7 \cdot 10^{-11}$ (NMR) [107] $7 \cdot 10^{-10}$ ($x = 0.73$,μSR) [67,108] $2.5 \cdot 10^{-10}$ ($x = 0.53$,μSR) [67,108] $10^{-10} - 10^{-12}$ (ab-initio) [15,109]
Li_xNiO_2 (layered)	4.19 V		yes	$6 \cdot 10^{-9}$ (NMR) [105,107]
$LiMn_2O_4$ (spinel)	4.1 V	yes	yes	$3.4 \cdot 10^{-16}$ (345K Exchange NMR) [110]
Li_xFePO_4 (olivine)	3.45 V	no	yes	$10^{-10} - 10^{-16}$ (GITT/PITT) [111] $7.6 \cdot 10^{-11}$ (GITT/PITT, $x = 1$) [111] 10^{-8} (ab-initio) [100] $10^{-9} - 10^{-10}$ (μSR) [112] $1.8 \cdot 10^{-14}$ (GITT, $x = 1$) [53] $1.29 \cdot 10^{-14}$ (EIS, $x = 0.9$) [53]
$Li_xV_2O_5$ (orthorhombic)	3.3 V	no	yes	$10^{-8} - 10^{-11}$ (GITT, EIS) [113,114]
Li_2O_2 (hexagonal)	2.96 V	no	no	

Table 2.1: A collection of the kinetic and electronic properties of several important lithium-ion conductors. Reports of chemical diffusion coefficients, unless otherwise noted, were conducted at room temperature and describe the span of diffusion coefficients measured throughout the full range of accessible lithium concentrations.

Chapter 3

The NMR of Lithium Sulfide

This thesis investigates the transport properties of the lithium-ion conductor lithium sulfide, the fully reduced product of the redox reaction underlying the lithium-sulfur electrochemical cell. Sulfur is a promising next-generation lithium battery cathode material for its high theoretical energy density, low cost and weight, and fast reaction kinetics [115]. Although sulfur was one of the earliest materials considered for use as a cathode in lithium-ion batteries, several unfavorable properties were subsequently discovered including a large internal electrical resistance, high rate of cell self discharge, and high rate of capacity fade on cycling which, unaddressable at the time, rendered lithium sulfur cells unsuitable for further development [116–119].

Instead, several alternate battery chemistries utilizing lithium intercalation compound cathodes have been developed and have achieved widespread adoption in portable, low-current applications. After two decades of engineering and optimization, intercalation cathode batteries are approaching their theoretical maximum energy density of 300 mAh/g [14]. These capacities have proven insufficient for applications such as long range plug-in and hybrid automotive propulsion and grid scale energy storage and load leveling [120]. The growing need for an energy storage system capable of handling these workloads has renewed interest in lithium integration cathodes, such as sulfur and oxygen.

Integration compounds are distinguished from intercalation compounds by the nature of the chemical bonds through which lithium adheres to the cathode host

41

material; covalent for integration and ionic for intercalation. In intercalation compounds, Li^+ ions occupy interstitial sites within an existing host crystal lattice and so are easily removed or inserted during battery operation. In integration cathodes, lithium covalently bonds with the host material and thus more tightly integrates into the cathode structure resulting in a theoretical energy density far beyond that of intercalation cathodes [26, 27, 121, 122].

3.1 Lithium Polysulfides

In its most common form, elemental sulfur organizes as stacks of eight atom rings (S_8). As lithium is introduced, the sulfur-sulfur bonds are cleaved, opening the sulfur ring and introducing lithium bonds at each end. Further addition of lithium results in a continuing subdivision of the initial sulfur ring yielding the redox cascade $S_8 \leftrightarrow Li_2S_8 \leftrightarrow Li_2S_6 \leftrightarrow Li_2S_5 \leftrightarrow Li_2S_4 \leftrightarrow Li_2S_2 \leftrightarrow Li_2S$ [28]. The overall redox reaction $S_8 + 16\,Li^+ + 16\,e^- \rightleftharpoons 8\,Li_2S$ occurs at a potential of 2.15 V relative to lithium metal, approximately two-thirds that of transition metal oxide intercalation cathodes.

Of the polysulfides generated in the redox cascade, the first four are highly soluble in the polar organic solvents used in lithium battery electrolytes and the last two are not. During normal operation, the generation of the lower order polysulfides, and in particular, the conversion from the soluble Li_2S_4 to the insoluble Li_2S_2, occurs at a reduced rate due to the energy required for nucleation into the solid phase. In the solid phase, full reduction from Li_2S_2 to Li_2S, and access to half of the cell's potential energy density, is limited by the rate of lithium diffusion in the cathode bulk [123, 124].

While the soluble higher order polysulfides yield fast reaction kinetics, diffusion across the electrolyte results in a parasitic shuttle reaction which drastically reduces Columbic efficiency [124, 125]. Partially reduced sulfur ions diffuse through the electrolyte to the anode where they react directly with the lithium metal to form lower order polysulfides. On the following charge, these lower order polysulfides diffuse back to the cathode and are reoxidized. Irreversibility in this process through the

generation of the insoluble Li_2S_2 and Li_2S results in the accumulation of impedance layers on both electrodes and active mass loss from the cathode [126].

In hopes of addressing the difficulties discovered during the early investigations of lithium sulfur cells, recent research efforts have developed and studied novel sulfur cathodes to provide electrical conductivity, polysulfide containment, and increased active surface area [28, 115]. Cathode additives and solgel electrolytes have been investigated as means of increasing electrical conductivity and preventing polysulfide dissolution but have not yet achieved these goals without significant reductions in energy density and cyclability [127–130].

More recently, the development of nanostructured porous carbon/sulfur composites comprised of high pore-volume carbon super structures with 1D or 3D channels for lithium transport has renewed interest in sulfur as a lithium-ion battery cathode material [115]. Molten sulfur is readily drawn into the carbon structure by capillary forces, and shrinks upon solidification to provide channels for electrolyte and Li^+ ion flow. By constraining sulfur within the carbon framework, the shuttle mechanism is suppressed, the requisite electrical contact is provided, and full reduction to Li_2S or oxidation to S_8 is achieved within the carbon framework. Reversible capacities of 1320 mAh/g have been demonstrated with 99.9% efficiency on the first cycle. Due to the reduction of polysulfide concentration in the electrolyte, capacity fading is reduced and sustained reversible capacities of 1100 mAh/g have been achieved [131]. Subsequent studies have expanded to consider a wide range of carbon based host structure materials including meso-, micro-, and nano-porous carbon, single and multi-walled carbon nanotubes and graphene [132–137].

3.2 Sample Characterization

While much progress has been made in understanding the electrochemistry and thermodynamics of lithium-sulfur cells and in engineering host cathode structures to address their associated implementation challenges, much less is known about the mechanisms and influences of room-temperature lithium transport in sulfur cathodes.

Line	Fraction	Frequency (Hz.)	FWHM (Hz.)	Form
Narrow	0.0165 ± 0.0041	312.75 ± 4.22	414.76 ± 13.45	Lorentzian
Broad	0.9834 ± 0.0010	672.15 ± 5.01	10941.97 ± 85.35	Gaussian

Table 3.1: The fitting parameters extracted from a least-squares fit of the Li_2S equilibrium ^7Li spectrum shown in Figure 3-1 to a one Lorentzian, one Gaussian line shape. Magnitudes are expressed as fractions of the total spectrum area, frequency shifts are shown relative to a $LiCl$ (aq). reference, and line widths are specified as full peak widths at half height. The coefficient of determination was $R^2 = 0.9943$.

Neutron scattering, electrochemical impedance spectroscopy, and NMR relaxometry studies of high-temperature transport in lithium sulfide have been previously pursued due to interest in a highly diffusive superionic conduction phase occurring above $800\ K$ [58, 138–140]. Much remains unknown with regards to the room-temperature dynamics in Li_2S and so we performed a series of standard solid-state NMR experiments under conditions described in Section 4.3.

3.2.1 ^7Li NMR Spectra

The observed ^7Li static spectrum is shown in Figure 3-1, calibrated to an aqueous $LiCl$ reference sample. We observe two overlapping lines distinguished by their line widths and relative amplitude. A least-squares fit was performed to the sum of Gaussian and Lorentzian line shapes. Fitting parameters are shown in Table 3.1.

The width and Gaussian form of the broader line is consistent with the presence of a static dipole-dipole interaction and is in agreement with the 11.6 kHz line width expected from a second moments calculation of the dipolar line width [141]. The sharpness and Lorentzian form of the narrow line can be attributed to motional narrowing. Diffusing lithium nuclei which visit several lattice or interstitial sites during the duration of an NMR experiment will experience a partial averaging of the dipolar relaxation mechanism due to the spatial dependence of the dipole-dipole Hamiltonian, resulting in extended coherence times and a narrowed line width [141, 142].

Subsequently, a 30 kHz magic-angle spinning spectrum was obtained in an 11.75 T external field utilizing a commercial Bruker MAS probe. A comparison of the static
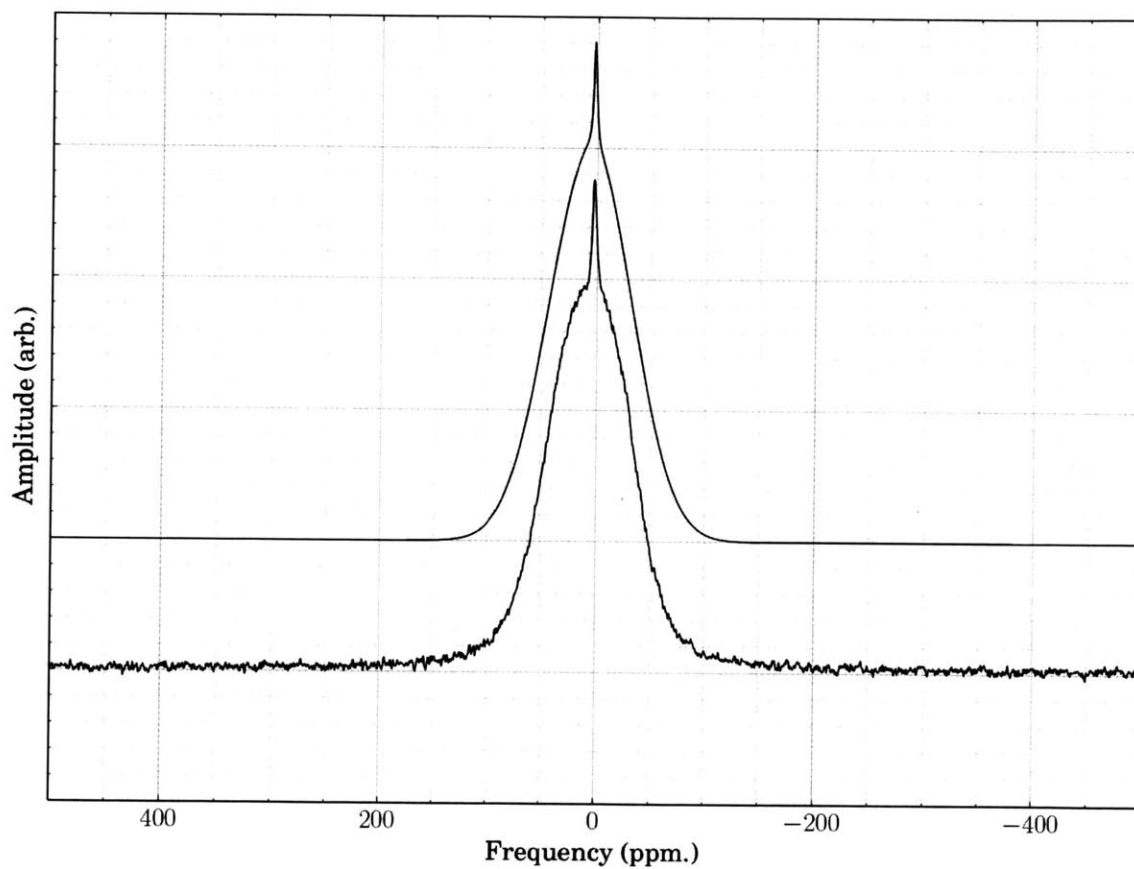
Figure 3-1: The room-temperature ^7Li static spectrum of lithium sulfide observed in a 7.05 T external field. The line shape resulting from a least-squares fit is shown offset above the spectrum. Parameters from the fit are shown in Table 3.1.
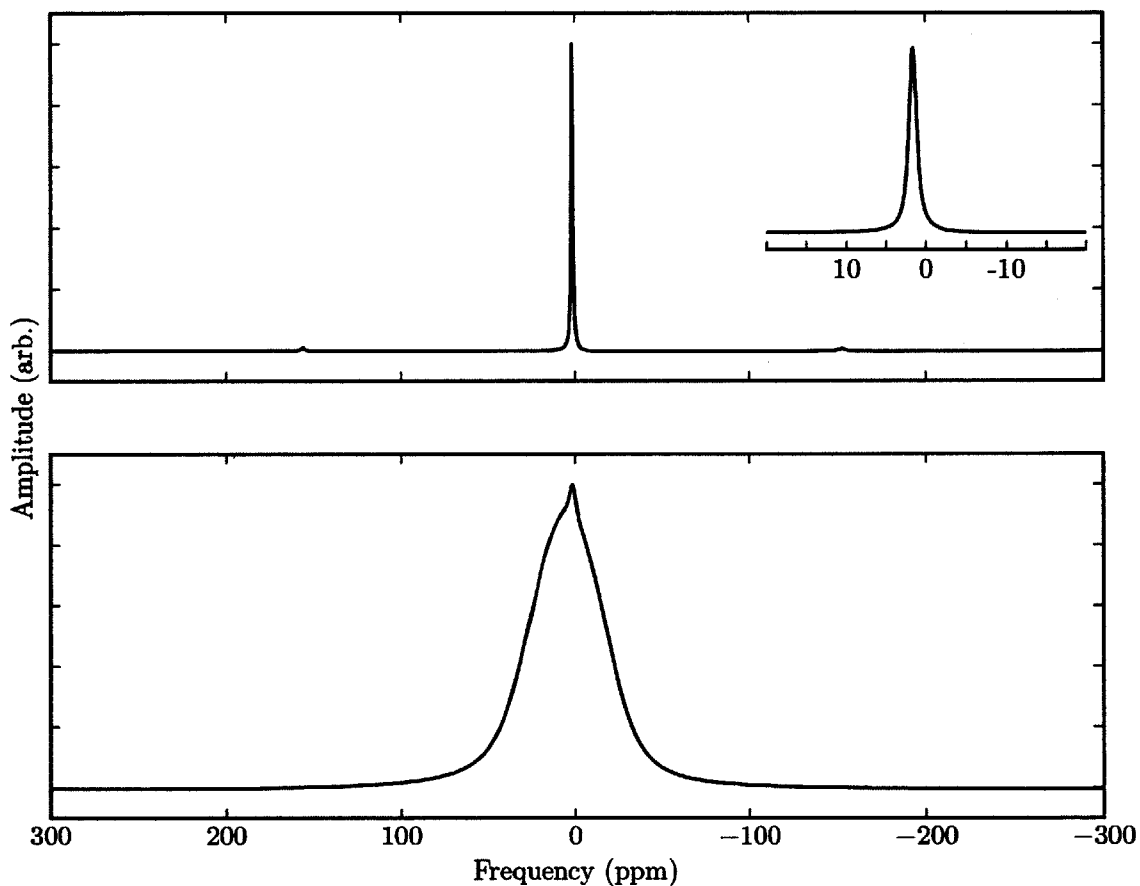
Figure 3-2: A comparison of the static (bottom) and 30 kHz magic angle spinning (top) ^{7}Li spectra for lithium sulfide in an 11.75 T external field. The inset enlarges the single central peak of the MAS spectrum. The static spectrum contains two overlapping lines which differ by more than an order of magnitude in line width and negligibly in chemical shift. Under MAS, the two lines collapse into a single 230 Hz line and a series of smaller spinning side bands. Amplitudes of the three plots are not to scale.

and 30 kHz MAS spectra is shown in Figure 3-2. The static line shape again contains two lines of drastically different line width and amplitude, collapsing into a single peak under MAS.

3.2.2 Longitudinal Relaxation

To investigate the longitudinal relaxation processes of the two observed lines, we performed inversion recovery and saturation recovery experiments. The saturation recovery experiment utilized a train of 32 $\pi/2$ pulses spaced 1 ms apart, followed by a variable-length recovery period and observation pulse. A standard inversion recovery sequence was employed with a logarithmically incremented recovery time, and a cycle time of 180 s. The narrow and broad peaks were observed in separate experiments with a Hahn echo sequence employed to ensure a flat baseline for the observation of the narrow line. The results of these experiments are shown in Figures 3-3 and 3-4 for the narrow and broad lines, respectively.

The non-linearity of the narrow line inversion recovery curve on the semilog amplitude plot indicates the presence of a two-exponential recovery mechanism. Additionally, disagreement between the slopes of the narrow line inversion and saturation recoveries is observed. For the broad line, both the inversion and saturation recoveries are well described by a single exponential relaxation process and no strong discrepancy is seen between the saturation and inversion recovery curves.

The observed behavior is potentially explained by the presence of chemical exchange. In order to confirm and quantify the presence of an exchange process between the narrow and broad lines, we performed a series of NMR relaxometry experiments which are reported in the following chapter.
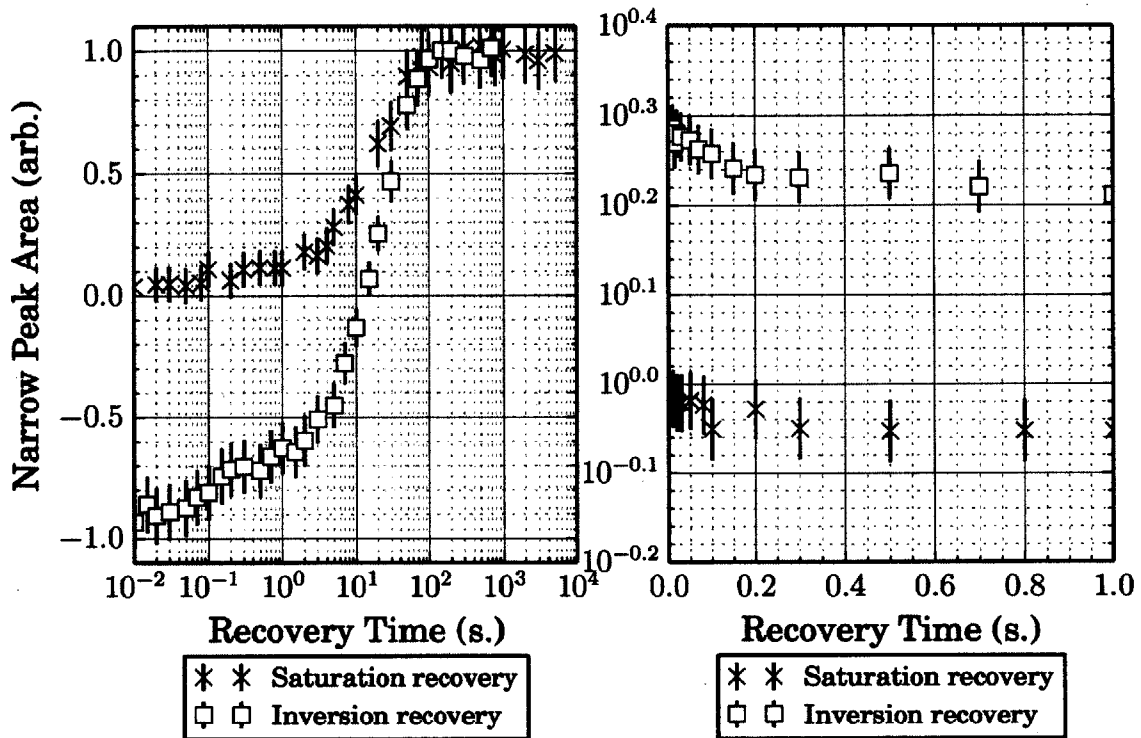
Figure 3-3: Semilog time and semilog attenuation plots of the Li_2S narrow line saturation and inversion recovery curves. A two exponential recovery of the narrow line magnetization is apparent from the non-linearity of the semilog attenuation curve, and the disagreement of the slopes for inversion and saturation recovery experiments strongly indicates the presence of an exchange process. Curves are normalized to the equilibrium line magnitude.
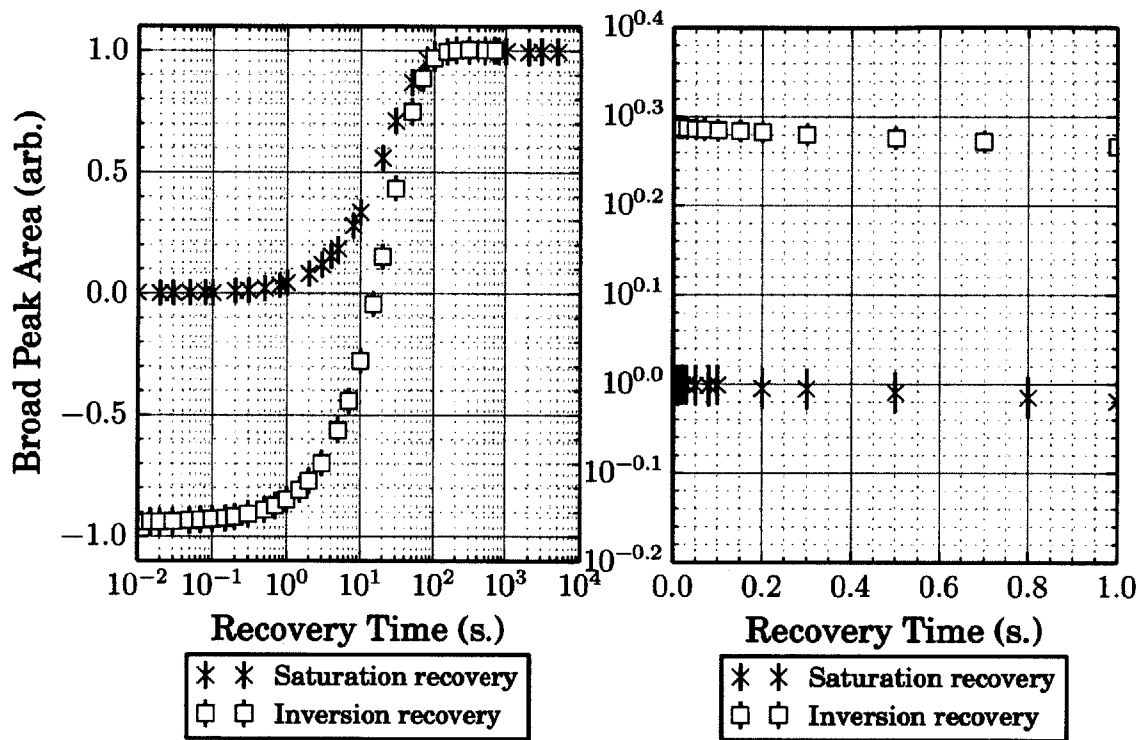
Figure 3-4: Semilog time and semilog attenuation plots of the Li_2S broad line saturation and inversion recovery curves. Unlike the narrow line, the recovery of the broad line does not show a strong deviation from single exponential relaxation. Curves are normalized to the equilibrium magnitude and error bars, where not shown, are smaller than data markers.

Chapter 4

Exchange Spectroscopy of Lithium Sulfide

Many technologically important materials which appear static under macroscopic observation show more dynamic behavior on molecular length scales. One class of finite-temperature microscopic process which drives such dynamics is chemical exchange processes. These processes stochastically modulate the local chemical environment of atoms within a molecule and as a result may significantly impact the macroscopic thermodynamic and kinetic equilibrium properties of materials. This class of processes includes, for example, molecular reorientations between locally stable configurations and ionic and vacancy hopping amongst lattice and interstitial sites in a disordered crystal [143].

When these processes modify the magnetic environment of a nucleus, the influence of the exchange process will appear in that nucleus' NMR spectra through a manifestation determined by the relative time scales of the active NMR and exchange processes. Systematic observation of this influence allows for the determination of temperature dependent hopping rates, pathways of a given exchange process and activation energies of transport processes through the Arrhenius and Eyring equations [144, 145].

Given the prevalence of lithium-ion mobility and host lattice disorder in lithium-ion conductors, chemical exchange is frequently observed and has been utilized to

investigate the lithium-ion hop mechanisms underlying macroscopic lithium-ion mobility in several lithium battery electrode materials [110, 146–149].

The two exponential spin-lattice recovery of the narrow and broad lines of lithium sulfide and the dependence of the recovery rates of each line on the initial spin states of the baths, as observed in Chapter 3, indicate the presence of an exchange process. To quantify the rates of exchange and extract the intrinsic spin-lattice relaxation rates, we perform a modified version of the 1D exchange spectroscopy (EXSY) selective inversion recovery experiment [150, 151].

Beyond the usefulness of determining exchange rates for structural studies and mapping energetics of mobility pathways, the exchange rates and intrinsic relaxation rates are required for analysis of the diffusion measurements presented in Chapter 5. The stimulated echo diffusion experiment relies upon accurate measurements of signal attenuation due to diffusion in an inhomogeneous magnetic field. In order to isolate the component of the echo attenuation due to diffusion, accurate knowledge and a corresponding mathematical model of all other attenuation mechanisms are required. Moreover, if the exchange process brings a spin to multiple sites with different intrinsic diffusion coefficients during the diffusion time, knowledge of the residency times on each site will be required to extract the intrinsic mobility properties of each individual site from the apparent bulk transport properties [152, 153].

4.1 Signatures and Models of Exchange

Exchange processes which alter the magnetic environment of a nuclear spin within the timescale of an NMR experiment will have a pronounced effect on the NMR spectrum [154]. Depending on the relative scale of the exchange and relaxation rates, exchange can be manifest in NMR spectra in one of several ways, though a single physical phenomenon underlies each.

In general, an exchange processes randomly alternates a nuclear spin between the distinct magnetic environments of the exchanging sites or configurations. The resulting microscopic spin dynamics are dictated by a series of evolutions under the

spin Hamiltonians of each site with duration and order determined by the random jumps of the exchange process. The macroscopic sample response is the coherent sum over many realizations of the exchange random process.

Sites undergoing rapid exchange on a time scale short compared to T_2 and the inverse chemical shift difference, for example, will appear as a single site with properties derived from a residency-time weighted average of the constituent sites, resulting in a coalescence of the exchanging lines in the observed spectrum [154]. Exchange rates on the order of T_2 can be directly measured in the 2D EXSY experiment through the buildup of cross peak volume as a function of the mixing time [79, 155].

Slower exchange processes, on the order of T_1, will result in a modification of spin-lattice relaxation curves as spins alternate during the relaxation time between the relaxation processes of each site [150, 151, 156]. For two exchanging sites, each with an intrinsic single T_1 relaxation process, the resulting relaxation curves will be a product of two exponentials with effective T_1 rates and coefficients determined by the exchange rates, relative bath sizes, and the initial state of each bath [143].

Despite the breadth of manifestations of chemical exchange in NMR spectra, a simple modification to the Bloch equations, inspired by a heat bath model, is sufficient to capture the influence of exchange dynamics across the full range of time scales [157–159]. An earlier description of exchange processes modeled the microscopic site hopping as a stochastic Markov process with jump rates determined by the exchange rates [160]. This model has been shown to yield the same macroscopic system response as the modified Bloch equations derived by McConnell [161].

4.1.1 The Heat Bath Model

The semi-classical picture of NMR dynamics under chemical exchange which underlies the McConnell modifications to the Bloch equations is that of two coupled spin baths, each described by a set of intrinsic properties such as chemical shift, relaxation rates, and diffusion coefficients. A member spin of bath i will evolve according to the properties intrinsic to bath i and will be included in the coherent sum for bath i's intensity in the observed spectrum. An exchange process can be modeled by a series

52
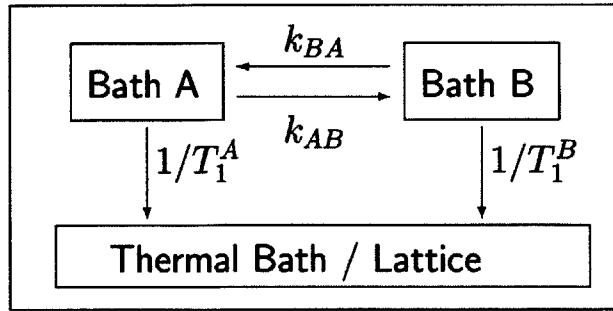
Figure 4-1: A graphical depiction of the two bath, dissipative exchange model. Spin and transport dynamics in each bath evolve according to the intrinsic properties of that bath. Spins in each bath posses a rate of flow to the other bath and into the lattice degrees of freedom.

of instantaneous jumps of a spin from bath i to bath j, at which point the spin will evolve with the properties intrinsic to bath j.

If the rate of exchange is very slow compared to the longest NMR time scale, the T_1's of the baths, the baths will evolve independently during the course of the NMR experiment. Likewise, if the rate of exchange is much faster than the NMR time scales describing the baths, the observed NMR signal resulting from the exchanging baths will not be distinguishable from that of a single effective bath with properties given by an occupation-time weighted average of the properties of the physical baths. Intermediate regimes will show more complex behavior with spins iterating between periods of evolution resident in each of the exchanging baths. Spin dynamics in these regimes can be described through a set of differential rate equations which unify the description of the evolution of magnetization and its exchange driven flow between the exchanging baths.

Considering the macroscopic spin evolution of the M_z component of bath i as described by the McConnell equations in the absence of RF irradiation yields

$$\frac{dM_{zi}(t)}{dt} = -\frac{M_{zi}(t) - M_{zi}(\infty)}{T_{1i}} + \sum_{\substack{baths \\ j \neq i}} \left(k_{ji} M_{zj}(t) - k_{ij} M_{zi}(t) \right). \qquad (4.1)$$

T_{1i} is the relaxation rate intrinsic to site i, the spin-lattice relaxation rate that site would display in the absence of any exchange processes and the summation is taken

over each pair of exchange-coupled baths. The M_x and M_y components are similarly modified but are not included here as only the dynamics of exchange slower than $1/T_2$ are of interest for this study.

By asserting that experiments be conducted at chemical equilibrium, the principle of detailed balance ensures that the ratio of the forward and reverse exchange rates is equal to the ratio of the occupancy of the destination and source baths. For an exchange process

$$A \underset{k_{BA}}{\overset{k_{AB}}{\rightleftharpoons}} B, \tag{4.2}$$

one can define an equilibrium constant K such that

$$K \equiv \frac{[B]}{[A]} = \frac{k_{AB}}{k_{BA}} = \frac{M_{0B}}{M_{0A}}. \tag{4.3}$$

In NMR spectra, the equilibrium concentrations can be inferred from the relative peak areas of the equilibrium spectrum. From the spectra shown in Section 3.2.1, we determine the equilibrium constant K of Li_2S to be 0.0160 ± 0.00105 for the narrow to broad exchange reaction.

4.1.2 Spin Dynamics under Exchange and Spin Lattice Relaxation

The set of coupled differential equations presented in Equation 4.1 can be rephrased in a master equation formalism so as to appear more amenable to solution under simple linear algebra. For a system of N exchanging baths, the magnetization evolution is governed by

$$\frac{\partial}{\partial t} \begin{bmatrix} M_1(\infty) - M_1(t) \\ \vdots \\ M_n(\infty) - M_n(t) \end{bmatrix} = -A \begin{bmatrix} M_1(\infty) - M_1(t) \\ \vdots \\ M_n(\infty) - M_n(t) \end{bmatrix} \tag{4.4}$$

where A is the rate matrix describing both the intrinsic relaxation rates of each site and exchange rates to all other sites as

$$A = \begin{bmatrix} R_1 & -k_{21} & -k_{31} & \cdots & -k_{n1} \\ -k_{12} & R_2 & -k_{32} & & -k_{n2} \\ -k_{13} & -k_{23} & R_3 & & -k_{n3} \\ \vdots & & & \ddots & \vdots \\ -k_{1n} & -k_{2n} & -k_{3n} & \cdots & R_n \end{bmatrix} \tag{4.5}$$

with

$$R_i = \frac{1}{T_{1i}} + \sum_{i \neq j} k_{ij}. \tag{4.6}$$

The solution to this set of coupled differential equations can be shown to be

$$\begin{bmatrix} M_1(\infty) - M_1(t) \\ \vdots \\ M_n(\infty) - M_n(t) \end{bmatrix} = e^{-At} \begin{bmatrix} M_1(\infty) - M_1(0) \\ \vdots \\ M_n(\infty) - M_n(0) \end{bmatrix} \tag{4.7}$$

where the exponential of A can be computed through its eigendecomposition. For two and three site exchange, the rate matrix A matrix can be diagonalized algebraically to a yield closed form, if cumbersome, solution.

For two site exchange, the general solution to Equation 4.7 can be shown to be

$$\begin{aligned} M_1(t) = M_1(\infty) \\ -\frac{1}{\Delta} \left[e^{-(a+d)t/2} \left(\Delta \cosh(\frac{\Delta}{2}) - t(a-d)\sinh(\frac{\Delta}{2}) \right) (M_1(\infty) - M_1(0)) \right. \\ \left. -2tbe^{-(a+d)t/2} \sinh(\frac{\Delta}{2}) (M_2(\infty) - M_2(0)) \right] \end{aligned} \tag{4.8}$$

with

$$\begin{aligned} a &= 1/T_{11} + k_{12} \\ b &= -k_{21} \\ c &= -k_{12} \\ d &= 1/T_{12} + k_{21} \\ \Delta &= \sqrt{t^2(a-d)^2 + 4bct^2}. \end{aligned} \tag{4.9}$$

It is clear from Equation 4.8, that the relaxation behavior of a given bath will be strongly dependent on the relative bath sizes, relaxation rates, exchange rates, and initial states. Of these, the initial magnetization states are easily varied experimentally and thus it is possible to select a subset of initial magnetization states such that the observed evolution will allow determination of the relative exchange rates and intrinsic relaxation rates. This is the basis of the 1D EXSY experiment.

4.2 The 1D EXSY Experiment

The dependence of the magnetization recovery of each bath on the intrinsic relaxation rates, exchange rates, and initial bath magnetization as described in Equation 4.8 allows one to selectively isolate and measure the elements of A by appropriately selecting a series of bath initial conditions and observing the resulting return to equilibrium [162, 163]. By comparing the observed recovery curves of both baths to the numerical model above, a direct measure of the intrinsic relaxation and exchange rates is obtained.

This technique has recently been employed in study of the lithium-ion conductor Li_2VPO_4F which displays two ^6Li lines separated by 93 ppm under 40 kHz MAS [148]. By allowing an evolution period of $1/(2\Delta\nu_{AB})$ between an initial broadband excitation and a second broadband $\pi/2$ rotation, the on-resonance species is inverted and the off-resonance species is returned to its equilibrium orientation. A mixing period follows in which the return to equilibrium of the inverted species can be compared against the recovery profile in the case of non-selective inversion. A means of selecting the optimal initial states to distinguish the relaxation and exchange quantities has been proposed in [164].

The selective inversion method does not directly apply to Li_2S as there is no discernible chemical shift difference between the two lines, even under 30 kHz MAS, so performing a selective rotation on only one of the two overlapping lines is not possible. However, the difference in the response of the two lines to standard refocusing sequences and their vastly different T_2's are sufficient to reach a selection of initial

states suitable for exchange characterization. For the investigation of exchange in lithium sulfide, a non-selective saturation recovery, non-selective inversion recovery, selective saturation of the broad line, and a selective saturation of the broad line and inversion of the narrow line are chosen as initial states. The pulse sequences utilized to generate each of these states are shown in Figure 4-2.

4.3 Experimental Procedure and Results

Observation of the ^7Li Li_2S recovery curves was performed in a 7.05 T superconducting magnet using a Bruker 300 MHz Avance spectrometer and a homebuilt two-axis quadrupole gradient probe. The ^7Li nucleus is preferred for its larger natural abundance and gyromagnetic ratio, as justified in Chapter 5. Powder samples prepared as described in Chapter 3 were utilized for all experiments.

To generate the selection of initial states required, a series of preparation sequences was performed, followed by a storage pulse. A magnetization recovery time was allowed followed by a solid echo or Hahn echo pulse sequence to allow selective observation of the broad or narrow line, respectively. Limiting the final spectrum to only one of the two lines simplifies and reduces error in the extraction of the resultant line magnitude.

Non-selective saturation was achieved with a train of 32 $\pi/2$ pulses spaced 3 ms apart. Selective saturation of the broad line was achieved through a Hahn echo sequence with an echo time of 1 ms followed by a $\pi/2$ storage pulse with phase chosen to either invert the narrow line magnetization or restore it along the equilibrium direction. The recovery spectra for each of the four pulse sequences are shown in Figures 4-3 and 4-4.

Peak areas were extracted from the resulting spectra using a non-linear least-squares regression to a Gaussian or Lorentzian line shape model with frequency and line width parameters fixed from the equilibrium spectrum. The resulting peak amplitudes were then supplied to a three parameter non-linear least-squares regression of the two bath exchange model described in Section 4.1.2 to extract the forward ex-
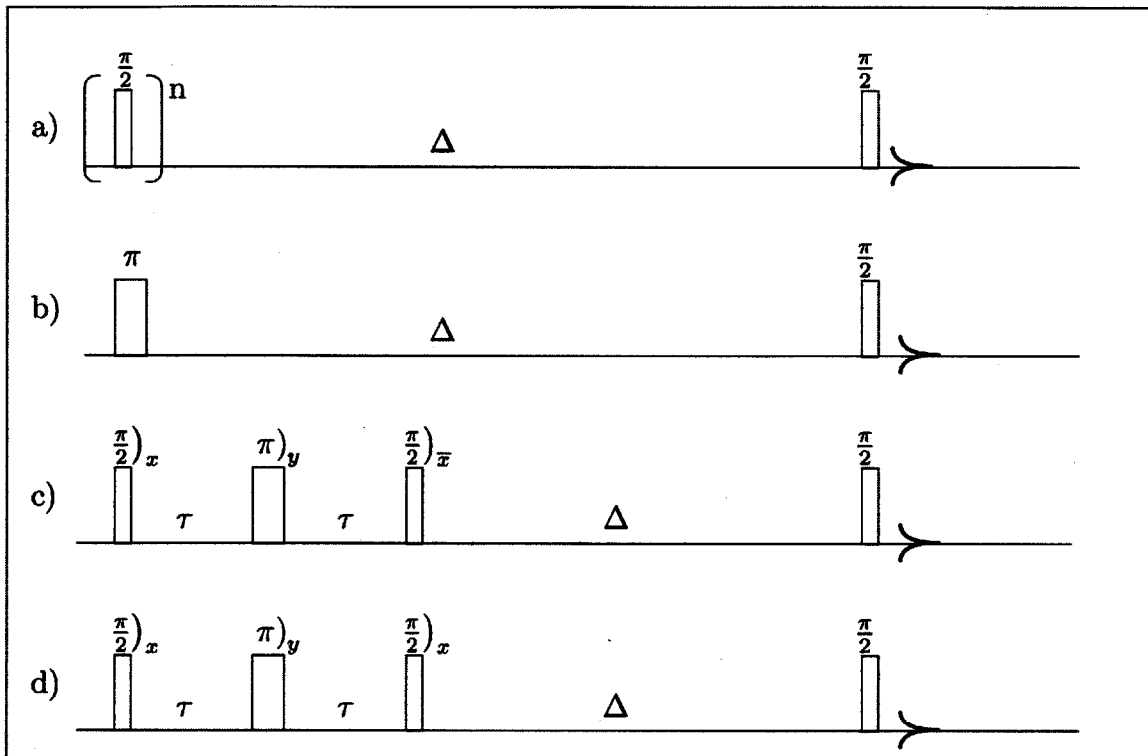
Figure 4-2: Diagrams of four state preparation pulse sequences used in the acquisition of exchange influenced recovery curves. a) Non-selective saturation recovery, b) non-selective inversion recovery, c) saturation of the broad line and restoration of the narrow line, and d) saturation of the broad line and inversion of the narrow line.

change rate and intrinsic T_1's, as described in [165]. The exchange rate for the reverse reaction is calculated from the equilibrium peak areas as described in Equation 4.3. The extracted peak amplitudes and resulting fit are shown in Figures 4-5 and 4-6 for the narrow and broad lines, respectively.

4.4 Analysis and Discussion

Figures 4-5 and 4-6 compare the recovery rates of the narrow and broad lines across all prepared initial states. As predicted for the relative bath sizes, the influence of the narrow line initial state on the broad line recovery is imperceptible. Conversely, the influence of the initial state of the broad line on the evolution of the narrow line is dramatic. Moreover, the transient dip in the restored narrow line recovery is strongly indicative of exchange. None of the observed recovery curves are well fit to a single exponential decay, but rather a two exponential decay with time constants determined by the exchange rates and intrinsic T_1's, and coefficients determined by the initial states of each bath.

The intrinsic T_1's and the exchange rates were obtained from a non-linear least-squares regression of the recovery curve amplitudes to the model presented in Section 4.1.2. The measured narrow line intrinsic T_1^N is 1.24 ± 0.034 s and the broad line intrinsic T_1^B is 32.85 ± 0.496 s. The exchange rate from the narrow to broad bath was $k_{NB} = 7.505 \pm 0.0145$ Hz and when combined with the bath magnitudes as drawn from the equilibrium spectra yields a rate for the reverse reaction $k_{BN} = 0.120 \pm 0.0033$ Hz. The values of the two bath exchange model evaluated with these fitting parameters are shown as solid lines in Figures 4-5 and 4-6 for the narrow and broad bath, respectively.
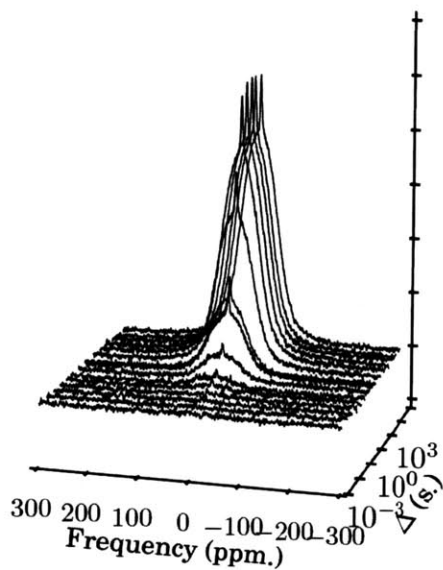
59

Non-selective saturation   **Non-selective inversion**
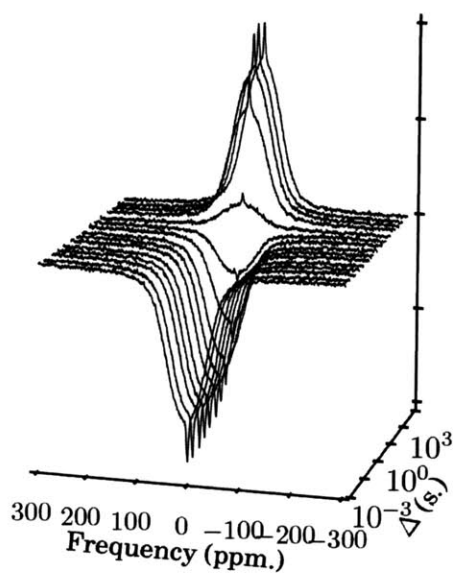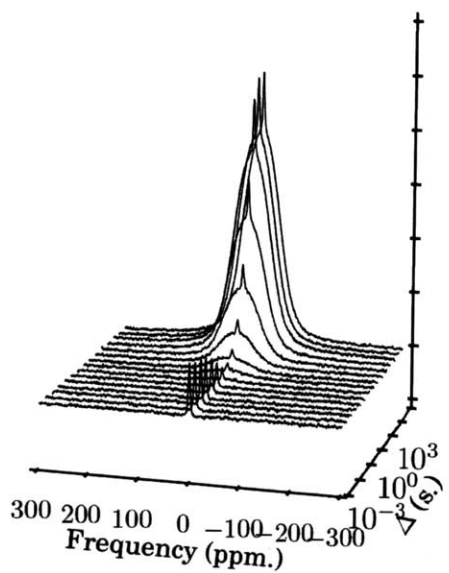
Restore narrow,   **Invert narrow,**
saturate broad   **saturate broad**
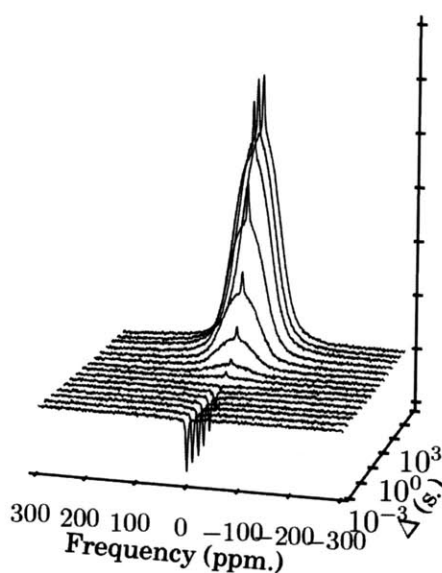
Figure 4-3: Full line Li_2S recovery spectra for each of the four initial magnetization states. For these trials, only a single $\pi/2$ pulse was applied after the recovery time so that both the broad and narrow line resonances are present.

Non-selective saturation   **Non-selective inversion**
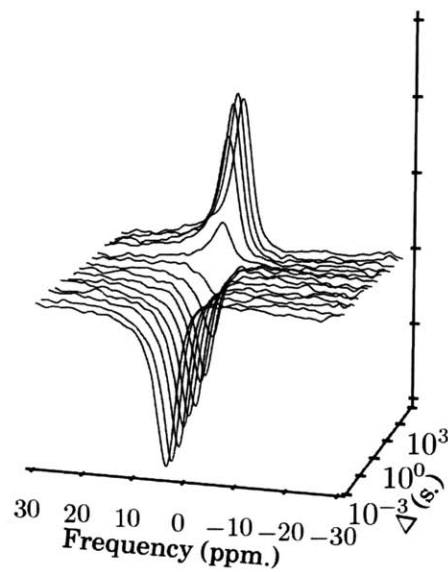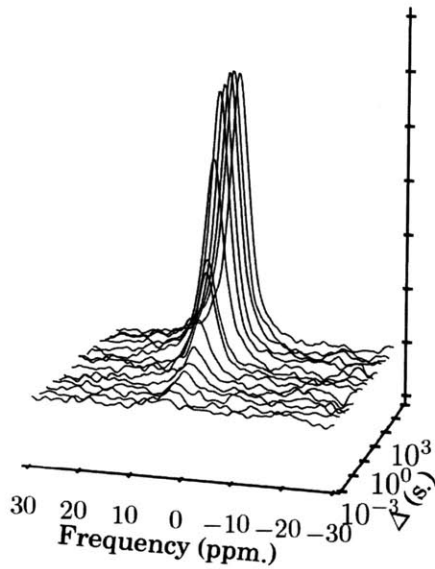
Restore narrow,   **Invert narrow,**
saturate broad   **saturate broad**
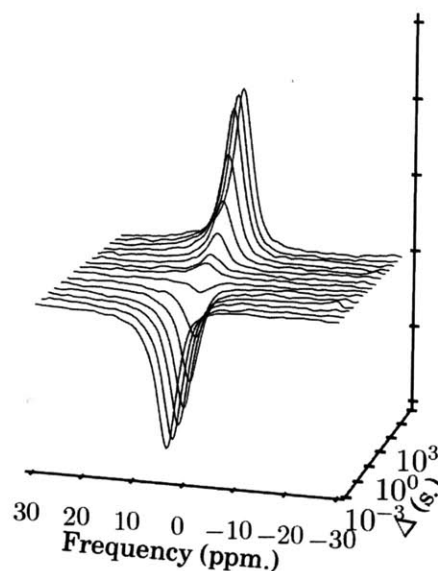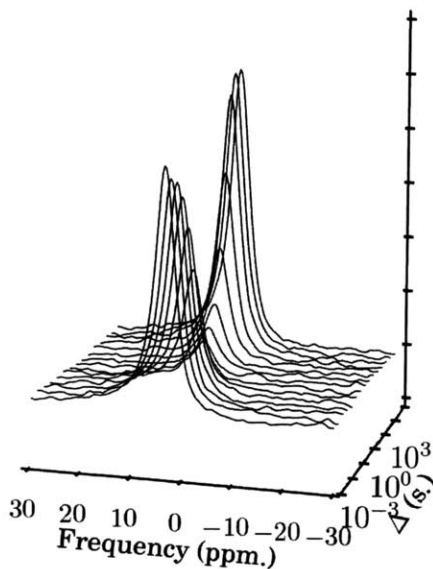
Figure 4-4: Narrow line Li_2S recovery spectra for each of the four initial magnetization states. For these trials, a Hahn echo sequence was applied following the recovery period so that only the narrow peak remains. The dip of the narrow peak following saturation of the broad peak and the deviation of the recovery of the inverted narrow peak in the presence of a saturated as compared to the presence of an inverted broad peak are clear indicators of exchange.
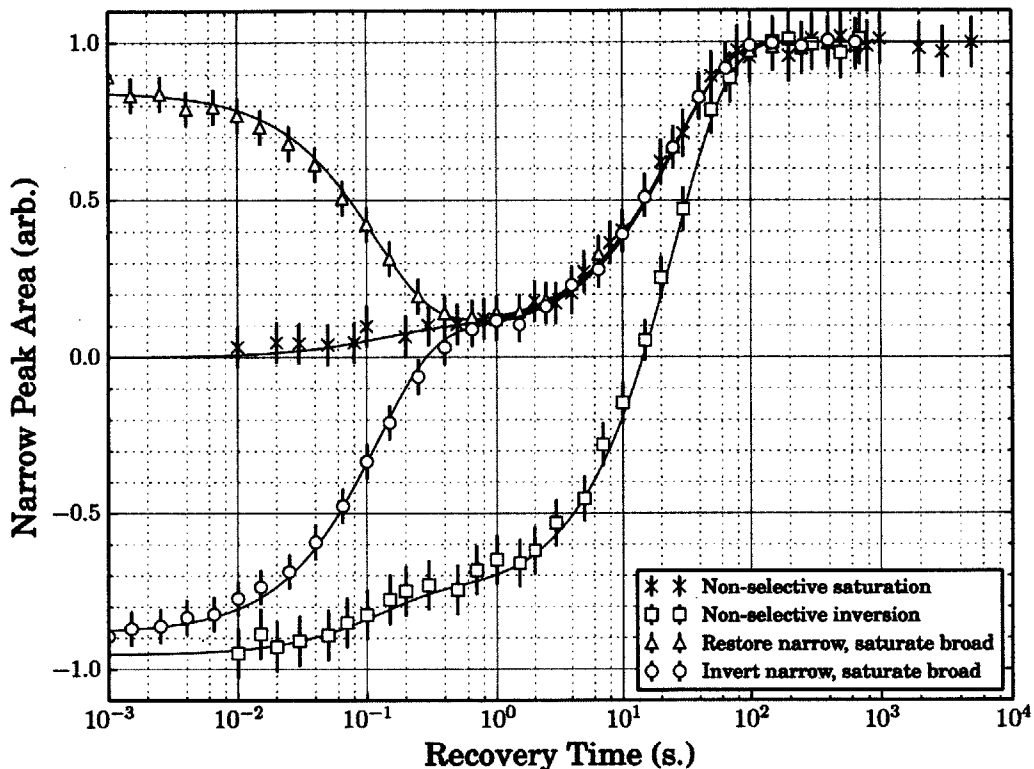
Figure 4-5: A plot of the narrow resonance magnitudes for the 1D EXSY experiments of Li_2S under varied initial magnetizations as extracted from a Lorentzian line shape fit. Solid lines show the results of a three parameter nonlinear least-squares fit of the two site exchange model of Equation 4.8 with independent T_1's and fixed inter-site exchange rates to the observed narrow and broad line relaxation curves. The presence of exchange is highlighted by the transient dip of the restored narrow line following saturation of the broad line and the dependence of the narrow line responses to inversion on the state of the broad line.
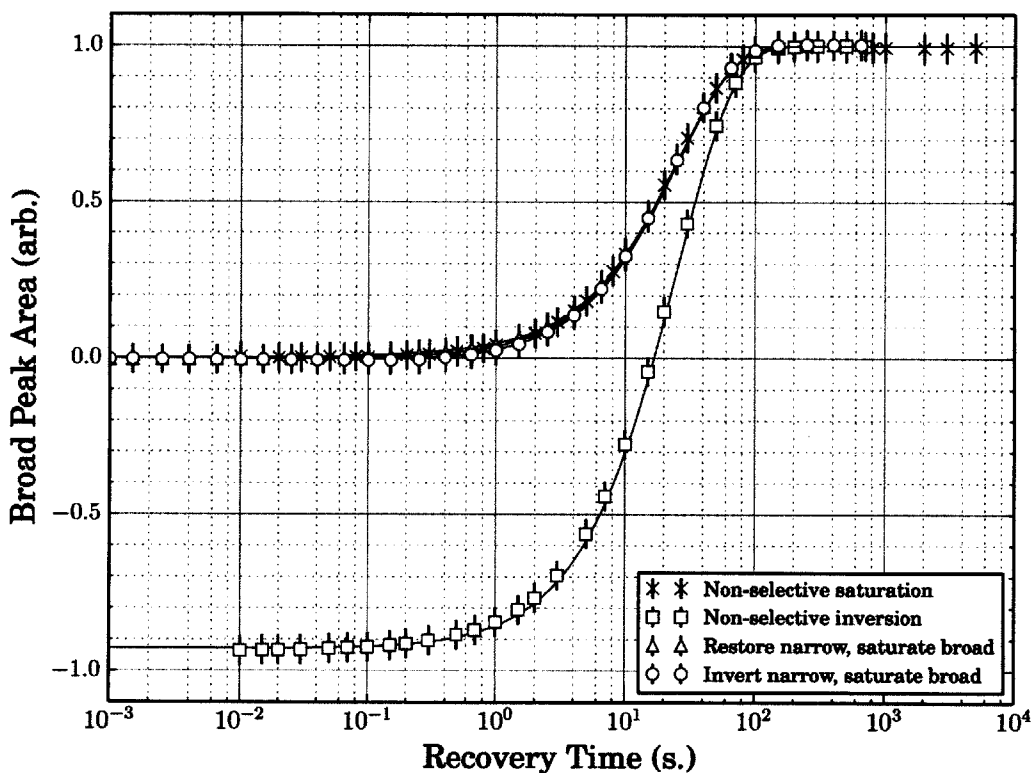
Figure 4-6: A plot of the broad resonance magnitudes for the 1D EXSY experiments of Li_2S under varied initial magnetizations as extracted from a Gaussian line shape fit. Solid lines show the results of a three parameter nonlinear least-squares fit of the two site exchange model of Equation 4.8 to the observed narrow and broad line relaxation curves. The influence of the initial magnetization state of the narrow line on the relaxation of the broad line is negligible, as expected given the relative bath sizes.

Chapter 5

Stimulated Echo Diffusion Measurements

The spatial dependence of the applied magnetic fields in NMR spectroscopy is generally minimized so as to increase sensitivity to local, atomic scale magnetic interactions. A spatially independent spin Hamiltonian, however, generates only position independent evolution and so leaves ensemble NMR measurements, in the absence of any other spatially dependent phenomena, insensitive to relative location or transport dynamics. Sensitivity to spatial degrees of freedom can be reintroduced through the controlled application of a magnetic field gradient of known geometry. The resulting spatial dependence of the spin Hamiltonian generates spatially dependent evolution which can be used to encode spatial information on to the nuclear spin degree of freedom and thus provide access to ensemble statistics of the transport of individual nuclei.

A diffusion process, in the presence of a magnetic field gradient, causes the spin location and thus Larmor frequency to become stochastically time dependent. Ensuing spin evolution yields a net phase accumulation determined by the diffusive path traveled [166]. The accumulated phase disorder across a macroscopic sample provides a direct signature of the transport of the nucleus under study [167].

NMR measurements of diffusion have been widely applied in liquids and gases where long spin coherence times and fast diffusion rates make possible measurements

of diffusion with only modest requirements on gradient strength. NMR measurements of diffusion in liquids have been demonstrated for determining the sizes and shapes of molecules and molecular aggregates, in examining the microgeometry of porous materials, imaging of diffusion profiles and enhancements of sensitivity to slow diffusion through multiple quantum spectroscopy have been demonstrated [19]. Further, if gradient fields can be switched during the course of an experiment, the chemical sensitivity of NMR spectroscopy can be combined with its sensitivity to transport dynamics to yield chemically resolved transport measurements specific to individual atomic sites or subspecies [168-171].

The application of spatially sensitive NMR methods to solids, however, has proven considerably more challenging. Slow diffusion rates and short coherence times limit both the time for growth of the phase encoding and the expected diffusive path length [23,172,173]. Through recent efforts in the application of coherent control sequences [48,174-176] and novel gradient design [49,177], NMR field gradient methods have recently found application in measurements of spin diffusion [177,178], high-temperature diffusion in proton and fluorine ion conductors [20,179], diffusion in plastic crystals [46], and solids imaging [48,180]. However, other applications, such as room-temperature diffusion measurements of low-γ nuclei remain challenging.

5.1   The Magnetization Grating

Magnetic resonance diffusion measurements utilize the nuclear spin degree of freedom as a flag or tracer of relative motion. Spin interactions are largely decoupled from transport dynamics and so provide an ideal cursor for probing motion unaffected by any manipulation of the nuclear spin [19]. Furthermore, as the application of a magnetic field gradient produces no chemical gradient, NMR diffusion measurements provide direct access to the free diffusion coefficient.

An excited nuclear spin placed in a strong external magnetic field will undergo precession at the Larmor frequency

$$\omega(\vec{r}) = -\gamma B_z(\vec{r}). \tag{5.1}$$

To generate spatially dependent spin evolution, a magnetic field gradient of known geometry is applied in conjunction with the uniform field such that $\omega(\vec{r})$ is explicitly a function of position. In the presence of a general field gradient

$$\vec{G} = \frac{\partial B_z}{\partial x}\hat{x} + \frac{\partial B_z}{\partial y}\hat{y} + \frac{\partial B_z}{\partial z}\hat{z}, \tag{5.2}$$

the position dependent Larmor frequency is

$$\omega(\vec{r}) = -\gamma(B_0 + \vec{G} \cdot \vec{r}). \tag{5.3}$$

During a period of free precession under the gradient field, spins accumulate a total phase

$$\phi(\vec{r}) = \gamma t \vec{G} \cdot \vec{r} = \vec{k} \cdot \vec{r} \tag{5.4}$$

where we define a wave number $\vec{k}$ to quantify the formation of a magnetization grating [181–183].

The net result is a position dependent phase rotation, usefully visualized as a magnetization helix with a pitch

$$\Lambda = 2\pi/(\gamma g t) \tag{5.5}$$

which defines a lower bound of the length scale on which NMR measurements may be sensitive to transport processes.

5.2 Influence of Diffusion on the Magnetization Grating

For any spin species in the presence of a gradient field, rapid phase decoherence is expected due to the distribution of local field strengths and thus Larmor frequencies.

Thus, an echo sequence is desired to recover initial coherence and produce a measurable signal after an extended evolution. Consider a gradient echo produced by means of an instantaneous negation of the amplitude of the gradient field half way through the free evolution period. In the absence of diffusion, each spin experiences local fields of equal and opposite amplitudes during the first and second evolution periods and thus undergoes no net phase rotation. Though local field strengths differ throughout the sample, the matching of the phase rotations during the first and second periods for all spins individually yields, in the absence of other relaxation mechanisms, a completely refocused echo.

The introduction of diffusion will, in general, break this matching condition as spins can no longer be assumed to reside in a single location throughout the evolution. Diffusion during each gradient evolution period will cause the accumulated phase to become a function of the stochastic trajectory of the diffusing spin. The degree to which this matching condition is violated, realized as individual residual phase rotations and the growth of ensemble phase disorder and thus attenuation of the resulting echo signal, is a direct signature of the diffusion process under study [167].

The Hahn echo diffusion measurement is an implementation of the above with a π rotation substituted for the gradient field inversion, easing the gradient switching requirement. Assuming a Gaussian diffusion process, the echo attenuation due to diffusion can be expressed as

$$\frac{M}{M_0} = e^{-2D\gamma^2 g^2 \delta^3/3} \tag{5.6}$$

where D is the diffusion coefficient, g is the applied field gradient strength, γ is the gyromagnetic ratio, and δ is the duration between the initial excitation and π pulse, half the total diffusion time.

For samples in which T_1 is much greater than T_2, the stimulated echo diffusion measurement is preferred for an extended diffusion period at the expense of a factor of two reduction in signal amplitude. The stimulated echo diffusion measurement begins with an RF excitation pulse followed by the application of a short, intense gradient

pulse generating a magnetization helix of fixed pitch. A second RF pulse returns the spins to alignment with the external field while preserving the phase encoding created during the gradient pulse. The remaining transverse magnetization components decay away in a time T_2, much shorter than the diffusion time, and may be neglected. The spins, now aligned or anti-aligned with the external field, are allowed a long period of free diffusion limited by T_1. Following the diffusion period, a final RF pulse returns the spins to the transverse plane in preparation for a decoding step implemented by a gradient pulse of equal magnitude to the first. If the diffusion period is substantially longer than the gradient pulse length, diffusion during the gradient pulses may be neglected [184].

A spin which has been translated along the gradient axis during the diffusion time will be left with a residual phase due to the mismatch of the rotations imparted by the encoding and decoding gradient pulses, given by

$$\phi_r = \gamma g t(z_i - z_f) = k(z_i - z_f) \tag{5.7}$$

with z_i and z_f the initial and final positions of the diffusing spin along the gradient axis, respectively.

Consider the evolution of a net complex magnetization $\mathbf{M} = M_x + iM_y$ describing the bulk magnetic moment of a macroscopic NMR sample. The phase rotations due to the gradient pulses can be described by rotations in the complex plane, $e^{-i\phi(\vec{r})}$, and thus the final vector after the above diffusion measurement will be described by

$$\mathbf{M} = \sum_{\text{spins } j} M_0 e^{-ikz_{ji}} e^{ikz_{jf}} = \sum_{\text{spins } j} M_0 e^{-ikz_j} \tag{5.8}$$

where z_j is the displacement of spin j along the gradient axis during the diffusion time, and k is the wave number of the gradient encoding. Taking each z_j to be a realization of a Gaussian probability distribution, as motivated by Equation 1.5, and

invoking the law of large numbers [185], the final magnetization is

$$
\begin{aligned}
\mathbf{M} &= \sum_i M_0 e^{ikz_i} \\
&= M_0 \int_{-\infty}^{\infty} e^{-ikz} \wp(z)dz \\
&= M_0 \int_{-\infty}^{\infty} e^{ikz} \frac{e^{-z^2/4D\Delta}}{2D\Delta\sqrt{2\pi}} dz \\
&= M_0 e^{-k^2 D\Delta}.
\end{aligned}
\tag{5.9}
$$

The result is an exponential signal attenuation linear in the diffusion time and quadratic in the helix wave number. Measuring the slope of the linear dependence between the log of the attenuation and $k^2\Delta$ provides a direct measurement of the free diffusion coefficient, D.

An alternate calculation of the macroscopic signal attenuation due to diffusion in an inhomogeneous magnetic field was proposed by Torrey, incorporating diffusion into the Bloch equations [186],

$$
\frac{\partial \vec{M}(\vec{r},t)}{\partial t} = \gamma \vec{M} \times \vec{H}(\vec{r},t) - \frac{M_x\hat{x} + M_y\hat{y}}{T_2} - \frac{(M_z - M_0)\hat{z}}{T_1} + D\nabla^2\vec{M}.
\tag{5.10}
$$

More general treatments have been developed to describe cases of non-delta function gradient pulses [184, 187] and more involved gradient pulse sequences have been developed to compensate for various experimental limitations such as gradient mismatching [188, 189] and background gradients [190, 191]. For the experiments performed here, however, the high strength and short duration of the gradient pulses relative to the diffusion time ensures the validity of the delta-pulse limit and the description of Equation 5.9.

Equations 1.4 and 5.9 define a limit on the gradient strength and relaxation times required to observe a given diffusion rate. To observe a factor of $1/e$ attenuation due to diffusion, one must satisfy

$$
\sqrt{2D\Delta} \gtrsim \frac{1}{k} = (\gamma g\delta)^{-1}
\tag{5.11}
$$

where Δ is the diffusion time, g is the gradient strength, and δ is the gradient pulse length. This requirement is equivalent to ensuring that the root mean squared diffusion length during the diffusion period is equal to the grating pitch. Equation 5.11 makes apparent the challenges in the application of gradient magnetic resonance studies to lithium. The gyromagnetic ratio of ^7Li is roughly 40% that of ^1H and ^{19}F, and the gyromagnetic ratio of ^6Li is lower than that of ^7Li by a further 40%. To enable measurements of slow diffusion, strong gradient pulses and control sequences to preserve coherence are required.

5.3 Extending Coherence Times in Solids

Strong static field gradients have been applied for measurements of transport in diffusive phases of supercooled liquids and glasses under naturally short coherence times of several hundred microseconds [40, 192]. Solids applications, where the coherence times are generally shorter and the diffusion rates generally slower will, as illustrated by Equation 5.11, require a means of preserving coherence.

The dominant source of spin-spin relaxation in many solid systems is the homonuclear dipole-dipole coupling resulting from the through space magnetic interaction of neighboring magnetic nuclei which, while averaged to zero by the random tumbling of nuclei in liquid samples, is preserved by the relative lack of motion in solid systems.

The Hamiltonian of a dipolar coupled spin system is analogous to that of a network of classically coupled magnetic dipoles

$$\hat{\mathscr{H}}_{DD} = \frac{1}{2} \sum_{j=1}^{N} \sum_{k=1}^{N} \left[\frac{\hat{\mu}_j \cdot \hat{\mu}_k}{r_{jk}^3} - \frac{3(\hat{\mu}_j \cdot \hat{r}_{jk})(\hat{\mu}_k \cdot \hat{r}_{jk})}{r_{jk}^5} \right] \tag{5.12}$$

with $\vec{r}_{jk}$ the vector between spins j and k.

In the presence of a strong external field, only those terms of Equation 5.12 which commute with the dominant Zeeman Hamiltonian are not averaged to zero and con-

tribute to the secular dipolar Hamiltonian,

$$\hat{\mathcal{H}}_{DD}^0 = \frac{\gamma^2 \hbar^2}{4} \sum_{j,k} \frac{(1 - 3\cos^2 \theta_{jk})}{r_{jk}^3} (3\hat{I}_{jz}\hat{I}_{kz} - \hat{I}_j \cdot \hat{I}_k) \qquad (5.13)$$

where θ_{jk} is the angle between $\vec{r}_{jk}$ and the orientation of the external static field. The presence of the secular dipolar Hamiltonian gives rise to a homogeneous line broadening which can be on the order of tens of kilohertz in densely packed systems of high gamma nuclei, reducing T_2's to tens of microseconds.

In the interest of obtaining high resolution solid-state spectra and pursuing NMR applications requiring long coherence times in solids, control sequences have been developed over the past several decades to refocus the influence of the dipolar Hamiltonian and remove or decrease the resulting spectral broadening.

Magic angle spinning (MAS) is one method of narrowing dipolar broadened lines by averaging the angular dependence of the dipolar Hamiltonian in coordinate space [193, 194]. By rotating the sample about an axis at 54.7° relative to the external field, the time average of the angular dependence of Equation 5.13 will approach zero provided a sufficiently fast spinning rate, exceeding the dipolar line width [195]. MAS is widely employed for spectroscopic studies of solids and MAS gradient probes have been developed for both transport and imaging studies in solids [196]. However, simultaneously satisfying the conflicting experimental requirements for both strong pulsed field gradients and high speed MAS on a single probe remains an unmet experimental challenge.

Effective averaging of the dipolar Hamiltonian is also possible through RF control of the nuclear spin ensemble. Two $\pi/2$ pulses shifted by $\pi/2$ in phase and separated by τ in time will perfectly refocus the homonuclear dipole-dipole coupling for pairs of coupled spin-1/2 nuclei generating a solid echo a time τ after the second pulse [197]. The same sequence was shown to refocus the solid-state quadrupolar coupling [198] and do so perfectly for spin-1 quadrupolar coupled nuclei [199].

It was subsequently discovered that by composing cycles of such phase shifted $\pi/2$ pulses with a particular choice of relative phase shifts and delays, one could

construct a cycle over which the average influence of the dipolar Hamiltonian, if observed periodically at the cycle time, would be zero [200, 201]. The development of the average Hamiltonian theory allowed for improved line narrowing efficiency of such sequences through the construction of super cycles introducing additional symmetries into the pulse sequence to compensate for pulse errors, phase transients, and finite pulse widths [202–205].

The use of such solid echo based refocusing sequences has been demonstrated to extend coherence times in solids for both imaging and transport applications. Pulsed field gradient imaging experiments have demonstrated resolutions of 30 μm in ferrocene and 300 μm in high density polyethylene by restricting gradient pulses to the several μs free evolution windows of the RF refocusing sequence [48]. Static field gradient studies have achieved two orders of magnitude increases in sensitivity to slow diffusion in plastic crystals through the extended gradient evolution afforded by solid echo based dipolar refocusing sequences [46].

A second family of dipolar refocusing sequences has been developed based on the building block of the magic echo pulse sequence. Similar to solid echo based sequences, the magic echo is a cycle such that over its duration the average influence of the dipolar Hamiltonian is zero [176, 206, 207]. Magic echo sequences utilize the fact that under strong, on-resonance RF irradiation, evolution under the dipole-dipole Hamiltonian, transformed into a frame doubly rotating with both the Larmor and Rabi frequencies, will propagate backward in time with a scaling factor of one half. When sandwiched by a pair of toggling frame hard pulses and free evolution periods and in the limit of infinite RF power, the result is a cycle over which the influence of the full dipole-dipole Hamiltonian is refocused perfectly [176]. A phase inversion during the RF application, similar to a rotary echo, results in no net evolution due to the applied RF field.

Magic echo sequences may be constructed in either stroboscopic or time suspension variants through the insertion of a virtual π pulse in the center of the cycle [180]. Super cycles of magic echo sequences have been developed to compensate for finite pulse widths, pulse errors and phase transients [175, 208, 209].

The advantages of magic echo based refocusing sequences in pulsed gradient experiments, where the simultaneous application of gradient fields and RF control is to be avoided, are in the long free evolution periods which may be as long as tens of ms while achieving comparable narrowing to solid echo refocusing sequences where maximum free evolution periods are on the order of tens of μs [202]. Extended free evolution periods ease requirements on the switching times required of the pulsed field gradient apparatus and allow for longer, higher current pulses into high coil constant gradient coils, ultimately allowing for the development of higher values of k and thus finer spatial resolution.

This behavior may be understood through the convergence of the Magnus expansion in the average Hamiltonian description of the two refocusing sequences [201,210]. For the magic echo, higher order terms in the Magnus expansion scale as the inverse of the B_1 field strength and so may be reduced through the application of sufficient RF power. For the solid echo, higher order terms of the Magnus expansion scale with the cycle time and so may only be suppressed by decreasing the cycle time, thereby shortening free evolution periods for gradient application. Magic echo sequences have demonstrated spatial imaging resolutions down to 50 μm in protonated solids [180,211–214], and have been successfully employed in the measurement of the rate of spin diffusion in CaF_2 [49].

5.4 The Magic Echo

Considering the case of a dipolar coupled solid under RF irradiation in a rotating frame detuned from the Larmor frequency by B_0, the system Hamiltonian is

$$\hat{\mathscr{H}} = \hat{\mathscr{H}}_Z + \hat{\mathscr{H}}_1 + \hat{\mathscr{H}}_{DD}^0 \tag{5.14}$$

where the Zeeman interaction for the residual static and applied RF fields are

$$\hat{\mathscr{H}}_Z = \gamma \hbar B_0 \sum_j \hat{I}_{zj} \tag{5.15}$$

73

and

$$\hat{\mathscr{H}}_1 = -\gamma\hbar B_1 \sum_j \hat{I}_{xj}, \qquad (5.16)$$

respectively.

Transforming into a frame rotating about the effective field, $\vec{H}_{eff} = \hat{x}B_1 + \hat{z}B_0$ and again assuming that the effective field is sufficiently large, $H_{eff} \gg H_{DD}$, such that non-commuting terms in the system Hamiltonian average to zero, the resulting Hamiltonian in the doubly rotating frame is

$$\hat{\mathscr{H}}' = -\gamma\hbar H_{eff}\hat{I}_{z'} + \frac{1}{2}(3\cos^2\theta - 1)\sum_{i>j} B_{ij}(3\hat{I}_{z'i}\hat{I}_{z'j} - \hat{I}_i \cdot \hat{I}_j) \qquad (5.17)$$

with θ the angle between the effective field and the static field, $\hat{z}'$ the unit vector in the direction of the effective field, and $B_{ij} \equiv \frac{1}{2}\frac{\gamma^2\hbar^2}{r_{ij}^3}(1 - \cos^2\theta_{ij})$.

By judicious choice of B_1 and B_0 such that $\cos^2\theta = \frac{1}{3}$, it has been shown that dipolar broadening is eliminated [215, 216]. It was subsequently discovered that by irradiating directly on-resonance, the angular dependence of Equation 5.17 becomes $\frac{1}{2}(3\cos^2\theta - 1) = -\frac{1}{2}$ and thus the resulting effective Hamiltonian in the doubly rotating frame is

$$\hat{\mathscr{H}} = -\gamma\hbar B_1\hat{I}_x - \frac{1}{2}\sum_{j>k} B_{jk}(3\hat{I}_{xj}\hat{I}_{xk} - \hat{I}_j \cdot \hat{I}_k). \qquad (5.18)$$

The first term describes the Rabi precession in the presence of the applied RF field. The second term is equivalent to a frame rotated secular dipolar Hamiltonian with amplitude scaled by a factor of negative one half. By appending a pair of frame transformation pulses outside the period of RF irradiation, the evolution due to the second term is equivalent to that of evolving the secular dipolar Hamiltonian backwards in time at half speed. Rabi precession due to the first term may be removed by implementing a phase inversion halfway through the RF irradiation period, implementing a rotary echo [217].

With only on-resonance RF irradiation of sufficient strength, dipolar echoes can

be obtained on time scales far beyond those of the solid echo. Furthermore, the sequence is easily modified to include refocusing of chemical shifts. By rotating the second frame transformation pulse, equivalent to the insertion of a virtual π pulse at the center of the RF period, a time suspension variant is achieved.

Stroboscopic line narrowing sequences were subsequently derived [175] and due to their amenability to long gradient pulses, solid-state imaging applications were developed [39,180]. The average Hamiltonian theory [200,202,210,218] describes a means of improving the efficiency of line narrowing sequences through the construction of supercycles to compensate for pulse and phase errors and finite pulse widths and further symmetrizing the toggling frame Hamiltonian. By doing so, supercycles of the magic echo sequence have demonstrated improved line narrowing both when refocusing only the dipolar interaction and when refocusing both the dipolar interaction and chemical shift [209].

5.5 Stimulated Echo Dynamics under Diffusion and Exchange

In a stimulated echo diffusion measurement, it is desirable for the diffusion time to approach T_1 so as to increase the diffusive path length and thus maximize diffusive attenuation. On this time scale, there will be, in general, more than one process leading to the attenuation of the simulated echo amplitude. In order to isolate attenuation due to diffusion, an accurate understanding of the competing sources of signal attenuation during the diffusion time is required. For the case of Li_2S, the exchange dynamics identified in Chapter 4 introduce effective relaxation pathways as magnetization from the bath under observation migrates to the alternate bath.

Furthermore, as demonstrated in Chapter 4, the mixing introduced by an exchange processes can generate macroscopic dynamics described not by the intrinsic properties of either bath, but by an occupancy time-weighted average over the properties of the sites involved in the exchanged process. Care must be taken in choosing initial

conditions and measurements so as to isolate the intrinsic transport properties of each bath where possible and to understand and correctly model the influence of exchange where not.

To model the stimulated echo experiment in the presence of an exchange process, we reconsider the microscopic description of spin transport in a gradient field given in Equation 5.9 now including exchange. An exchange process introduces an incoherent, stochastic switching of the spin and transport evolution parameters between those of the exchanging baths. The observed spin and transport dynamics of a given spin will be determined by the history of site occupations and durations.

We model the residency of an exchanging single spin as a two state Markov chain. Each state corresponds to occupancy in a given bath and imposes spin and transport evolution governed by the intrinsic properties of that bath for the duration of the residency. Exchange is modeled by a Poisson point process with jump rates corresponding to the exchange rates determined in Chapter 4.

We now follow the evolution of a single spin which, after the encoding period, is found to be in state one of a two bath exchange process. The analysis is simplified by the description as a Markov process and that both the relaxation and diffusion processes are both additive and jointly commutative. We need only determine the total occupancy time on each site during the given diffusion period to completely describe both spin and transport dynamics.

If the diffusion time is fixed to Δ, and we denote the total residency time on site i during Δ as Δ_i, the net stimulated echo attenuation, including relaxation and

diffusion, will be

$$
\begin{aligned}
\mathbf{M} &= \sum_{\text{spins } j} M_0 e^{-\frac{\Delta_{1i}}{T_{11}}} e^{-\frac{\Delta_{2i}}{T_{12}}} e^{-ikz_i} \\
&= \sum_{\text{spins } j} M_0 e^{-\frac{\Delta_{1i}}{T_{11}}} e^{-\frac{\Delta_{2i}}{T_{12}}} e^{-ik(z_{1i}+z_{2i})} \\
&= \int_0^\Delta d\Delta_1 \wp(\Delta_1) e^{-\frac{\Delta_1}{T_{11}}} e^{-\frac{(\Delta-\Delta_1)}{T_{12}}} \iint_{-\infty}^\infty dz_1 dz_2 \wp(z_1)\wp(z_2) e^{-ik(z_1+z_2)} \\
&= \int_0^\Delta d\Delta_1 \wp(\Delta_1) e^{-\frac{\Delta_1}{T_{11}}} e^{-\frac{(\Delta-\Delta_1)}{T_{12}}} \\
&\qquad \iint_{-\infty}^\infty dz_1 dz_2 e^{-ik(z_1+z_2)} \frac{e^{-z_1^2/4D_1\Delta_1}}{\sqrt{4\pi D_1\Delta_1}} \frac{e^{-z_2^2/4D_2(\Delta-\Delta_1)}}{\sqrt{4\pi D_2(\Delta-\Delta_1)}} \\
&= \int_0^\Delta d\Delta_1 \wp(\Delta_1) e^{-\frac{\Delta_1}{T_{11}}} e^{-\frac{(\Delta-\Delta_1)}{T_{12}}} e^{-k^2 D_1\Delta_1} e^{-k^2 D_2(\Delta-\Delta_1)}
\end{aligned}
\tag{5.19}
$$

where we have recast the attenuation in terms of a single random variable, the total occupancy time on site one, Δ_1. Calculating $\wp(\Delta_1)$ at long times is straightforward as given by principle of detailed balance. However, the diffusion times considered here will be on the order of the inverse of the exchange rate and thus calculation of the probability density function $\wp(\Delta_1)$ in the short term transient response regime is required.

5.5.1 Calculation of the Residency Time Probability Density Function for a Two-Site Exchange Model

The analysis of the diffusion measurements presented in Chapter 5 is complicated beyond that of the standard stimulated echo experiment due to the presence of an exchange process. Random hopping between magnetically and kinetically inequivalent sites generates a stochastic time dependence in the set of parameters which govern both spin and transport evolution. To infer the intrinsic site characteristics from the observed ensemble evolution, a quantitative model of the exchange process, its influence on spin and transport dynamics and the resulting response as observed

77

through the ensemble NMR signal is required.

Here, we model the evolution of a single spin system undergoing chemical exchange as a series of sequential periods of free spin and transport evolution, individually absent exchange, with evolution parameters jumping instantaneously at the boundary of each period to reflect the current site of the exchanging spin. The exchange process determines the duration of each evolution period and, for cases of more than two exchanging sites, the next site to be occupied. While the stochastic nature of the exchange process will make the evolution of each individual spin unpredictable, averaging across a large ensemble of independently evolving spins, as required to determine the observable NMR response of the macroscopic spin system, will yield a deterministic quantity.

As the net evolution of a single exchanging spin is determined by the composition of the evolutions from each period between site hops, a restriction to classical spin and transport evolution is justified. As discussed in Chapter 4, spins begin the diffusion period in an eigenstate of both the Zeeman and secular dipolar Hamiltonians. Thus, two-spin interactions requiring a quantum description will not drive evolution during the diffusion period. Likewise, the diffusion and exchange processes we consider are modeled by independent classical random walks [23] and Markov random processes under the sudden jump approximation [152, 153, 219].

Another simplification, which follows from the classical description of both displacement and magnetization, is that for those quantities for which the order of the composition of evolutions does not impact the net result or equivalently, that evolutions under alternate exchanging sites commute, the net evolution will be dependent only on the total occupancy time on each site, independent of the number or duration of exchange periods. Thus, to calculate an ensemble measure of an arbitrary function of the total occupancy time, such as the net relaxation or root mean square displacement due to diffusion, the residency time probability density function is sufficient.

To describe the occupancy time probability density function (PDF), we consider a random variable T with realizations τ describing the total duration of time a spin resides on its initial site, including time after even numbered jumps, during an evolu-

tion of fixed time Δ. We begin by calculating the cumulative density function (CDF) which is simply related to the PDF by differentiation with respect to the realization value

$$f_X(x) = \frac{\partial}{\partial x} F_X(x) \tag{5.20}$$

where we denote the PDF of a random variable X as $f_X(x)$, defined by

$$\wp(a \leq X \leq b) = \int_a^b f_x(x) dx \tag{5.21}$$

and the CDF $F_X(x)$

$$F_X(x) = \wp(X \leq x) \tag{5.22}$$

[185].

The total probability theorem allows the probability of a given residency time to be decomposed into paths enumerated by the number of jumps as

$$F_T(\tau) = \wp(T < \tau) = \sum_{n=0}^{\infty} \wp(T < \tau \cap n \text{ jumps }). \tag{5.23}$$

The individual addends on the right hand side can be derived from the product of the probabilities of n single jump events from the definition of the Poissonian jump process and a Heaviside step function to enact the $T < \tau$ condition. The result is the time ordered integral

$$\wp(T < \tau \cap n \text{ jumps }) = \underbrace{\int_0^{\Delta} dt' \int_0^{t'} dt'' \ldots \int_0^{t'^{n-1}} dt'^n}_{n \text{ integrals}} E_n K_n H_n \tag{5.24}$$

where E_n is a product of $n+1$ decaying exponentials

$$E_n = \begin{cases} e^{-k_{21}(\Delta-t')} e^{-k_{12}(t'-t'')} \ldots e^{-k_{12}t'^n} & \text{if } n \text{ odd} \\ e^{-k_{12}(\Delta-t')} e^{-k_{21}(t'-t'')} \ldots e^{-k_{12}t'^n} & \text{if } n \text{ even} \end{cases}, \tag{5.25}$$

79
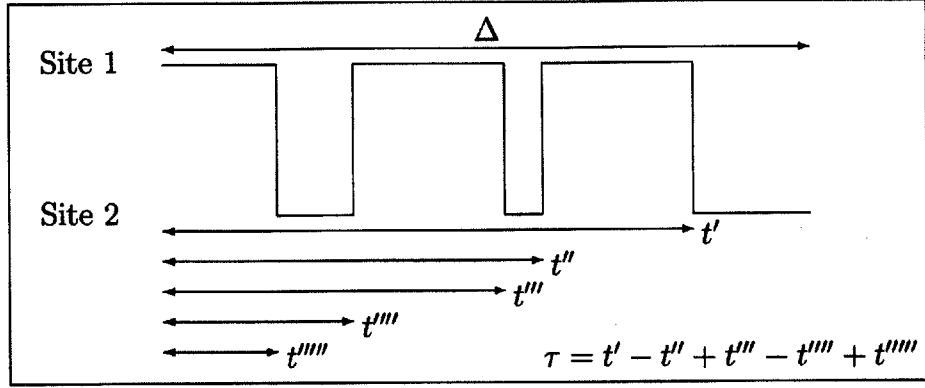
Figure 5-1: A diagrammatic reference of the variables used in the calculation of the total residency time of a two site hopping model. In this case, a path consisting of five jumps is considered, and the value τ is equal to the sum of the durations spent occupying the first site.

K_n is a product of the rate constants

$$K_n = \begin{cases} k_{12} \left(k_{12} k_{21} \right)^{(n-1)/2} & \text{if } n \text{ odd} \\ \left(k_{12} k_{21} \right)^{n/2} & \text{if } n \text{ even} \end{cases}, \tag{5.26}$$

and H_n is the Heaviside step function

$$H_n = H(\tau - T) = H\left(\tau - \sum_{\substack{n \text{ on} \\ \text{site 1}}} t_n \right) = \begin{cases} H(\tau - (t' - t'' + t''' - t'''' + \ldots)) & \text{if } n \text{ odd} \\ H(\tau - (\Delta - t' + t'' - t''' + \ldots)) & \text{if } n \text{ even} \end{cases}. \tag{5.27}$$

The above integrals are simple to solve in low dimensions ($n \leq 3$) where the influence of the step function to replace the bounds of integration can be simply identified geometrically. In higher dimensions, however, the area over which the integral is to be taken must be expressed as the area of an n-dimensional prism cut by an $n - 1$ dimensional hyperplane and arriving at simple forms for the integration bounds is complicated substantially.

At this point, it is convenient to reintroduce the derivative with respect to τ of Equation 5.20. As τ is present only as an argument to the step function, the derivative with respect to τ replaces the step with a delta function of the same argument.

80

Integrating over the delta function removes a single integral and greatly simplifies the bounds calculations on those remaining,

$$f_T(\tau \cap n) = e^{-k_{12}\tau} e^{-k_{21}(\Delta-\tau)}$$

$$\times \begin{cases} k_{12} (k_{12}k_{21})^{(n-1)/2} \underbrace{\int_0^{\Delta-\tau} dt' \int_0^{t'} dt''' \ldots}_{(n-1)/2 \text{ integrals}} \underbrace{\int_0^{\tau} dt'' \int_0^{t''} dt'''' \ldots}_{(n-1)/2 \text{ integrals}} \text{ if } n \text{ odd} \\ (k_{12}k_{21})^{n/2} \underbrace{\int_0^{\tau} dt' \int_0^{t'} dt''' \ldots}_{n/2 \text{ integrals}} \underbrace{\int_0^{\Delta-\tau} dt'' \int_0^{t''} dt'''' \ldots}_{n/2-1 \text{ integrals}} \text{ if } n \text{ even} \end{cases}$$

(5.28)

Making use of the identity

$$\underbrace{\int_0^x dt' \int_0^{t'} dt'' \ldots}_{n \text{ integrals}} = \frac{x^n}{n!}$$

(5.29)

simplifies Equation 5.28 to

$$f_T(\tau \cap n) = e^{-k_{12}\tau} e^{-k_{21}(\Delta-\tau)}$$

$$\times \begin{cases} k_{12} (k_{12}k_{21})^{(n-1)/2} \frac{(\tau(\Delta-\tau))^{(n-1)/2}}{(\frac{n-1}{2})!(\frac{n-1}{2})!} \text{ if } n \text{ odd} \\ (k_{12}k_{21})^{n/2} \frac{\tau^{n/2}(\Delta-\tau)^{n/2-1}}{(\frac{n}{2})!(\frac{n}{2}-1)!} \text{ if } n \text{ even} \end{cases}$$

(5.30)

Substituting Equation 5.30 back in to equations 5.20 and 5.23 yields an expression for the PDF of the total residency time

$$f_T(\tau) = e^{-k_{12}\Delta}\delta(\Delta - \tau)$$

$$+ e^{-k_{12}\tau} e^{-k_{21}(\Delta-\tau)}$$

$$\times \left[\sum_{\substack{n=1 \\ \text{odd}}}^{\infty} k_{12}(k_{12}k_{21})^{(n-1)/2} \frac{(\tau(\Delta - \tau))^{(n-1)/2}}{\frac{n-1}{2}!\frac{n-1}{2}!} \right.$$

(5.31)

$$\left. + \sum_{\substack{n=2 \\ \text{even}}}^{\infty} (k_{12}k_{21})^{n/2} \frac{\tau^{n/2}(\Delta - \tau)^{n/2-1}}{\frac{n}{2}!(\frac{n}{2} - 1)!} \right].$$

These summations are greatly simplified by recalling the series expansion form of the modified Bessel functions of the first kind [220, 221]

$$I_\nu(z) = \left(\frac{z}{2}\right)^\nu \sum_{k=0}^{\infty} \frac{(z/2)^{2k}}{k!\Gamma(\nu + k + 1)} \tag{5.32}$$

and, specifically the zeroth and first order,

$$I_0(z) = \sum_{k=0}^{\infty} \frac{(z/2)^{2k}}{k!k!} \tag{5.33}$$

$$I_1(z) = \frac{z}{2} \sum_{k=0} \frac{(z/2)^{2k}}{k!(k+1)!}. \tag{5.34}$$

As a result, Equation 5.31 can be expressed more compactly as

$$f_T(\tau) = e^{-k_{12}\Delta}\delta(\Delta - \tau) + e^{-k_{12}\tau}e^{-k_{21}(\Delta-\tau)} \left[k_{12}I_0(2\eta) + \frac{\eta}{(\Delta - \tau)}I_1(2\eta) \right] \tag{5.35}$$

with

$$\eta \equiv \sqrt{k_{12}k_{21}\tau(\Delta - \tau)}. \tag{5.36}$$

5.5.2   Functions of the Occupancy Time Random Variable

Equation 5.35 describes the likelihood of the total duration of time an exchanging spin will occupy its initial site during a fixed evolution time. This expression allows for the calculation of the ensemble quantities which, at the microscopic scale, are functions of the total residency time and are required in order to calculate the ensemble NMR response in gradient and relaxation experiments.

The observed NMR signal can be calculated as the coherent sum of the individual nuclear magnetizations over the order of 10^{23} spins comprising an NMR sample. It is in this way that microscopic quantities are observed as their ensemble averages in the detected signal. For microscopic quantities determined by stochastic processes, the signal contribution must be calculated explicitly as the number of realizations tends to infinity which will, by the law of large numbers, be determined by the expectation

value of the random variable. To calculate the expectation value of a simple function of a stochastic variable, one need only integrate the value of the function across the PDF of the random variable

$$E[g(X)] = \int_{-\infty}^{\infty} g(x) f_X(x) dx. \tag{5.37}$$

Quantities such as the root mean square displacement which are not simple functions of the residency time but are themselves stochastic processes for which the residency time is a parameter will require the calculation of the resulting joint PDF.

Reconstruction of Relaxation Curves Under Exchange

To calculate the net effective relaxation of a spin ensemble exchanging between site one, on which it undergoes spin-lattice relaxation with a time constant T_{11}, and site two, with T_{12}, we solve for the expectation value of a random variable describing the net relaxation across both sites. Relaxation on both sites is a multiplicative exponential relaxation independent of the input state and so the total impact of relaxation across both sites is described by the random variable $R = e^{-\tau_1/T_{11}} e^{-\tau_2/T_{12}} = e^{-\tau_1/T_{11}} e^{-(\Delta-\tau_1)/T_{12}}$ which is itself fully determined by the residency time on the initial site, τ_1, hereafter referred to as τ. Expressed in terms of τ, the expectation value of R then is

$$E[R] = \int_0^{\Delta} d\tau e^{-\tau/T_{11}} e^{-(\Delta-\tau)/T_{12}} f_T(\tau). \tag{5.38}$$

To reproduce the results of Equation 4.8, we consider the relaxation of two exchanging baths and identify the final magnetization at each site as the sum of the magnetization corresponding to the even n-jump terms from the bath we observe, and the odd n-jump terms originating from the alternate bath.

$$E[M_1(t)] = E[M_1(t| \text{ originated in Bath 1 })] + E[M_1(t| \text{ originated in Bath 2 })]$$

$$= \int m\wp(m| \text{ Bath 1 } \cap \text{ even } n \text{ jumps })dm + \int m\wp(m| \text{ Bath 2 } \cap \text{ odd } n \text{ jumps })dm$$

$$= \int_0^\Delta d\tau M_{10}(1 + M_{1i}e^{-\tau/T_{11}}e^{-(\Delta-\tau)/T_{12}})\wp(\tau| \text{ Bath 1 } \cap \text{ even } n \text{ jumps })$$

$$+ \int_0^\Delta d\tau M_{20}(1 + M_{2i}e^{-\tau/T_{12}}e^{-(\Delta-\tau)/T_{11}})\wp(\tau| \text{ Bath 2 } \cap \text{ odd } n \text{ jumps })$$

$$= \int_0^\Delta d\tau M_{10}(1 + M_{1i}e^{-\tau/T_{11}}e^{-(\Delta-\tau)/T_{12}}) \left(e^{-k_{12}\Delta}\delta(\Delta - \tau) + e^{-k_{12}\tau}e^{-k_{21}(\Delta-\tau)}\frac{\eta}{\Delta - \tau}I_1(2\eta) \right)$$

$$+ \int_0^\Delta d\tau M_{20}(1 + M_{2i}e^{-\tau/T_{12}}e^{-(\Delta-\tau)/T_{11}}) \left(e^{-k_{21}\tau}e^{-k_{12}(\Delta-\tau)}k_{21}I_0(2\eta) \right)$$

$$\tag{5.39}$$

where the equilibrium magnetization, representative of the relative bath sizes, is denoted by M_{n0} and the initial magnetization, ranging from 0 to -2 for aligned and anti-aligned initial states as $-2\sin(2\theta)$ with flip angle θ is denoted by M_{ni}.

Calculation of the Intrinsic Diffusion Coefficient from Apparent Diffusion Coefficient

We would similarly like to utilize this derived PDF to determine the form of the ensemble average diffusive displacement from the intrinsic diffusion coefficients and exchange rates. Unlike the case above where relaxation is a simple exponential function of the occupancy time random variable τ, diffusion is itself a random process for which the initial-site occupancy time random variable τ is a parameter. Moreover, the net displacement due to diffusion will be the sum of two random diffusion processes, one with diffusion coefficient D_1 and diffusion time τ and another with D_2 and time $\Delta - \tau$. In this case, as both random diffusion processes are assumed to be zero-mean Gaussian random variables, the PDF of the displacement due to the sum of these two processes can be shown to also be a zero-mean Gaussian random variable with variance $\sigma^2 = \sigma_1^2 + \sigma_2^2 = 2D_1\tau + 2D_2(\Delta - \tau)$.

This allows for the construction of the displacement probability density function

for a spin originating on site one

$$
\begin{aligned}
f_Z(z) &= \int_0^\Delta d\tau \wp(Z = z \cap T = \tau) \\
&= \int_0^\Delta d\tau \wp(Z = z | T = \tau) \wp(T = \tau) \\
&= \int_0^\Delta d\tau \frac{e^{-z^2/(4D_1\tau + 4D_2(\Delta - \tau))}}{\sqrt{4\pi(D_1\tau + D_2(\Delta - \tau))}} f_T(\tau).
\end{aligned}
\tag{5.40}
$$

Calculation of the Net Stimulated Echo Attenuation Under Diffusion and Exchange

Having established the above, it is now possible to derive an expression describing the total attenuation of the stimulated echo including exchange and the independent relaxation and transport properties of each bath. Analysis of experimental data, in light of this model and the exchange and relaxation parameters established in Chapter 4, will allow the determination of site specific transport properties.

In deriving the expression for the net echo attenuation, we assume that only spins which originate on a given site will contribute to the site's final signal amplitude. For spins originating on the broad bath and exchanging to the narrow, this is justified by the requirement that magnetization persist through both the encoding and decoding gradient to contribute to the final echo. For spins originating in the narrow bath and exchanging to the broad, this is justified by the relative sizes of the two baths and the relatively rapid spin-lattice relaxation of the narrow bath. Substituting the initial site occupancy probability density function, Equation 5.35, into the equation for the net stimulated echo amplitude, Equation 5.19, yields an expression for the net echo attenuation under exchange and diffusion

$$
\begin{aligned}
\mathbf{M} = \int_0^\Delta d\tau\, e^{-\frac{\tau}{T_{11}}} e^{-\frac{(\Delta-\tau)}{T_{12}}} e^{-k^2 D_1 \tau} e^{-k^2 D_2(\Delta-\tau)} \\
\left(e^{-k_{12}\Delta} \delta(\Delta - \tau) + e^{-k_{12}\tau} e^{-k_{21}(\Delta-\tau)} \frac{\eta}{\Delta - \tau} I_1(2\eta) \right).
\end{aligned}
\tag{5.41}
$$

This expression provides a model against which data in the following chapter can

be compared to obtain the intrinsic diffusion properties of each bath from the total attenuation of the narrow and broad line stimulated echo amplitudes.

Chapter 6

Experimental Procedure and Results

As an experimental apparatus providing the high gradient field strengths and rapid switching times required for the diffusion measurements to be preformed here is not available commercially, a custom probehead and gradient coil are required. This chapter describes the design, construction and application of such an apparatus for the stimulated echo measurements of lithium diffusion in Li_2S.

Pulsed field gradient stimulated echo experiments were performed in a 7.05 T superconducting magnet using a Bruker Avance 300 MHz spectrometer and a custom-built, single axis gradient probe. The probehead design and gradient support have been described previously [222]. The design and construction of the pulsed field gradient coil is described in Section 6.2 below. Powdered samples of Li_2S were sealed in 1 mm OD glass capillaries under an inert argon atmosphere and confined to a 1 mm axial region by Teflon rod inserts. An eight turn, 36 AWG RF coil was used with an axially varying winding geometry to improve B_1 homogeneity [223] and fit tightly within the 1.4 mm sample space of the gradient coil.

In addition to providing the RF excitation, control and detection, the spectrometer was used to send gating pulses to a switched circuit driving the gradient coil, as described in the next section.
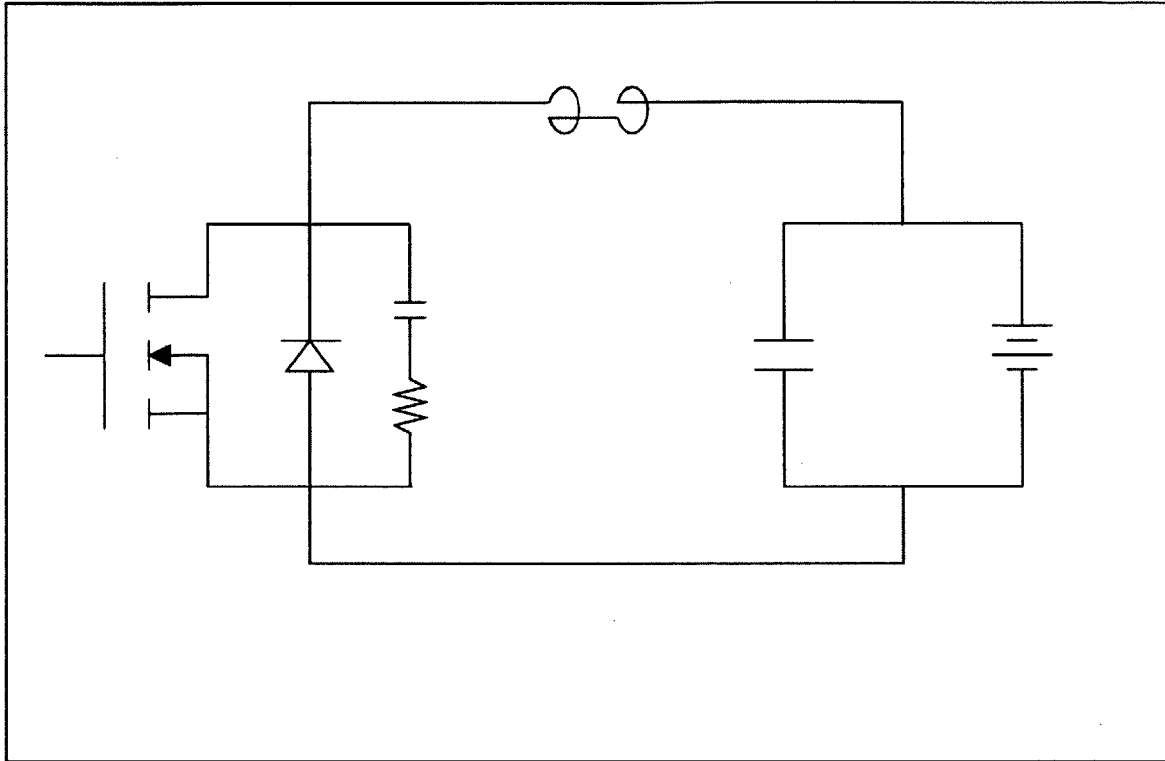
Figure 6-1: A schematic of the pulsed DC circuit employed for the application of trains of high-current gradient pulses, each up to several hundred μs in length. An isolated TTL trigger from the spectrometer gated the Behlke HTS 32-12-B MOSFET switch. The circuit drove a 263 $m\Omega$, 10.8 μH gradient coil using a single 12 V lead-acid battery achieving peak currents of 15.7 A. An RC snubber was placed across the MOSFET switch to match the critical damping condition and aid in quickly de-energizing the gradient coil.

6.1 Circuit for Strong Pulsed Field Gradients

The delivery of short, intense gradient pulses was accomplished via the switched DC circuit diagrammed in Figure 6-1. This design is derived from earlier solid-state NMR studies utilizing high-current pulsed gradient coils [47, 49] and has been modified to match the RF refocusing sequence, switching element and gradient coil used in this study.

A single Behlke HTS 32-12-B MOSFET switch was chosen as the switching element in this circuit for its order of tens of nanoseconds switching times, reliable operation, high sustained pulse current and robustness to transient and flyback voltage spikes. The cost for this reliability, however, is a relatively large closed switch

resistance measured at 430 $m\Omega$ by way of a four point measurement. The choice of a high resistance switching element limits high-current, low-voltage operation and so influences coil design towards higher coil constant and higher impedance designs.

As efficient refocusing of the Li_2S ^7Li resonance is achieved with the spectroscopic variants of the magic echo dipolar refocusing sequence, a single polarity pulsed circuit is chosen. As described in Section 6.4, the weak heteronuclear dipolar interactions of Li_2S, left unrefocused, do not generate large cross terms in the refocusing of the dominant dipolar relaxation mechanism and are refocused by the stimulated echo sequence. Thus, a spectroscopic variant of the magic echo is sufficient for coherence preservation. Unlike the time-suspension variants of the magic echo sequence, spectroscopic variants preserve the sign of the toggling frame Zeeman Hamiltonian in each free evolution window and so gradient pulses of a single polarity may be applied constructively in every window. Compared to the bi-directional pulse circuits employed in cases of time-suspension refocusing sequences, single polarity pulse circuit designs benefit from reduced complexity and reduced in-line resistance.

The pulse circuit was driven by a single 12 V lead-acid battery. To assist in quickly de-energizing the coil without large flyback voltages, a matching RC snubber was added across the switch to critically damp the coil discharge current [224]. Gradient currents were measured with a Tektronix TCP305 inductive current probe and TCPA300 amplifier. Current traces were digitized and recorded on a Tektronix DPO4104 oscilloscope. The integrated areas of the current pulses were recorded and used to determine the achieved value of k.

6.2 Design and Construction of a Strong Pulsed Field Gradient

In order to be sensitive to the slow diffusion rates expected of room-temperature ionic diffusion in solids, gradient strengths in excess of 100 T/m are required. To achieve these large gradient strengths at modest currents, a Maxwell pair configuration with

millimeter scale geometry is required and coil design is restricted considerably [49].

The coil design described here opted for a larger impedance, higher coil constant and lower operating current than earlier designs [49, 177] influenced by the choice of the high internal resistance switching element of the driving DC pulse circuit. Low current designs benefit from reductions in difficulties such as Ohmic heating and Lorentz forces compared to high-current gradient probes.

For a static current, I, of a given geometry, the resulting magnetic field is determined by the Biot-Savart Law

$$\vec{B}(\vec{r}) = \frac{\mu}{4\pi} \oint_C \frac{Id\vec{\ell} \times \vec{r}}{|\vec{r}|^3}. \tag{6.1}$$

where $d\ell$ is the differential line element along the current path, C, and μ is the permeability of the sample. Considerable literature exists examining potential coil geometries, the intensity and homogeneity of the resulting gradient fields and their relative merits on metrics such as gradient strength, uniformity, heating, efficiency and applicability for magnetic resonance imaging and transport applications [225–227].

The Maxwell pair is favored in solid-state diffusion studies for its high coil constants and ease of construction on small length scales. This geometry creates a field gradient by arranging two uniaxial current hoops of shared diameter D with oppositely oriented current flow, centered at $\pm z_0$ along the center axis. The generated magnetic field is zero at the center of the two hoops and the resulting field gradient is

$$g = \frac{12\beta\mu I}{(1 + \beta^2)^{5/2} D^2} \tag{6.2}$$

with $\beta \equiv 2z_0/D$. Arranging the separation of the hoops such that $\beta = \sqrt{3}/2$ results in an approximately linear gradient field for which the third and all even order terms in the expansion about the origin are zero. Configurations involving additional pairs of oppositely oriented current rings have been developed to generate gradient fields of improved linearity for which increasing odd expansion orders are zero [225].

From Equation 5.11, the measured values of the relaxation rates and expected ranges of the diffusion coefficient, a coil design on the order of 10 $T/m/A$ was required.

90

A numerical optimization was performed to identify a set of suitable coil parameters to generate the required gradient field. The coil resistance was fixed at approximately 300 $m\Omega$ to maximize the product of the current and gradient strength, given the parameters of the pulse circuit described in Section 6.1. Field profiles were calculated for a selection of multiple-turn first order Maxwell pair geometries with varying coil diameter, separation, wire gauge, and winding cross section to identify the parameters which maximized the resulting field gradient while maintaining less than 5% variation in gradient strength across the 1 mm diameter, 1 mm length sample space. The chosen geometry is shown in Figure 6-2.

The result is a geometry which closely matches the Maxwell pair condition for the average wire placement, weighted by the $1/r^3$ fall off for windings further from the sample. The gradient form is 8 mm in diameter and 14.1 mm in length. Two 1.3 mm wide channels are cut down to a diameter of 1.6 mm, separated by 1.5 mm. A 1.4 mm diameter sample hole is cut through the center of the gradient form to support a 1.0 mm OD sample tube wrapped with 36 AWG wire. The gradient coil was wound with 30 turns of 30 AWG insulated copper wire with a cross section roughly five layers parallel to the coil axis by six layers perpendicular to it.

The form was machined from a rod of Vespel SP-1, chosen for its high strength and favorable machining properties. To mount the set to the probe head, a pair of machined copper plates were employed both as leads carrying the gradient current and clamps supporting the gradient set as described in [222].

The coil constant was calibrated against the known diffusion coefficient of water at $25°C$ [228] to be 7.79 ± 0.152 $T/m/A$. Driven by a 12 V DC source, the gradient circuit achieved gradients of 122 T/m at a peak current of 15.7 A.

6.3 Li_2S Narrow Line Diffusion Measurement

To isolate and measure the presence of potential diffusion processes in the narrow line, a standard stimulated echo experiment was performed without dipolar refocusing as diagrammed in Figure 6-4. By virtue of the narrow line's long T_2's, sufficiently long
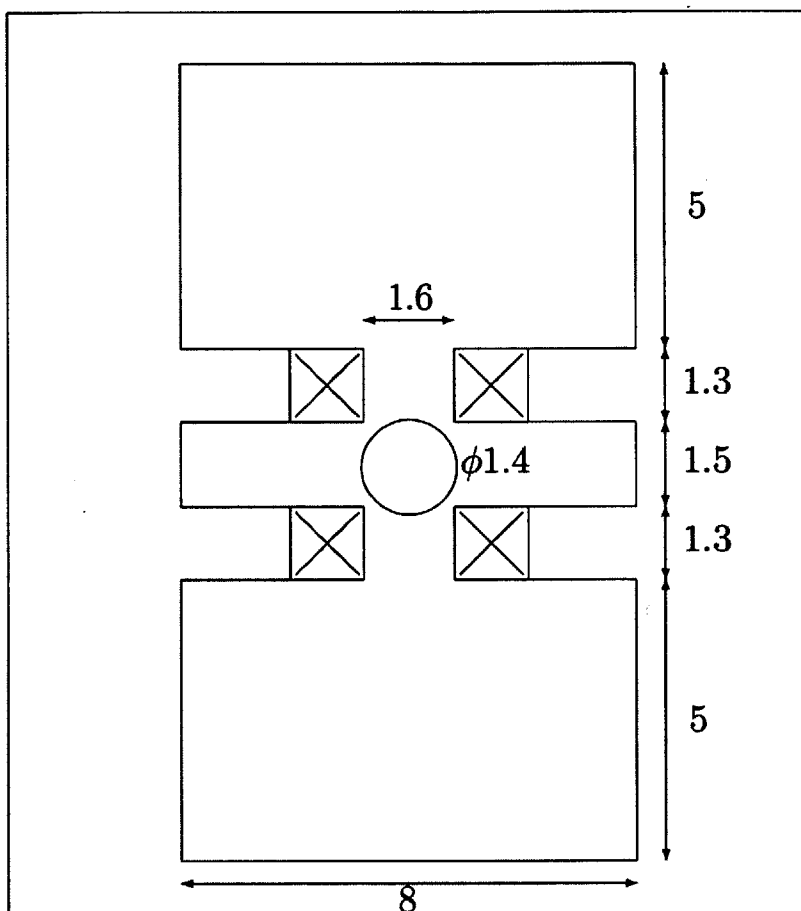
Figure 6-2: A drawing of the pulsed field gradient coil geometry constructed for this study. The coil parameters were determined by numerical optimization over the gradient field strength and uniformity. The resulting coil design was wound with 30 turns of 30 AWG copper wire and produced a measured coil constant of $7.79 \pm 0.152 \ T/m/A$.
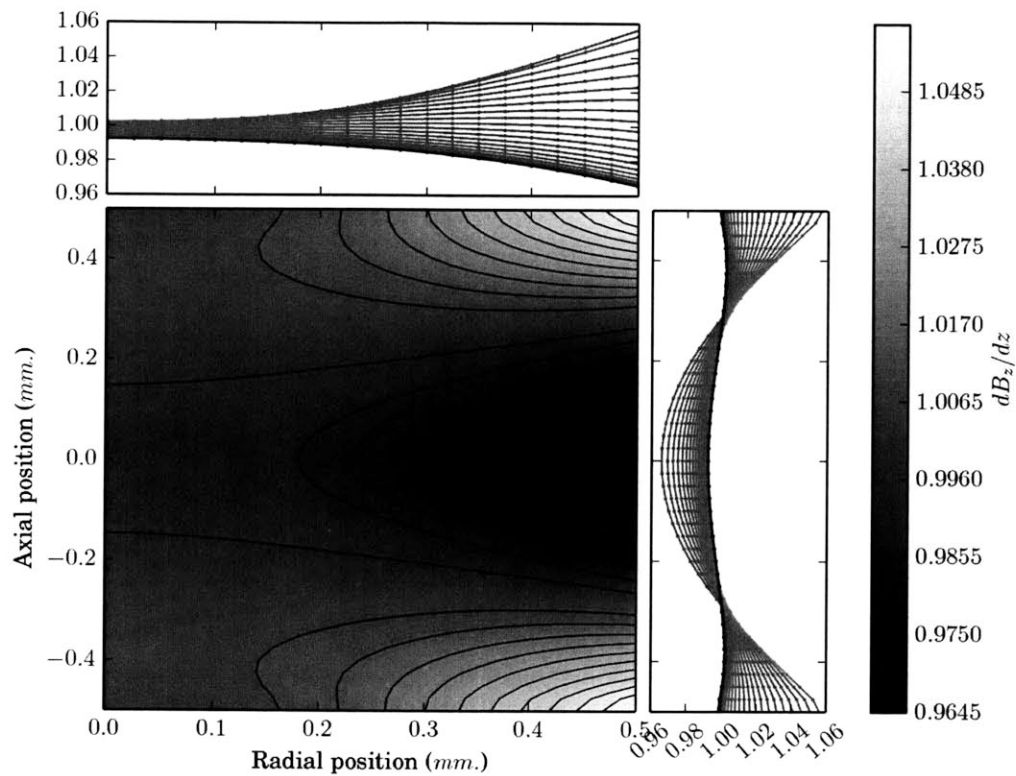
Figure 6-3: A plot of the calculated magnetic field gradient distribution across the sample space as generated by the coil described in Figure 6-2. Contours are normalized to the average gradient field strength and denote each 0.5% deviation. The adjacent plots display the gradient field strength along cross sections of fixed radial or axial position with the darkest line highlighting the centermost cross sections.

gradient pulses are achieved without the application of refocusing sequences. This simultaneously saturates the broad line before the beginning of the diffusion period and simplifies the analysis of the exchange. Spins originating in the broad line will quickly decohere and will not contribute to the detected narrow line signal. According to the exchange model described and parameterized in Chapter 4, two jump processes which involve spins originating in the narrow bath, exchanging to the broad bath, and exchanging back to the narrow bath within the diffusion period may be neglected due to the T_1^N limited diffusion time and the relative sizes of the narrow and broad bath. Thus, any diffusive attenuation observed in the stimulated echo of the narrow line may be attributed solely to the transport properties of the narrow bath.

We acquired stimulated echo spectra, with and without gradient pulses, with a fixed encoding time of 500 μs, gradient pulse lengths varied between 50 μs and 300 μs and diffusion time incremented between 5 ms and 40 ms for each value of the gradient pulse length.

As the exchange dynamics will not introduce mixing between the narrow and broad bath transport properties, the narrow line stimulated echo magnitudes are amenable to a plot of the log attenuation against $k^2\Delta$, normalized by trials without gradient pulses to remove the influence of relaxation, as motivated by Equation 5.9. The result is shown in Figure 6-5. The measured narrow line diffusion coefficient is $2.39 \pm 0.34 \cdot 10^{-8}$ cm^2/s.

6.4 Li_2S Broad Line Diffusion Measurement

To identify the presence of any diffusion processes in the broad line, a modified version of the pulsed gradient stimulated echo sequence was applied, as illustrated in Figure 6-6. Unlike the case of the narrow line, where the influence of exchange on the apparent transport properties was negligible, it is expected that exchange will have an influence on the apparent transport of the broad line. Processes involving spins originating on the broad bath and exchanging to the narrow bath multiple times during the long diffusion period cannot be neglected. The model described in Section 5.5, informed by

RF $\frac{\pi}{2})$ $\frac{\pi}{2})$ $\frac{\pi}{2}$

τ Δ

G
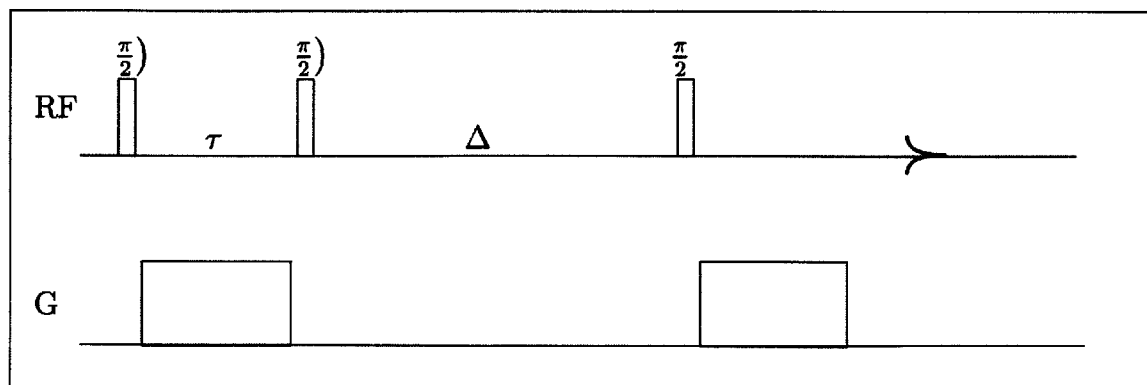
Figure 6-4: The pulse sequence utilized for the narrow line pulsed gradient stimulated echo experiment. A standard stimulated echo sequence saturates the broad line and removes its influence from the observed transport dynamics. The encoding time was fixed to 500 μs, the gradient pulse length was varied between 50 μs and 300 μs, and the diffusion period was varied between 5 ms and 40 ms as limited by the short lifetime of spins in the narrow bath.

the exchange and relaxation rates determined in Chapter 4, allow us to infer intrinsic site transport properties from the observed narrow and broad line stimulated echo attenuation.

To address the naturally short coherence times of the broad line, a spectroscopic TREV4 dipolar refocusing sequence [209] was incorporated into the encoding and decoding periods of the stimulated echo experiments. The choice to use a stroboscopic rather than time-suspension refocusing sequence was allowed by the weak heteronuclear dipolar coupling such that efficient refocusing of the dominant homonuclear dipolar relaxation mechanism was achieved without the need of refocusing the heteronuclear or chemical shift terms each cycle. Two values of τ in the TREV sequence were utilized, 50 μs and 75 μs, and the base TREV cycle was repeated up to four times. Broad line stimulated echo amplitudes were acquired for each set of encoding parameters both with and without gradient pulses with diffusion times incremented between 0.5 s and 12 s.

As for the narrow line, a plot of the broad line stimulated echo amplitude as a function of $k^2\Delta$ with attenuation due to relaxation removed is shown in Figure 6-7. We observe no diffusive attenuation for the broad line and so no measurement of the broad line diffusion coefficient can be made. However, an upper bound on the

Figure 6-5: A plot of the log narrow line stimulated echo attenuation as a function of $k^2 \Delta$, motivated by Equation 5.9. Signal attenuation due to relaxation and exchange has been removed through a renormalization of echo amplitudes against those acquired in the absence of gradient pulses and the parameterized model of Chapter 4. The linearity of the plotted line and the agreement between data acquired for varying values of k support a single bath Gaussian diffusion process, shown as a solid line, with a diffusion coefficient determined to be $2.39 \pm 0.34 \cdot 10^{-8}$ cm^2/s.
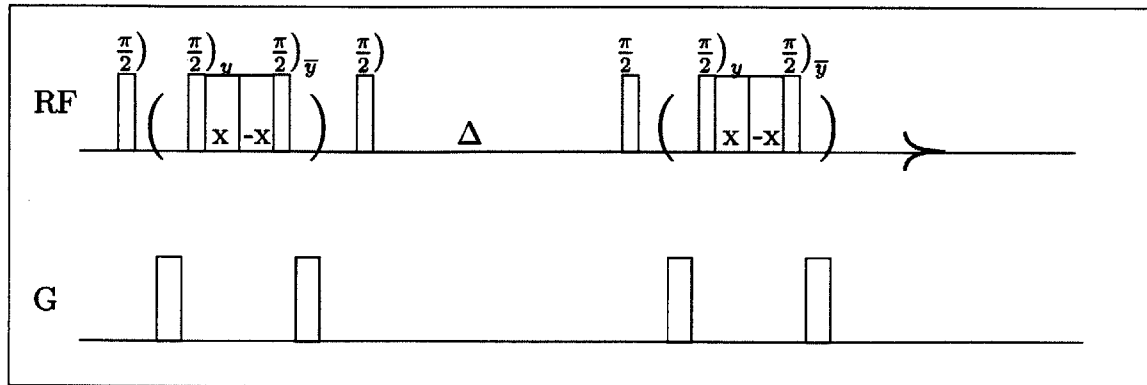
Figure 6-6: The pulse sequence used in the broad line pulsed gradient stimulated echo experiment. A magic echo based dipolar refocusing sequence is incorporated into the encoding and decoding periods of the stimulated echo experiment to extend the naturally short coherence time of the broad line allowing longer composite gradient pulses. The refocusing sequence and gradient pulses in parenthesis were repeated allowing extended encoding and decoding gradient pulses. The diffusion time was incremented between 0.5 s and 12 s.

diffusion coefficient of the broad line can be determined from the sensitivity of the experiment as $D < 10^{-12}$ cm^2/s.

6.5 Analysis

The difference of the narrow line stimulated echo amplitude between experiments with and without gradient pulses indicates the presence of a diffusion process. Moreover, the deviation between experiments with and without gradient pulses increases as the value of k is increased, consistent with Equation 5.9.

By comparison, the gradient on and gradient off experiments for the broad line display no discernible difference in echo attenuation. This data supports the hypothesis of a static broad bath and allows us to place a conservative upper bound on the diffusion coefficient of the broad bath at the sensitivity of the experiment as given by Equation 5.11, $D < 10^{-12}$ cm^2/s.

The acquired narrow line and broad line data was compared by means of a least-squares regression to the model of Section 5.5.2. The extracted value for the intrinsic diffusion coefficient of the narrow bath was $2.39 \pm 0.34 \cdot 10^{-8}$ cm^2/s while no value
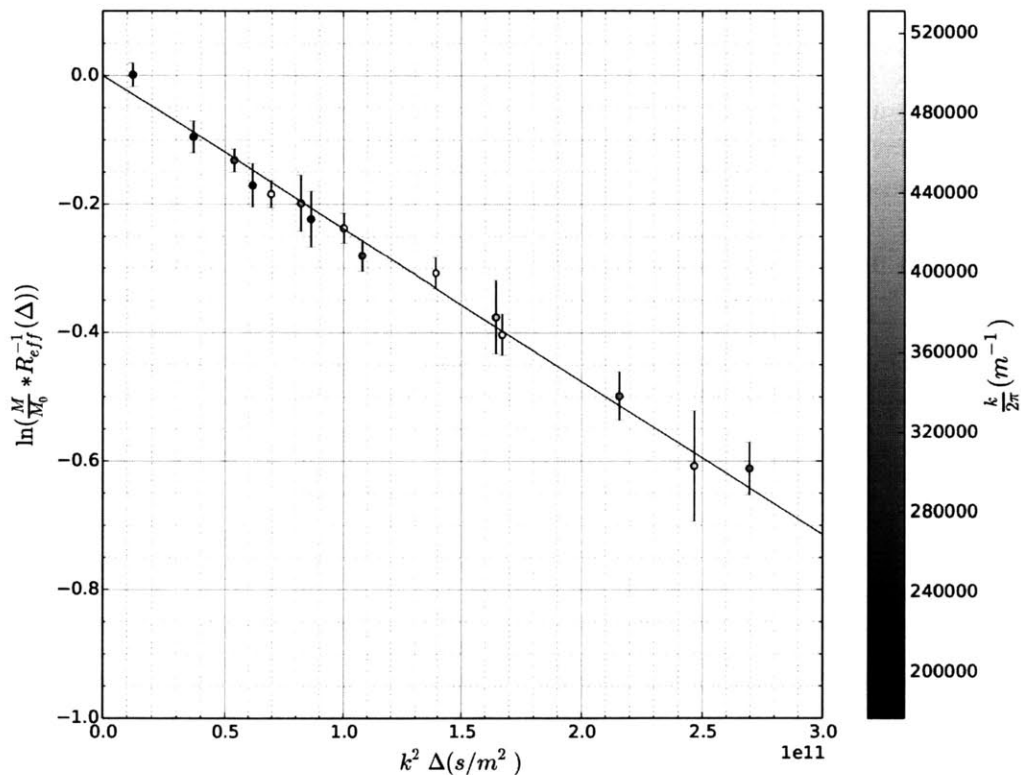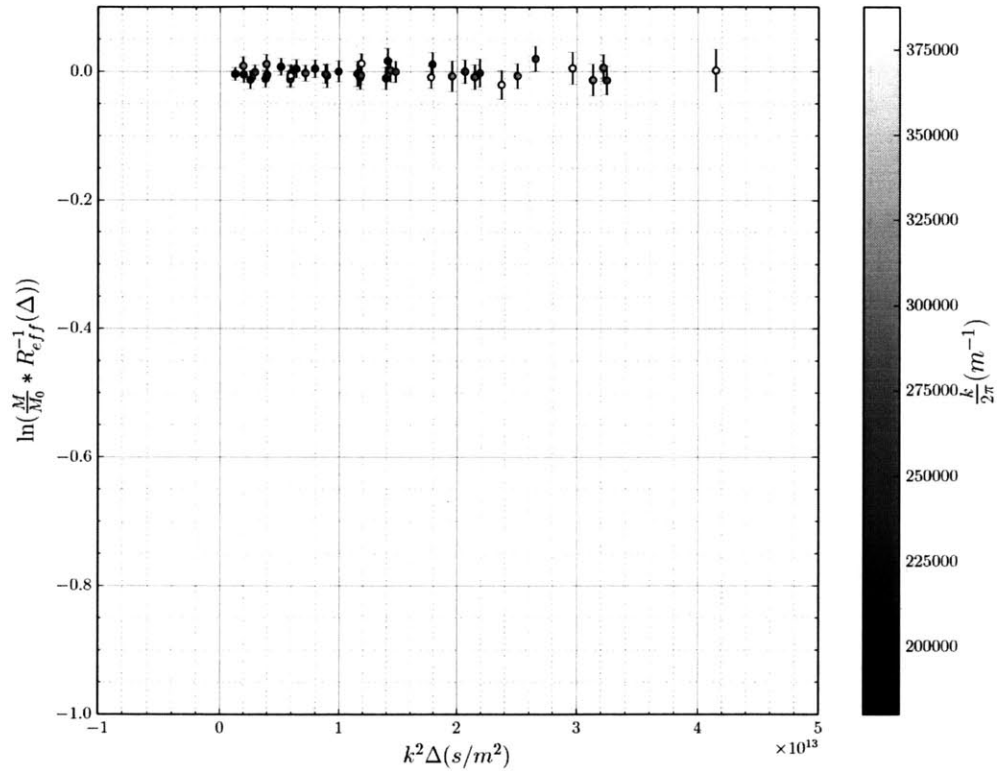
Figure 6-7: A plot of the log broad line stimulated echo attenuation as a function of $k^2\Delta$, as motivated by Equation 5.9. Signal amplitudes have been renormalized to compensate for attenuation due to relaxation and exchange to isolate attenuation due to diffusion. For all values of k and Δ, no diffusive attenuation is observed and an upper bound of the diffusion coefficient of the broad line is placed at 10^{-12} cm^2/s.

was obtained for the intrinsic diffusion coefficient of the broad bath.

Chapter 7

Conclusion and Discussion

This thesis demonstrates the application of a magnetic resonance method for the direct measurement of the self-diffusion coefficient of the lithium-ion conductor lithium sulfide. We measured a diffusion coefficient for one of the two observed lithium baths and determined an upper bound on the diffusion coefficient of the other.

This thesis is the first report of the rate of room-temperature lithium diffusion in lithium sulfide and the first report of a chemically resolved diffusion measurement in a room-temperature lithium battery electrode material. The measured self-diffusion coefficient of the narrow bath is among the fastest of those obtained from theoretical and experimental diffusion measures of other high-current lithium battery cathode materials. This measurement will enable utilization of the mobility of the narrow bath in the design and optimization of future sulfur based cathode materials.

Additionally, we performed a series of NMR relaxometry experiments to characterize an exchange process between these two baths and quantify exchange rates and intrinsic relaxation properties. We provided a review of the properties of a selection of lithium-ion conductors.

To perform these experiments, we employed a dipolar refocusing sequence to extend the naturally short lived coherence of the broad line allowing extended gradient pulses and increased sensitivity to slow diffusion. Additionally, we developed an experimental apparatus for the application of modest current pulsed gradient NMR transport measurements including a new gradient design with an exceptional coil con-

stant. We developed a microscopic model of the two bath exchange process and the influence of exchange on macroscopic observables such as relaxation rates, diffusive path lengths and stimulated echo amplitudes.

This thesis has demonstrated the usefulness of pulsed field gradient nuclear magnetic resonance measurements in studying the transport properties of room-temperature lithium-ion conductors. In particular, the ability to chemically resolve transport measurements has proven useful in distinguishing between the transport properties of the rapidly diffusing narrow line and relatively static broad lines of lithium sulfide.

The methodologies developed in this thesis are applicable to the study of lithium transport in other candidate lithium-ion battery electrode materials. In particular, from the materials review provided in Chapter 2, this method holds promise as a means of investigating the mechanisms underlying diffusion-induced stresses in anode materials such as elemental silicon and $Si - C$ composites, in optimizing the transport limited current capacity in intercalation compounds like $LiFePO_4$ and in resolving transport limited energy storage density in the integration cathode material $Li-$Air.

Bibliography

[1] M. Stanley Whittingham. Lithium batteries and cathode materials. *Chemical Reviews*, 104(10):4271–4302, 2004.

[2] John B. Goodenough and Youngsik Kim. Challenges for rechargeable Li batteries. *Chemistry of Materials*, 22(3):587–603, 2010.

[3] Brian L. Ellis, Kyu Tae Lee, and Linda F. Nazar. Positive electrode materials for Li-ion and Li-batteries. *Chemistry of Materials*, 22(3):691–714, 2010.

[4] Myounggu Park, Xiangchun Zhang, Myoungdo Chung, Gregory B. Less, and Ann Marie Sastry. A review of conduction phenomena in Li-ion batteries. *Journal of Power Sources*, 195(24):7904–7929, December 2010.

[5] J.-M. Tarascon and Michel Armand. Issues and challenges facing rechargeable lithium batteries. *Nature*, 414(6861):359367, 2001.

[6] Kristin Persson, Vijay A. Sethuraman, Laurence J. Hardwick, Yoyo Hinuma, Ying Shirley Meng, Anton van der Ven, Venkat Srinivasan, Robert Kostecki, and Gerbrand Ceder. Lithium diffusion in graphitic carbon. *The Journal of Physical Chemistry Letters*, 1(8):1176–1180, 2010.

[7] Anton Van der Ven, Jishnu Bhattacharya, and Anna A. Belak. Understanding Li diffusion in Li-intercalation compounds. *Accounts of Chemical Research*, 46(5):1216–1225, 2013.

[8] Clare P. Grey and Nicolas Dupré. NMR studies of cathode materials for lithium-ion rechargeable batteries. *Chemical Reviews*, 104(10):4493–4512, 2004.

[9] J. S. Murday. Self-diffusion coefficient of liquid lithium. *The Journal of Chemical Physics*, 48(11):4938, 1968.

[10] T. G. Stoebe and R. A. Huggins. Measurement of ionic diffusion in lithium fluoride by nuclear magnetic resonance techniques. *Journal of Materials Science*, 1(2):117126, 1966.

[11] Detlef Brinkmann. NMR studies of superionic conductors. *Progress in Nuclear Magnetic Resonance Spectroscopy*, 24(6):527552, 1992.

[12] S. Chandrashekar, Nicole M. Trease, Hee Jung Chang, Lin-Shu Du, Clare P. Grey, and Alexej Jerschow. ^7Li MRI of Li batteries reveals location of microstructural lithium. *Nature Materials*, 11(7):311–315, February 2012.

[13] Rangeet Bhattacharyya, Baris Key, Hailong Chen, Adam S. Best, Anthony F. Hollenkamp, and Clare P. Grey. In situ NMR observation of the formation of metallic lithium microstructures in lithium batteries. *Nature Materials*, 9(6):504510, 2010.

[14] Kisuk Kang, Ying Shirley Meng, Julien Brger, Clare P. Grey, and Gerbrand Ceder. Electrodes with high power and high capacity for rechargeable lithium batteries. *Science*, 311(5763):977–980, 2006.

[15] A. Van der Ven, G. Ceder, M. Asta, and P. Tepesch. First-principles theory of ionic diffusion with nondilute carriers. *Physical Review B*, 64(18), October 2001.

[16] Mikhail D. Levi and Doron Aurbach. The mechanism of lithium intercalation in graphite film electrodes in aprotic media. Part 1. High resolution slow scan rate cyclic voltammetric studies and modeling. *Journal of Electroanalytical Chemistry*, 421(12):79 – 88, 1997.

[17] E. Markevich, M.D. Levi, and D. Aurbach. Comparison between potentiostatic and galvanostatic intermittent titration techniques for determination of chemical diffusion coefficients in ion-insertion electrodes. *Journal of Electroanalytical Chemistry*, 580(2):231 – 237, 2005.

[18] Paul Heitjans, Sylvio Indris, and Martin Wilkening. Solid-state diffusion and NMR. *Diffusion Fundamentals*, pages 226–245, 2005.

[19] Charles S. Johnson and Donghui Wu. *Diffusion Measurements by Magnetic Field Gradient Methods*. John Wiley & Sons, Ltd, 2007.

[20] V.V. Sinitsyn, O. Lips, A.F. Privalov, F. Fujara, and I.V. Murin. Transport properties of LaF_3 fast ionic conductor studied by field gradient NMR and impedance spectroscopy. *Journal of Physics and Chemistry of Solids*, 64(7):1201 – 1205, 2003.

[21] A. N. Garroway and R. M. Cotts. NMR measurements of self-diffusion in lithium-ammonia and sodium-ammonia solutions. *Physical Review A*, 7:635–648, Feb 1973.

[22] M. Mali, J. Roos, M. Sonderegger, D. Brinkmann, and P. Heitjans. 6Li and 7Li diffusion coefficients in solid lithium measured by the NMR pulsed field gradient technique. *Journal of Physics F: Metal Physics*, 18(3):403, 1988.

[23] Robert M. Cotts. *Diffusion in Solids*. John Wiley & Sons, Ltd., 1996.

[24] Paul Heitjans and Sylvio Indris. Diffusion and ionic conduction in nanocrystalline ceramics. *Journal of Physics: Condensed Matter*, 15(30):R1257, 2003.

[25] Armin Bunde, Klaus Funke, and Malcolm D. Ingram. Ionic glasses: History and challenges. *Solid State Ionics*, 105(1):113, 1998.

[26] Takeshi Ogasawara, Aurlie Dbart, Michael Holzapfel, Petr Novk, and Peter G. Bruce. Rechargeable Li2O2 electrode for lithium batteries. *Journal of the American Chemical Society*, 128(4):1390–1393, 2006.

[27] Alexander Kraytsberg and Yair Ein-Eli. Review on Li-air batteries-Opportunities, limitations and perspective. *Journal of Power Sources*, 196(3):886 – 893, 2011.

[28] Scott Evers and Linda F. Nazar. New approaches for high energy density Lithium-Sulfur battery cathodes. *Accounts of Chemical Research*, 46(5):1135–1143, May 2013.

[29] John Crank. *The Mathematics of Diffusion*. Oxford University Press, Oxford, second edition, 1975.

[30] A. Einstein. Über die von der molekularkinetischen theorie der wärme geforderte bewegung von in ruhenden flüssigkeiten suspendierten teilchen. *Ann. Phys. Lpz.*, 17:549–560, 1905.

[31] M. von Smoluchowski. Zur kinetischen theorie der brownschen molekularbewegung und der suspensionen. *Annalen der Physik*, 326(14):756–780, 1906.

[32] Robert Zwanzig. Incoherent inelastic neutron scattering and self-diffusion. *Physical Review*, 133(1A):A50, 1964.

[33] Robert Gomer. Diffusion of adsorbates on metal surfaces. *Reports on progress in Physics*, 53(7):9171002, 1990.

[34] S.R. de Groot and Mazur P. *Non-Equilibrium Thermodynamics*. Dover, second edition, 1984.

[35] Young-Il Jang, Bernd J. Neudecker, and Nancy J. Dudney. Lithium diffusion in Li_xCoO2 $(0.45 < x < 0.7)$ intercalation cathodes. *Electrochemical and Solid-State Letters*, 4(6):A74–A77, 2001.

[36] A. D. Le Claire. *Physical Chemistry – An Advanced Treatise*, volume 10. Academic, New York, 1970.

[37] K. Compaan and Y. Haven. Correlation factors for diffusion in solids. *Transactions of the Faraday Society*, 52:786, 1956.

[38] A. D. Le Claire. *Treatise on Solid State Chemistry*, volume 4. Pleenum, New York, 1976.

[39] S Hafner, D E Demco, and R Kimmich. Magic-echo solid-state NMR imaging. *Measurement Science and Technology*, 2(9):882, 1991.

[40] Inyong Chang, Franz Fujara, Burkhard Geil, Gerald Hinze, Hans Sillescu, and Albert Tlle. New perspectives of NMR in ultrahigh static magnetic field gradients. *Journal of Non-Crystalline Solids*, 172:674681, 1994.

[41] O. Zger, S. T. Hoen, C. S. Yannoni, and D. Rugar. Threedimensional imaging with a nuclear magnetic resonance force microscope. *Journal of Applied Physics*, 79(4), 1996.

[42] Arnd Schaff and Wiebren S. Veeman. Mechanically detected nuclear magnetic resonance at room temperature and normal pressure. *Journal of Magnetic Resonance*, 126(2):200 – 206, 1997.

[43] A. Z. Genack and A. G. Redfield. Theory of nuclear spin diffusion in a spatially varying magnetic field. *Physical Review B*, 12:78–87, Jul 1975.

[44] Azriel Z. Genack. Dipole energy dissipation and nuclear spin diffusion in mixed-state superconducting vanadium. *Physical Review B*, 13:68–80, Jan 1976.

[45] D Canet, B Diter, A Belmajdoub, J Brondeau, J.C Boubel, and K Elbayed. Self-diffusion measurements using a radiofrequency field gradient. *Journal of Magnetic Resonance*, 81(1):1 – 12, 1989.

[46] I. Chang, G. Hinze, G. Diezemann, F. Fujara, and H. Sillescu. Self-diffusion coefficients in plastic crystals by multiple-pulse NMR in large static field gradients. *Physical Review Letters*, 76:2523–2526, Apr 1996.

[47] Mark S Conradi, A.N Garroway, D.G Cory, and J.B Miller. Generation of short, intense gradient pulses. *Journal of Magnetic Resonance*, 94(2):370 – 375, 1991.

[48] D.G Cory, J.B Miller, and A.N Garroway. Time-suspension multiple-pulse sequences: applications to solid-state imaging. *Journal of Magnetic Resonance*, 90(1):205 – 213, 1990.

[49] Wurong Zhang and D.G. Cory. Pulsed gradient NMR probes for solid state studies. *Journal of Magnetic Resonance*, 132(1):144 – 149, 1998.

[50] Werner Weppner and Robert A Huggins. Electrochemical methods for determining kinetic properties of solids. *Annual Review of Materials Science*, 8(1):269–311, 1978.

[51] Southampton Electrochemical Group. *Instrumental Methods in Electrochemistry*. Ellis Horwood Series in Physical Chemistry. John Wiley & Sons, Chichester, 1985.

[52] W. Weppner and R. A. Huggins. Determination of the kinetic parameters of mixedconducting electrodes and application to the system Li_3Sb. *Journal of The Electrochemical Society*, 124(10):1569–1578, 1977.

[53] Pier Paolo Prosini, Marida Lisi, Daniela Zane, and Mauro Pasquali. Determination of the chemical diffusion coefficient of lithium in $LiFePO_4$. *Solid State Ionics*, 148(12):45 – 51, 2002.

[54] C. Ho, I. D. Raistrick, and R. A. Huggins. Application of AC techniques to the study of lithium diffusion in tungsten trioxide thin films. *Journal of The Electrochemical Society*, 127(2):343–350, 1980.

[55] G. E. Murch. The Haven ratio in fast ionic conductors. *Solid State Ionics*, 7(3):177198, 1982.

[56] Shin-ichi Nishimura, Genki Kobayashi, Kenji Ohoyama, Ryoji Kanno, Masatomo Yashima, and Atsuo Yamada. Experimental visualization of lithium diffusion in Li_xFePO_4. *Nature Materials*, 7(9):707–711, August 2008.

[57] G. Placzek and L. Van Hove. Crystal dynamics and inelastic scattering of neutrons. *Physical Review*, 93:1207–1214, Mar 1954.

[58] Felix Altorfer, W. Buhrer, I. Anderson, O. Scharpf, Hans Bill, and P. L. Carron. Fast ionic diffusion in Li_2S investigated by quasielastic neutron scattering. *Journal of Physics: Condensed Matter*, 6(46):9937, 1994.

[59] Leslie G. Butler, Burkhard Schillinger, Kyungmin Ham, Tabbetha A. Dobbins, Ping Liu, and John J. Vajo. Neutron imaging of a commercial Li-ion battery during discharge: Application of monochromatic imaging and polychromatic dynamic tomography. *Nuclear Instruments and Methods in Physics Research Section A: Accelerators, Spectrometers, Detectors and Associated Equipment*, 651(1):320–328, September 2011.

[60] Jason B. Siegel, Xinfan Lin, Anna G. Stefanopoulou, Daniel S. Hussey, David L. Jacobson, and David Gorsich. Neutron imaging of lithium concentration in LFP pouch cell battery. *Journal of The Electrochemical Society*, 158(5):A523–A529, 2011.

[61] Shigeomi Takai, Masahiro Kamata, Shigenori Fujine, Kenji Yoneda, Keiji Kanda, and Takao Esaka. Diffusion coefficient measurement of lithium ion in sintered $Li_{1.33}Ti_{1.67}O_4$ by means of neutron radiography. *Solid State Ionics*, 123(1):165172, 1999.

[62] G. Ceder, Y.-M. Chiang, D. R. Sadoway, M. K. Aydinol, Y.-I. Jang, and B. Huang. Identification of cathode materials for lithium batteries guided by first-principles calculations. *Nature*, 392(6677):694–696, April 1998.

[63] Christian Uebing and Robert Gomer. Determination of surface diffusion coefficients by Monte Carlo methods: Comparison of fluctuation and Kubo-Green methods. *The Journal of Chemical Physics*, 100(10):7759, 1994.

[64] J. H. Brewer and K. M. Crowe. Advances in muon spin rotation. *Annual Review of Nuclear and Particle Science*, 28(1):239326, 1978.

[65] G. Gunnarsson and P. Hedegård. Muon diffusion and quantum-motional narrowing. *Europhysics Letters*, 18(4):367, 1992.

[66] Jun Sugiyama. Ion diffusion in solids probed by muon-spin spectroscopy. *Journal of the Physical Society of Japan*, 82(Suppl.A):SA023, 2013.

[67] Jun Sugiyama, Kazuhiko Mukai, Yutaka Ikedo, Hiroshi Nozaki, Martin Mnsson, and Isao Watanabe. Li diffusion in Li_xCoO_2 probed by muon-spin spectroscopy. *Physical Review Letters*, 103(14), September 2009.

[68] R.J. Borg. *An Introduction to Solid State Diffusion*. Academic, San Diego, 1988.

[69] Baris Key, Rangeet Bhattacharyya, Mathieu Morcrette, Vincent Seznec, Jean-Marie Tarascon, and Clare P. Grey. Real-time NMR investigations of structural changes in silicon electrodes for lithium-ion batteries. *Journal of the American Chemical Society*, 131(26):9239–9249, July 2009.

[70] L. J. M. Davis, B. L. Ellis, T. N. Ramesh, L. F. Nazar, A. D. Bain, and G. R. Goward. 6Li 1D EXSY NMR spectroscopy: A new tool for studying lithium dynamics in paramagnetic materials applied to monoclinic Li_2VPO_4F. *The Journal of Physical Chemistry C*, 115(45):22603–22608, 2011.

[71] M. Wilkening and P. Heitjans. New prospects in studying Li diffusion two-time stimulated echo NMR of spin-3/2 nuclei. *Solid State Ionics*, 177(35-36):3031–3036, November 2006.

[72] M. Wilkening, W. Kchler, and P. Heitjans. From ultraslow to fast lithium diffusion in the 2D ion conductor Li0.7TiS2 probed directly by stimulated-echo NMR and nuclear magnetic relaxation. *Physical Review Letters*, 97(6), August 2006.

[73] Paul Heitjans and Jorg Karger. *Diffusion in Condensed Matter*. Springer, Berlin, 2006.

[74] N. Bloembergen, E. M. Purcell, and R. V. Pound. Relaxation effects in nuclear magnetic resonance absorption. *Physical Review*, 73:679–712, Apr 1948.

[75] H Co Torrey. Nuclear spin relaxation by translational diffusion. *Physical Review*, 92(4):962, 1953.

[76] HA Resing and HC Torrey. Nuclear spin relaxation by translational diffusion. iii. spin-spin relaxation. *Physical Review*, 131:1102–1104, 1963.

[77] C. A. Sholl. Nuclear spin relaxation by translational diffusion in solids. *Journal of Physics C: Solid State Physics*, 7(18):3378, 1974.

[78] C. A. Sholl. Nuclear spin relaxation by translational diffusion in solids. II. diffusion in BCC and SC lattices. *Journal of Physics C: Solid State Physics*, 8(11):1737, 1975.

[79] L. S. Cahill, R. P. Chapman, C. W. Kirby, and G. R. Goward. The challenge of paramagnetism in two-dimensional 6,7Li exchange NMR. *Applied Magnetic Resonance*, 32(4):565–581, December 2007.

[80] T Nagaura and K Tozawa. Lithium ion rechargeable battery. *Prog. Batteries Solar Cells*, 9:209, 1990.

[81] Walter van Schalkwijk and Bruno Scrosati. *Advances in lithium-ion batteries.* Springer, 2002.

[82] Norio Takami, Asako Satoh, Michikazu Hara, and Takahisa Ohsaki. Structural and kinetic characterization of lithium intercalation into carbon anodes for secondary lithium batteries. *Journal of The Electrochemical Society*, 142(2):371–379, 1995.

[83] Ping Yu, B. N. Popov, J. A. Ritter, and R. E. White. Determination of the lithium ion diffusion coefficient in graphite. *Journal of The Electrochemical Society*, 146(1):8–14, 1999.

[84] Hui Yang, Hyun Joo Bang, and Jai Prakash. Evaluation of electrochemical interface area and lithium diffusion coefficient for a composite graphite anode. *Journal of The Electrochemical Society*, 151(8):A1247–A1250, 2004.

[85] M.D. Levi, E.A. Levi, and D. Aurbach. The mechanism of lithium intercalation in graphite film electrodes in aprotic media. Part 2. Potentiostatic intermittent titration and in situ XRD studies of the solid-state ionic diffusion. *Journal of Electroanalytical Chemistry*, 421(12):89 – 97, 1997.

[86] Mark W. Verbrugge and Brian J. Koch. Electrochemical analysis of lithiated graphite anodes. *Journal of The Electrochemical Society*, 150(3):A374, 2003.

[87] Kristin Persson, Yoyo Hinuma, Ying Shirley Meng, Anton Van der Ven, and Gerbrand Ceder. Thermodynamic and kinetic properties of the Li-graphite system from first-principles calculations. *Physical Review B*, 82(12), September 2010.

[88] L. Y. Beaulieu, K. W. Eberman, R. L. Turner, L. J. Krause, and J. R. Dahn. Colossal reversible volume changes in lithium alloys. *Electrochemical and Solid-State Letters*, 4(9):A137–A140, 2001.

[89] Cheol-Min Park, Jae-Hun Kim, Hansu Kim, and Hun-Joon Sohn. Li-alloy based anode materials for Li secondary batteries. *Chemical Society Review*, 39:3115–3141, 2010.

[90] Junqian Zhang, Bo Lu, Yicheng Song, and Xiang Ji. Diffusion induced stress in layered Li-ion battery electrode plates. *Journal of Power Sources*, 209:220–227, July 2012.

[91] W. D. Johnston, R. R. Heikes, and D. Sestrich. The preparation, crystallography, and magnetic properties of the $Li_xCo_{1-x}O$ system. *Journal of Physics and Chemistry of Solids*, 7(1):113, 1958.

[92] Jan N. Reimers. Electrochemical and in situ X-Ray diffraction studies of lithium intercalation in Li_xCoO_2. *Journal of The Electrochemical Society*, 139(8):2091, 1992.

[93] A. Van der Ven and G. Ceder. Lithium diffusion in layered Li_xCoO_2. *Electrochemical and Solid-State Letters*, 3(7):301304, 2000.

[94] C. Wolverton and Alex Zunger. First-principles theory of cation and intercalation ordering in Li_xCoO_2. *Journal of Power Sources*, 8182:680 – 684, 1999.

[95] Chanjuan Pan, Young Joo Lee, Brett Ammundsen, and Clare P. Grey. ^6Li MAS NMR studies of the local structure and electrochemical properties of Cr-doped lithium manganese and lithium cobalt oxide cathode materials for lithium-ion batteries. *Chemistry of Materials*, 14(5):2289–2299, May 2002.

[96] H. J. Orman and P. J. Wiseman. Cobalt (III) lithium oxide, $CoLiO_2$: structure refinement by powder neutron diffraction. *Acta Crystallographica Section C: Crystal Structure Communications*, 40(1):1214, 1984.

[97] Rosalind J Gummow and Michael M Thackeray. Electrochemical cell. US Patent 5240794, August 1993.

[98] A. K. Padhi, K. S. Nanjundaswamy, and J. B. Goodenough. Phospho-olivines as positive-electrode materials for rechargeable lithium batteries. *Journal of The Electrochemical Society*, 144(4):1188–1194, 1997.

[99] Byoungwoo Kang and Gerbrand Ceder. Battery materials for ultrafast charging and discharging. *Nature*, 458:190–193, 2009.

[100] D. Morgan, A. Van der Ven, and G. Ceder. Li conductivity in Li_xMPO_4 (M = Mn, Fe, Co, Ni) olivine materials. *Electrochemical and Solid-State Letters*, 7(2):A30, 2004.

[101] D. B. Ravnsbaek, K. Xiang, W. Xing, O. J. Borkiewicz, K. M. Wiaderek, P. Gionet, K. W. Chapman, P. J. Chupas, and Y.-M. Chiang. Extended solid solutions and coherent transformations in nanoscale olivine cathodes. *Nano Letters*, 14(3):1484–1491, 2014.

[102] K. M. Abraham and Z. Jiang. A polymer electrolytebased rechargeable lithium/oxygen battery. *Journal of The Electrochemical Society*, 143(1):1–5, 1996.

[103] G. Girishkumar, B. McCloskey, A. C. Luntz, S. Swanson, and W. Wilcke. Lithium-Air battery: Promise and challenges. *The Journal of Physical Chemistry Letters*, 1(14):2193–2203, July 2010.

[104] Yi-Chun Lu, Hubert A. Gasteiger, Michael C. Parent, Vazrik Chiloyan, and Yang Shao-Horn. The influence of catalysts on discharge and charge voltages of rechargeable lioxygen batteries. *Electrochemical and Solid-State Letters*, 13(6):A69–A72, 2010.

[105] Koichi Nakamura, Muneo Yamamoto, Kazuhiro Okamura, Yoshitaka Michihiro, Ichiro Nakabayashi, and Tatsuo Kanashiro. NMR investigation on the motion of Li^+ defects in $LiCoO_2$ and $LiNiO_2$. *Solid State Ionics*, 121(1):301306, 1999.

[106] K Nakamura, H Ohno, K Okamura, Y Michihiro, T Moriga, I Nakabayashi, and T Kanashiro. ^7Li NMR study on Li^+ ionic diffusion and phase transition in Li_xCoO_2. *Solid State Ionics*, 177(9-10):821–826, March 2006.

[107] Koichi Nakamura, Hideki Ohno, Kazuhiro Okamura, Yoshitaka Michihiro, Ichiro Nakabayashi, and Tatsuo Kanashiro. On the diffusion of Li^+ defects in $LiCoO_2$ and $LiNiO_2$. *Solid State Ionics*, 135(1):143147, 2000.

[108] Kazuhiko Mukai, Jun Sugiyama, Yutaka Ikedo, Hiroshi Nozaki, Koichiro Shimomura, Kusuo Nishiyama, Kingo Ariyoshi, and Tsutomu Ohzuku. Magnetism and lithium diffusion in Li_xCoO_2 by a muon-spin rotation and relaxation (+SR) technique. *Journal of Power Sources*, 174(2):711–715, December 2007.

[109] A. Van der Ven, M. K. Aydinol, G. Ceder, G. Kresse, and J. Hafner. First-principles investigation of phase stability in Li_xCoO_2. *Physical Review B*, 58(6):2975, 1998.

[110] V. W. J. Verhoeven, I. M. de Schepper, G. Nachtegaal, A. P. M. Kentgens, E. M. Kelder, J. Schoonman, and F. M. Mulder. Lithium dynamics in $LiMn_2O_4$ probed directly by two-dimensional ^7Li NMR. *Physical Review Letters*, 86:4314–4317, May 2001.

[111] A.V. Churikov, A.V. Ivanishchev, I.A. Ivanishcheva, V.O. Sycheva, N.R. Khasanova, and E.V. Antipov. Determination of lithium diffusion coefficient in $LiFePO_4$ electrode by galvanostatic and potentiostatic intermittent titration techniques. *Electrochimica Acta*, 55(8):2939 – 2950, 2010.

[112] P. J. Baker, I. Franke, F. L. Pratt, T. Lancaster, D. Prabhakaran, W. Hayes, and S. J. Blundell. Probing magnetic order in $LiMPO_4$ (M= Ni, Co, Fe) and lithium diffusion in Li_xFePO_4. *Physical Review B*, 84(17), November 2011.

[113] Su-Il Pyun and Joon-Sung Bae. The AC impedance study of electrochemical lithium intercalation into porous vanadium oxide electrode. *Electrochimica Acta*, 41(6):919 – 925, 1996.

[114] Yuichi Sato, Tsuneyoshi Asada, Hideaki Tokugawa, and Koichi Kobayakawa. Observation of structure change due to discharge/charge process of V_2O_5 prepared by ozone oxidation method, using in situ X-ray diffraction technique. *Journal of Power Sources*, 68(2):674 – 679, 1997. Proceedings of the Eighth International Meeting on Lithium Batteries.

[115] Xiulei Ji, Kyu Tae Lee, and Linda F. Nazar. A highly ordered nanostructured carbon-sulphur cathode for lithium-sulphur batteries. *Nature Materials*, 8:500–506, 2009.

[116] Danuta Herbet and Juliusz Ulam. Electric dry cells and storage batteries. US Patent 3043896, 07 1962.

[117] Mlarur Lakshmanaroa Bhaskara Rao. Organic electrolyte cells. US Patent 3413154, November 1968.

[118] Dominick A. Nole and Vladimir Moss. Battery employing lithium-sulphur electrodes with non-aqueous electrolyte. US Patent 3532543, 10 1970.

[119] V. S. Kolosnitsyn and E. V. Karaseva. Lithium-sulfur batteries: Problems and solutions. *Russian Journal of Electrochemistry*, 44(5):506–509, June 2008.

[120] Peter G. Bruce. Energy storage beyond the horizon: Rechargeable lithium batteries. *Solid State Ionics*, 179(21-26):752–760, September 2008.

[121] Cline Barchasz, Jean-Claude Leprtre, Fannie Alloin, and Sbastien Patoux. New insights into the limiting parameters of the Li/S rechargeable cell. *Journal of Power Sources*, 199:322–330, February 2012.

[122] Dharmasena Peramunage and Stuart Licht. A solid sulfur cathode for aqueous batteries. *Science*, 261(5124):1029–1032, 1993.

[123] Karthikeyan Kumaresan, Yuriy Mikhaylik, and Ralph E. White. A mathematical model for a Lithium-Sulfur cell. *Journal of The Electrochemical Society*, 155(8):A576, 2008.

[124] H. Yamin and E. Peled. Electrochemistry of a nonaqueous lithium/sulfur cell. *Journal of Power Sources*, 9(3):281 – 287, 1983.

[125] B. M. L. Rao and J. A. Shropshire. Effect of sulfur impurities on Li/TiS_2 cells. *Journal of The Electrochemical Society*, 128(5):942–945, 1981.

[126] R. D. Rauh, F. S. Shuker, J. M. Marston, and S. B. Brummer. Formation of lithium polysulfides in aprotic media. *Journal of Inorganic and Nuclear Chemistry*, 39(10):17611766, 1977.

[127] Min-Sang Song, Sang-Cheol Han, Hyun-Seok Kim, Jin-Ho Kim, Ki-Tae Kim, Yong-Mook Kang, Hyo-Jun Ahn, S. X. Dou, and Jai-Young Lee. Effects of nano-sized adsorbing material on electrochemical properties of sulfur cathodes for Li/S secondary batteries. *Journal of The Electrochemical Society*, 151(6):A791, 2004.

[128] Alexander Gorkovenko, Terje A. Skotheim, and Zhe-Sheng Xu. Cathodes comprising electroactive sulfur materials and secondary batteries using same, 04 2005.

[129] May-Ying Chu. Rechargeable positive electrodes. US Patent 5686201, November 1997.

[130] Byoung Ho Jeon, Jin Hee Yeon, Kwang Man Kim, and In Jae Chung. Preparation and electrochemical properties of lithiumsulfur polymer batteries. *Journal of Power Sources*, 109(1):8997, 2002.

[131] B. Zhang, X. Qin, G. R. Li, and X. P. Gao. Enhancement of long stability of sulfur cathode by encapsulating sulfur into micropores of carbon spheres. *Energy & Environmental Science*, 3(10):1531, 2010.

[132] Wook Ahn, Kwang-Bum Kim, Kyu-Nam Jung, Kyoung-Hee Shin, and Chang-Soo Jin. Synthesis and electrochemical properties of a sulfur-multi walled carbon nanotubes composite as a cathode material for lithium sulfur batteries. *Journal of Power Sources*, 202:394–399, March 2012.

[133] Juchen Guo, Yunhua Xu, and Chunsheng Wang. Sulfur-impregnated disordered carbon nanotubes cathode for Lithium-Sulfur batteries. *Nano Letters*, 11(10):4288–4294, October 2011.

[134] Mumin Rao, Xiangyun Song, and Elton J. Cairns. Nano-carbon/sulfur composite cathode materials with carbon nanofiber as electrical conductor for advanced secondary lithium/sulfur cells. *Journal of Power Sources*, 205:474–478, May 2012.

[135] Hailiang Wang, Yuan Yang, Yongye Liang, Joshua Tucker Robinson, Yanguang Li, Ariel Jackson, Yi Cui, and Hongjie Dai. Graphene-wrapped sulfur particles as a rechargeable Lithium-Sulfur battery cathode material with high capacity and cycling stability. *Nano Letters*, 11(7):2644–2647, July 2011.

[136] Liwen Ji, Mumin Rao, Haimei Zheng, Liang Zhang, Yuanchang Li, Wenhui Duan, Jinghua Guo, Elton J. Cairns, and Yuegang Zhang. Graphene oxide as a sulfur immobilizer in high performance Lithium/Sulfur cells. *Journal of the American Chemical Society*, 133(46):18522–18525, November 2011.

[137] Yun-Xiao Wang, Ling Huang, Li-Chao Sun, Su-Yuan Xie, Gui-Liang Xu, Shu-Ru Chen, Yue-Feng Xu, Jun-Tao Li, Shu-Lei Chou, Shi-Xue Dou, and Shi-Gang Sun. Facile synthesis of a interleaved expanded graphite-embedded sulphur nanocomposite as cathode of LiS batteries with excellent lithium storage performance. *Journal of Materials Chemistry*, 22(11):4744, 2012.

[138] W. Buehrer, Felix Altorfer, J. Mesot, Hans Bill, P. Carron, and H. G. Smith. Lattice dynamics and the diffuse phase transition of lithium sulphide investigated by coherent neutron scattering. *Journal of Physics: Condensed Matter*, 3(9):1055, 1991.

[139] Robert A. Huggins. Recent results on lithium ion conductors. *Electrochimica Acta*, 22(7):773781, 1977.

[140] M. Mousa, Y. S. Oei, and H. Richtering. NMR investigations of cation diffusion in some solids with antifluorite structure. *Le Journal de Physique Colloques*, 41(C6):C6-223–C6-226, July 1980.

[141] Charles P. Slichter. *Principles of Magnetic Resonance*. Springer-Verlag, Berlin Heidelberg, third edition, 1990.

[142] Brian Cowan. *Nuclear Magnetic Resonance and Relaxation*. Cambridge University Press, Cambridge, 1997.

[143] Alex D. Bain. Chemical exchange. In *Modern Magnetic Resonance*, pages 421–427. Springer, 2006.

[144] Alex D. Bain. Chemical exchange in NMR. *Progress in Nuclear Magnetic Resonance Spectroscopy*, 43(34):63 – 103, 2003.

[145] K.J. Laidler. *Chemical Kinetics*. McGraw-Hill, New York, 1965.

[146] Zhi Xu and Jonathan F. Stebbins. Cation dynamics and diffusion in lithium orthosilicate: Two-dimensional lithium-6 NMR. *Science*, 270(5240):1332–1334, 1995.

[147] L. S. Cahill, R. P. Chapman, J. F. Britten, and G. R. Goward. ^7Li NMR and two-dimensional exchange study of lithium dynamics in monoclinic $Li_3V_2(PO_4)_3$. *The Journal of Physical Chemistry B*, 110(14):7171–7177, 2006.

[148] L. J. M. Davis, I. Heinmaa, and G. R. Goward. Study of lithium dynamics in monoclinic $Li_3Fe_2(PO_4)_3$ using ^6Li VT and 2D exchange MAS NMR spectroscopy. *Chemistry of Materials*, 22(3):769–775, February 2010.

[149] M. Wilkening, E. E. Romanova, S. Nakhal, D. Weber, M. Lerch, and P. Heitjans. Time-resolved and site-specific insights into migration pathways of Li^+ in $\alpha - Li_3VF_6$ by ^6Li 2D exchange MAS NMR. *The Journal of Physical Chemistry C*, 114(44):19083–19088, 2010.

[150] Sture Forsen and Ragnar A. Hoffman. Study of moderately rapid chemical exchange reactions by means of nuclear magnetic double resonance. *The Journal of Chemical Physics*, 39(11):2892, 1963.

[151] Sture Forsen and Ragnar A. Hoffman. Exchange rates by nuclear magnetic multiple resonance. III. Exchange reactions in systems with several nonequivalent sites. *The Journal of Chemical Physics*, 40(5):1189, 1964.

[152] D.R Muhandiram and R.E.D McClung. Product operator description of chemical exchange in NMR experiments with application to 1H-3C DEPT magnetization transfer. *Journal of Magnetic Resonance*, 76(1):121 – 135, 1988.

[153] Magnus Helgstrand, Torleif Härd, and Peter Allard. Simulations of NMR pulse sequences during equilibrium and non-equilibrium chemical exchange. *Journal of Biomolecular NMR*, 18(1):49–63, 2000.

[154] H. S. Gutowsky and C. H. Holm. Rate processes and nuclear magnetic resonance spectra. ii. hindered internal rotation of amides. *The Journal of Chemical Physics*, 25(6), 1956.

[155] J. Jeener, B. H. Meier, P. Bachmann, and R. R. Ernst. Investigation of exchange processes by two-dimensional NMR spectroscopy. *The Journal of Chemical Physics*, 71(11), 1979.

[156] Ragnar A. Hoffman. Transient and steady-state overhauser experiments in the investigation of relaxation processes. analogies between chemical exchange and relaxation. *The Journal of Chemical Physics*, 45(6):2049, 1966.

[157] F. Bloch. Nuclear induction. *Physical Review*, 70:460–474, Oct 1946.

[158] Harden M. McConnell and Don D. Thompson. Molecular transfer of nonequilibrium nuclear spin magnetization. *The Journal of Chemical Physics*, 26(4):958–959, 1957.

[159] Harden M. McConnell. Reaction rates by nuclear magnetic resonance. *The Journal of Chemical Physics*, 28(3):430–431, 1958.

[160] J. R. Zimmerman and W. E. Brittin. Nuclear magnetic resonance studies in multiple phase systems: lifetime of a water molecule in an adsorbing phase on silica gel. *The Journal of Physical Chemistry*, 61(10):13281333, 1957.

[161] Harden M. McConnell and Don D. Thompson. Molecular transfer of nonequilibrium nuclear spin magnetization. *The Journal of Chemical Physics*, 31(1):85–88, 1959.

[162] J. R. Alger and J. H. Prestegard. Investigation of peptide bond isomerization by magnetization transfer NMR. *Journal of Magnetic Resonance*, 27(1):137141, 1977.

[163] Craig R. Malloy, A. Dean Sherry, and Ray L. Nunnally. 13C NMR measurement of flux through alanine aminotransferase by inversion-and saturation-transfer methods. *Journal of Magnetic Resonance*, 64(2):243254, 1985.

[164] Alex D. Bain and Janice A. Cramer. Optimal NMR measurements for slow exchange in two-site and three-site systems. *The Journal of Physical Chemistry*, 97(12):2884–2887, 1993.

[165] Alex D. Bain and J.A. Cramer. Slow chemical exchange in an eight-coordinated bicentered ruthenium complex studied by one-dimensional methods. data fitting and error analysis. *Journal of Magnetic Resonance, Series A*, 118(1):21 – 27, 1996.

[166] E. L. Hahn. Spin echoes. *Physical Review*, 80:580–594, Nov 1950.

[167] H. Y. Carr and E. M. Purcell. Effects of diffusion on free precession in nuclear magnetic resonance experiments. *Physical Review*, 94:630–638, May 1954.

[168] R. L. Vold, J. S. Waugh, M. P. Klein, and D. E. Phelps. Measurement of spin relaxation in complex systems. *The Journal of Chemical Physics*, 48(8):3831–3832, 1968.

[169] Thomas L James and George G McDonald. Measurement of the self-diffusion coefficient of each component in a complex system using pulsed-gradient fourier transform NMR. *Journal of Magnetic Resonance*, 11(1):58 – 61, 1973.

[170] Peter Stilbs. Fourier transform pulsed-gradient spin-echo studies of molecular diffusion. *Progress in Nuclear Magnetic Resonance Spectroscopy*, 19(1):1 – 45, 1987.

[171] Kevin F. Morris and Charles S. Johnson. Resolution of discrete and continuous molecular size distributions by means of diffusion-ordered 2D NMR spectroscopy. *Journal of the American Chemical Society*, 115(10):4291–4299, 1993.

[172] J. H. Strange, P. Mansfield, M. Wormald, W. Derbyshire, and E. R. Andrew. Echoes and imaging in solids [and discussion]. *Philosophical Transactions of the Royal Society of London. Series A: Physical and Engineering Sciences*, 333(1632):427439, 1990.

[173] J.B. Miller. NMR imaging of materials. *Progress in Nuclear Magnetic Resonance Spectroscopy*, 33(34):273 – 308, 1998.

[174] W.-K. Rhim, D. D. Elleman, and R. W. Vaughan. Analysis of multiple pulse NMR in solids. *The Journal of Chemical Physics*, 59:3740, 1973.

[175] K. Takegoshi and C.A. McDowell. A "magic echo" pulse sequence for the high-resolution NMR spectra of abundant spins in solids. *Chemical Physics Letters*, 116(23):100 – 104, 1985.

[176] W-K. Rhim, A. Pines, and J. S. Waugh. Time-reversal experiments in dipolar-coupled spin systems. *Physical Review B*, 3:684–696, Feb 1971.

[177] G. Boutis, D. Greenbaum, H. Cho, D. Cory, and C. Ramanathan. Spin diffusion of correlated two-spin states in a dielectric crystal. *Physical Review Letters*, 92(13), March 2004.

[178] Wurong Zhang and D. G. Cory. First direct measurement of the spin diffusion rate in a homogenous solid. *Physical review letters*, 80(6):1324, 1998.

[179] V.V. Sinitsyn, A.I. Privalov, O. Lips, A.I. Baranov, D. Kruk, and F. Fujara. Transport properties of $CsHSO_4$ investigated by impedance spectroscopy and nuclear magnetic resonance. *Ionics*, 14(3):223–226, 2008.

[180] S. Matsui. Solid-state NMR imaging by magic sandwich echoes. *Chemical Physics Letters*, 179(12):187 – 190, 1991.

[181] Aaron Sodickson and David G. Cory. A generalized k-space formalism for treating the spatial aspects of a variety of NMR experiments. *Progress in Nuclear Magnetic Resonance Spectroscopy*, 33(2):77 – 108, 1998.

[182] Paul T. Callaghan. *Principles of Nuclear Magnetic Resonance Microscopy*. Oxford University Press, Oxford, 1991.

[183] Timothy R. Saarinen and Charles S. Johnson Jr. Imaging of transient magnetization gratings in NMR analogies with laser-induced gratings and applications to diffusion and flow. *Journal of Magnetic Resonance*, 78(2):257 – 270, 1988.

[184] J. E. Tanner. Use of the stimulated echo in NMR diffusion studies. *The Journal of Chemical Physics*, 52(5):2523–2526, 1970.

[185] Dimitri P. Bertsekas and John N. Tsitsiklis. *Introduction to Probability*. Athena Scientific, Belmont, Massachusetts, 2002.

[186] H. C. Torrey. Bloch equations with diffusion terms. *Physical Review*, 104:563–565, Nov 1956.

[187] E. O. Stejskal and J. E. Tanner. Spin diffusion measurements: Spin echoes in the presence of a time-dependent field gradient. *The Journal of Chemical Physics*, 42(1):288–292, 1965.

[188] Mirko I. Hrovat and Charles G. Wade. NMR pulsed-gradient diffusion measurements. I. Spin-echo stability and gradient calibration. *Journal of Magnetic Resonance*, 44(1):62 – 75, 1981.

[189] P.T Callaghan. PGSE-MASSEY, a sequence for overcoming phase instability in very-high-gradient spin-echo NMR. *Journal of Magnetic Resonance*, 88(3):493 – 500, 1990.

[190] R.F Karlicek Jr. and I.J Lowe. A modified pulsed gradient technique for measuring diffusion in the presence of large background gradients. *Journal of Magnetic Resonance*, 37(1):75 – 91, 1980.

[191] Phillip Zhe Sun, John Georg Seland, and David Cory. Background gradient suppression in pulsed gradient stimulated echo measurements. *Journal of Magnetic Resonance*, 161(2):168 – 173, 2003.

[192] F. Fujara, B. Geil, H. Sillescu, and G. Fleischer. Translational and rotational diffusion in supercooled orthoterphenyl close to the glass transition. *Zeitschrift fr Physik B Condensed Matter*, 88(2):195204, 1992.

[193] I. J. Lowe. Free induction decays of rotating solids. *Physical Review Letters*, 2:285–287, Apr 1959.

[194] E. R. Andrew, A. Bradbury, and R. G. Eades. Removal of dipolar broadening of nuclear magnetic resonance spectra of solids by specimen rotation. *Nature*, 183:1802, 1959.

[195] M.Matti Maricq and J. S. Waugh. NMR in rotating solids. *The Journal of Chemical Physics*, 70(7):3300, 1979.

[196] W.E. Maas, A. Bielecki, M. Ziliox, F.H. Laukien, and D.G. Cory. Magnetic field gradients in solid state magic angle spinning NMR. *Journal of Magnetic Resonance*, 141(1):29 – 33, 1999.

[197] J.G. Powles and P. Mansfield. Double-pulse nuclear-resonance transients in solids. *Physics Letters*, 2(2):58 – 59, 1962.

[198] I. Solomon. Multiple echoes in solids. *Physical Review*, 110:61–65, Apr 1958.

[199] J.H. Davis, K.R. Jeffrey, M. Bloom, M.I. Valic, and T.P. Higgs. Quadrupolar echo deuteron magnetic resonance spectroscopy in ordered hydrocarbon chains. *Chemical Physics Letters*, 42(2):390 – 394, 1976.

[200] U. Haeberlen and J. S. Waugh. Coherent averaging effects in magnetic resonance. *Physical Review*, 175:453–467, Nov 1968.

[201] J. S. Waugh, L. M. Huber, and U. Haeberlen. Approach to high-resolution NMR in solids. *Physical Review Letters*, 20(5):180182, 1968.

[202] Ulrich Haeberlen. *High Resolution NMR in Solids Selective Averaging*. Academic Press, 1976.

[203] W-K. Rhim. Enhanced resolution for solid state NMR. *The Journal of Chemical Physics*, 58(4):1772, 1973.

[204] P. Mansfield, M. J. Orchard, D. C. Stalker, and K. H. B. Richards. Symmetrized multipulse nuclear-magnetic-resonance experiments in solids: Measurement of the chemical-shift shielding tensor in some compounds. *Physical Review B*, 7(1):90, 1973.

[205] W. S. Warren, S. Sinton, D. P. Weitekamp, and A. Pines. Selective excitation of multiple-quantum coherence in nuclear magnetic resonance. *Physical Review Letters*, 43(24):1791, 1979.

[206] Horst Kessemeier and Won-Kyu Rhim. NMR line narrowing by means of rotary spin echoes. *Physical Review B*, 5:761–768, Feb 1972.

[207] Won-Kyu Rhim and Horst Kessemeier. Transverse-magnetization recovery in the rotating frame. *Physical Review B*, 3:3655–3661, Jun 1971.

[208] S. Matsui. Suppressing the zero-frequency artifact in magic-sandwich-echo proton images of solids. *Journal of Magnetic Resonance*, 98(3):618621, 1992.

[209] G.S. Boutis, P. Cappellaro, H. Cho, C. Ramanathan, and D.G. Cory. Pulse error compensating symmetric magic-echo trains. *Journal of Magnetic Resonance*, 161(2):132 – 137, 2003.

[210] M. Matti Maricq. Application of average Hamiltonian theory to the NMR of solids. *Physical Review B*, 25:6622–6632, Jun 1982.

[211] S. Matsui, Y. Ogasawara, and T. Inouye. Proton images of elastomers by solid-state NMR imaging. *Journal of Magnetic Resonance, Series A*, 105(2):215 – 218, 1993.

[212] S. Matsui, A. Uraoka, and T. Inouye. Improved resolution in solid-state NMR imaging by self-phase encoding. *Journal of Magnetic Resonance, Series A*, 112(1):130 – 133, 1995.

[213] S. Matsui, A. Uraoka, and T. Inouye. Solid-state NMR imaging by tetrahedral-magic-echo time-suspension sequences. *Journal of Magnetic Resonance, Series A*, 120(1):1117, 1996.

[214] S. Matsui and S. Saito. Symmetric echo acquisition for absolute-value display in solid-state NMR imaging. *Journal of Magnetic Resonance*, 149(1):103–109, March 2001.

[215] Walter I. Goldburg and Moses Lee. Nuclear magnetic resonance line narrowing by a rotating RF field. *Physical Review Letters*, 11:255–258, Sep 1963.

[216] Moses Lee and Walter I. Goldburg. Nuclear-magnetic-resonance line narrowing by a rotating RF field. *Physical Review*, 140:A1261–A1271, Nov 1965.

[217] I. Solomon. Rotary spin echoes. *Physical Review Letters*, 2:301–302, Apr 1959.

[218] D. P. Burum and W. K. Rhim. Analysis of multiple pulse NMR in solids. III. *The Journal of Chemical Physics*, 71(2):944–956, 1979.

[219] J. Jeener. Superoperators in magnetic resonance. *Advances in Magnetic Resonance*, 10:1–51, 1982.

[220] Mary L. Boas. *Mathematical Methods in the Physical Sciences*. John Wiley & Sons, Hoboken, New Jersey, second edition, 1983.

[221] Milton Abramowitz and Irene A. Stegun. *Handbook of Mathematical Functions with Formulas, Graphs, and Mathematical Tables*. Dover Scientific, New York, New York, 1972.

[222] Gregory S. Boutis. *Measurement of the spin diffusion rate of dipolar order in single crystal calcium flouride*. PhD dissertation, Massachusetts Institute of Technology, Department of Nuclear Engineering, May 2002.

[223] S. Idziak and U. Haeberlen. Design and construction of a high homogeneity RF coil for solid-state multiple-pulse NMR. *Journal of Magnetic Resonance*, 50(2):281 – 288, 1982.

[224] David M Pozar. *Microwave engineering*. J. Wiley, Hoboken, NJ, 2005.

[225] B. H. Suits and D. E. Wilken. Improving magnetic field gradient coils for NMR imaging. *Journal of Physics E: Scientific Instruments*, 22(8):565, 1989.

[226] J. E. Tanner. Pulsed field gradients for NMR spin-echo diffusion measurements. *Review of Scientific Instruments*, 36:1086, 1965.

[227] R. Pascone. Theoretical and experimental analysis of magnetic field gradients for MRI. In *IEEE Nuclear Science Symposium and Medical Imaging Conference*, pages 1349–1353, October 1993.

[228] Manfred Holz, Stefan R. Heil, and Antonio Sacco. Temperature-dependent self-diffusion coefficients of water and six selected molecular liquids for calibration in accurate 1H NMR PFG measurements. *Physical Chemistry Chemical Physics*, 2(20):4740–4742, 2000.